UNIVERSITY OF SOUTHAMPTON

High Energy and High Intensity Probes of Chemical Dynamics

by

Adam David Smith

Thesis for the degree of Doctor of Philosophy
2017

in the
Faculty of Natural and Environmental Sciences
Chemistry

October 2017

Supervisor: Dr. Russell S. Minns

UNIVERSITY OF SOUTHAMPTON

ABSTRACT

FACULTY OF NATURAL AND ENVIRONMENTAL SCIENCES
CHEMISTRY

Doctor of Philosophy

by Adam David Smith

Gas phase dynamics measurements have been performed using a series of techniques aimed at extending the observation window available to conventional probes. The probes used through the thesis are based on high harmonic spectroscopy, multiphoton ionisation probe photoelectron spectroscopy, and extreme ultraviolet photoelectron spectroscopy.

For the high harmonic spectroscopy experiments we have developed a new experimental set-up in Southampton so that high harmonic spectroscopy experiments can be performed. The development of the system has included the design, building and commissioning of a flat field spectrometer to provide improved signal detection and a more suitable energy range for detection of high harmonics generated from molecules. The development of the experiment is presented in chapter 3. A pump probe study of the Raman excitation of CCl_4 has been performed demonstrating that high harmonic spectroscopy is sensitive to molecular vibrations, this work is presented in chapter 4.

Photoelectron spectroscopy experiments have been performed on both ammonia and carbon disulphide, the results are presented in chapters 5 and 6. The ammonia study employs a multi photon ionisation probe. By probing the dynamics via the intermediate E' Rydberg state we access a different set of vibrational levels in the ion and maintain overlap with the ion state for an extended period of time. Higher lying ion vibrational states have an average excited state lifetime of approximately 200 fs which closely matches the lifetime associated with the non-adiabatic dissociation process while the lower vibrational states have a much longer lifetime of over 300 fs which more closely matches the adiabatic dissociation process. The different trajectories taken by the two competing dissociation pathways at the region of the conical intersection show up different excitation and ionisation propensity allowing us to isolate features related to each process.

By probing carbon disulphide with an extreme ultra violet probe all reaction intermediates have been observed through to the multiple dissociation products. This demonstrates the experimental capabilities whilst using a probe beam generated from high

harmonics, whilst this adds a level of complexity to the experiment it has provided a complete observation of the dissociation dynamics. Whilst carbon disulphide is a simple molecular system we have demonstrated that there are complex motions in the electronic and nuclear dynamics of this system that have not been previously observed.

Contents

List of Figures

Declaration of Authorship

I, Adam David Smith , declare that the thesis entitled *High Energy and High Intensity Probes of Chemical Dynamics* and the work presented in the thesis are both my own, and have been generated by me as the result of my own original research. I confirm that:

- this work was done wholly or mainly while in candidature for a research degree at this University;
- where any part of this thesis has previously been submitted for a degree or any other qualification at this University or any other institution, this has been clearly stated;
- where I have consulted the published work of others, this is always clearly attributed;
- where I have quoted from the work of others, the source is always given. With the exception of such quotations, this thesis is entirely my own work;
- I have acknowledged all main sources of help;
- where the thesis is based on work done by myself jointly with others, I have made clear exactly what was done by others and what I have contributed myself;
- sections of this work have been publised in, Smith et al. Phys. Chem. Chem. Phys. 2016, **18**, 28150-21856, and the work presented in Chapter 6 has been submitted for pulication.

Signed:.....

Date:.....

Acknowledgements

Encouragement and help to complete this thesis has been provided by a number of different people all of whom I would like to thank.

My supervisor Russell Minns who has shown endless enthusiasm throughout my time in Southampton and towards the results that have been obtained. With his continued support, guidance and advice he ensured that the research has progressed and that I have been kept busy! Without whom this thesis would not have been possible. The Leverhulme trust need to be thanked for providing the funding throughout my studies without whom none of this would have been possible. Our theoretical collaborators from the Kirrander group at the University of Edinburgh, for the huge amount of theoretical work they have done particularly Darren Bellshaw for the photoelectron spectroscopy experiments of CS_2.

The staff at Artemis, especially Richard Chapman for his guidance during beam times, all the effort that went in to ensure that experimental components were ordered and as much as possible was in place before we arrived. And above all the friendship developed throughout this time. Including Dan Horke who has participated in many beam times.

I would also like to thank Jeremy Frey and Bill Brocklesby for there guidance and the knowledge they have imparted upon me. A special thanks to Bill who has taught me many aspects of ultra-fast laser science. Most importantly thank you for to you both for the use of the laser system. The fellow group members, Ed Jager, Matthew Parsons, Pete Baksh, Emily Warne, Frank Longford and Lee Steinberg, who all provided many conversations and ensured that I remained sane throughout my time in Southampton. Several coffees with Ed Jager discussing my latest problems, and regularly that something was wrong with the laser.

My Family who have been continually supportive throughout but have shown large amounts of encouragement during the final months as my studies came to a close.

Finally I would like to thank Ellie Hodges who has offered a huge amount of support throughout my time in Southampton. She has kept me entertained during the long hours of writing and has always been happy to have a chat about any problem that has arisen. There cannot be another teacher with as fuller understanding of high harmonic generation and chemical dynamics. Thank you for all you help!

Chapter 1

Introduction

Photochemical processes are notoriously complex. They involve the coupled motion of electrons and nuclei on incredibly fast time scales. Typically, the ultra-fast motion of the molecular framework leads to a dynamic flow of energy between the electronic and geometric structures. Competing processes occur before the eventual formation of multiple reaction products, via many intermediate states.

Photochemical reactions can be described as the absorption of a photon which leads to a change in the molecular motion resulting in a molecular structure. These reactions are the foundations for the work presented in this thesis. The aim of this chapter is to describe photochemistry and chemical dynamics in detail and review different methods for measuring chemical dynamics. In particular it will discuss the limitations in measuring chemical dynamics and how these limitations can be over come by using high harmonic generation. High harmonic generation enables the production of high energy ultra-short pulses enabling the measurement of the ultra-fast dynamics that occur during a chemical reaction. The high energy, short wavelength pulse allow us to measure the entire reaction co-ordinate.

1.1 Chemical Dynamics

Photochemical reactivity lies at the centre of a large number of biological and technological important phenomena. These phenomena range from the photosensitivity of DNA to the capture of solar energy.[4,5] Photochemical reactions have a clear importance, yet our understanding of the underlying mechanism is incomplete. Chemical reactions and the structure of molecules is controlled by their valence electrons. When a photochemical event takes place, the absorption of a photon leads to change in the valence electronic structure. This change in the valence electronic structure drives reactivity, fragmentation and rearrangements. To understand these, photochemical reactions need to be studied.

Throughout this thesis the focus will be on the dynamics of individual molecules. The study of molecular dynamics is important, as understanding the motion of constituent atoms and changes to electronic structure of reacting molecules leads to a comprehension of the chemical reaction that is undergone by the molecule that is being studied. Molecules and atoms in the gas phase are easier to study as they can be considered isolated from each other and their environment due to the large spacing between molecules and therefore they have exceptionally weak inter-molecular interactions.

An approach that is used in order try and gain an understanding of large and complex molecular systems is the bottom up approach.[6] This approach considers the smallest molecular fragment of a much larger system in order to reduce the complexity of the measurement. Insight can be provided as to how the larger system would behave without the complexity of unravelling information from the significantly more complex system. An example of where the bottom up approach has been applied in work presented in Horke et. al. Phys. Rev. Lett. 2016, **117**, 163002. To understand the effects of hydrogen bonding in much larger biomolecules (such as DNA) the N-H-N unit can be taken on a mimic for this has been found within this molecular system. Two ammonia molecules contain this N-H-N unit therefore, the study of an ammonia dimer system could draw some conclusions as to how larger molecules interact at this point. In this

instance the work was carried out in the gas phase and small molecular clusters were formed leading to the desired molecular interaction.

The aforementioned photochemical process can be described in it's simplest form as R + hν $\rightarrow$ *R $\rightarrow$ P, the molecule (R) that absorbs a photon (hν), whose frequency (ν) can be adsorbed by R.[7] *R is the electronically excited molecule, and P is the products formed from this process. This photochemical process describes a photochemical change. For example, when a molecule undergoes photodissociation leading to the formation of the product or products.[8] Another example of this process is the ring opening of cyclohexadiene.[9] Other photophysical processes can occur, where a photon is absorbed but no overall photochemical change occurs, the products are the reformation of the ground state i.e R + hν $\rightarrow$ *R $\rightarrow$. A good example of this process is when a molecule undergoes phosphorescence or fluorescence and upon the emission of light returns to its ground state unchanged. The overview provided here is greatly simplified when compared to what is occurring within a molecular system, where numerous different states are involved each contributing to each step effecting how the reaction progresses. Taking the final step in this chain, R* $\rightarrow$ P there are several different states that could be involved with a number of different processes occurring, in the 1930's Jablonkski depicted the electronic transitions in a diagrammatic form making the process much clearer and simpler to explain.[10]

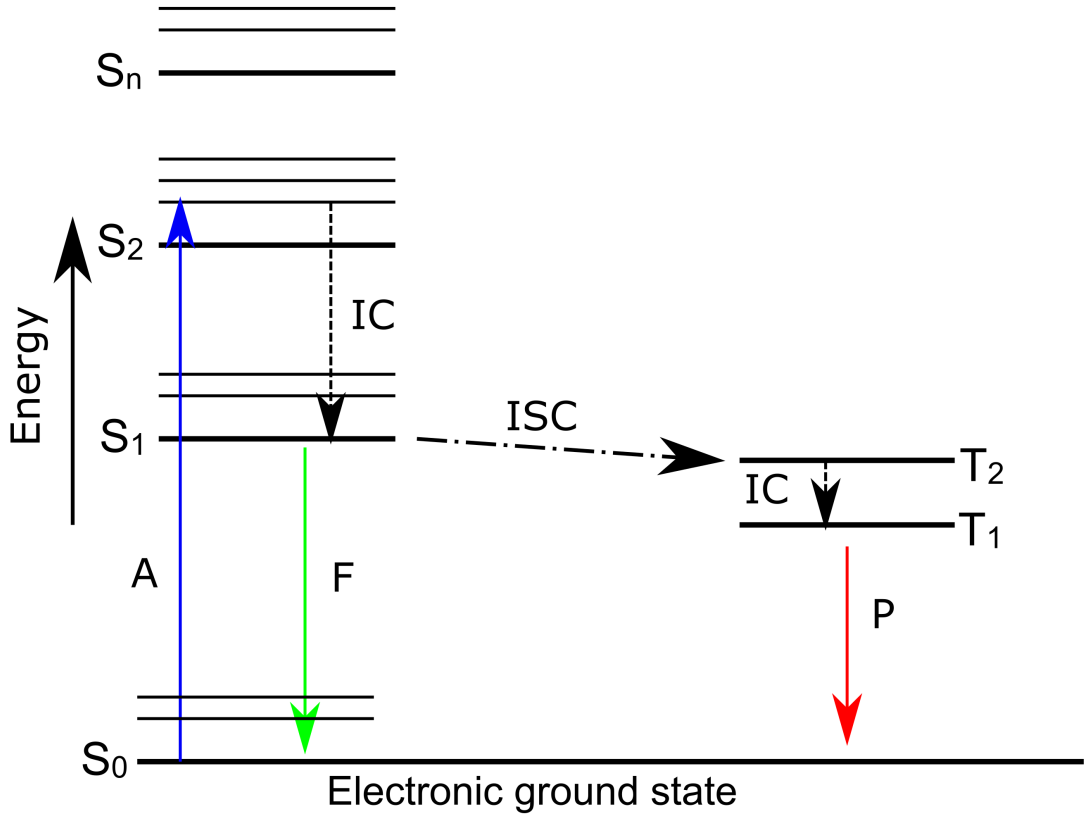

FIGURE 1.1: A Jablonkski diagram, showing electronic transitions from the ground state into the second electronic state following the absorption of a photon (A), the molecule undergoes internal conversion (IC) into the first excited state, leading to the emission of light via florescence (F). There is a second process happening during which absorbed energy undergoes inter-system crossing (ISC) into the second triplet state (T_2), internal conversion occurs once again here to the first triplet state (T_1) resulting in the emission of light via phosphorescence (P)

In the figure 1.1 a Jablonkski diagram can be seen. There are several vibrational levels with the ground electronic state labelled S_0 and for the excited states, S_1, S_2 though to S_n. For the process shown in figure 1.1 upon the absorption of a photon the molecule transitions to the second excited state, non-radiative transitions subsequently occur until the molecule is in the ground vibrational level of the singlet excited state (S_1). The excess electronic energy is dissipated through collisions and exchange of energy with other molecules leading to vibrational relaxation. It will then decay back to the ground state leading to the emission of light via fluorescence. An alternative process can

occur from the singlet excited state through inter-system crossing into the triplet state, T_2. This leads to the emission of a photon via phosphorescence after internal conversion to T_1. As can be seen the digram defines the electronic changes within the molecule but provides no information as to geometric changes. In almost all cases, every process that occurs in the Jablonkski digram involves the molecule changing structure. However, Jablonkski diagrams allow changes in electronic structure to be shown, and a fraction of the possible outcomes when a photon of light is applied to a molecule. In order to portray these process properly a potential energy surface is required. An example of potential energy surface can be seen in figure 1.2 for the photodissociation of CS_2.

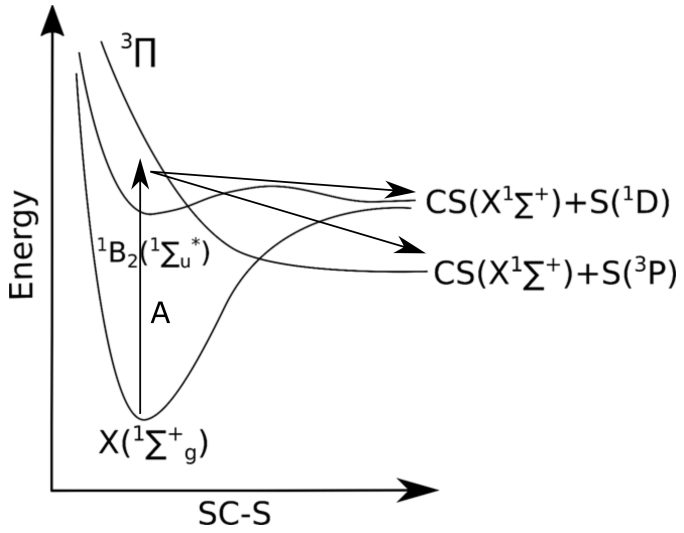

FIGURE 1.2: A schematic potential energy surface of the dissociation dynamics of CS_2, A is the absorption of a photon into the singlet excited state. Following initial excitation this leads to the dissociation, resulting in the formation of S(^{1}D) singlet and S(^{3}S) triplet following intersystem crossing, the cartoon representation is adapted from Hu, et al.[1]

The potential energy surfaces can be used to describe the energy of the system as a function of molecular and electronic structure. These provide information about the location of energy minima, transition states and describe the forces acting upon a molecule that drive it from starting reactants to final products.[11] A particular important feature on a potential energy surface for many polyatomic molecules is the conical intersection. Conical intersections are the point where different states of electronic structure cross and allow highly efficient relaxation dynamics. Conical intersections are important as at this

point a molecule crosses from one state to another resulting in an electronic structure change and generally a geometric change. As can be seen figure 1.2 once the molecule is excited into a new electronic state it will then begin to relax to a lower energy configuration, this could involve dissociation, isomerisation or the molecule returning to its ground state. In the excited state, the molecule will have a different electronic structure, which will have a new equilibrium structure associated to it. The molecule will then relax into this new equilibrium structure which leads to a geometric change. Which can drive electronic changes such as internal conversion or inter-system crossing.

In figure 1.2 we can see the molecule is first excited into an electronic state. This molecule then begins to relax going via a equilibrium geometry for the excited state which is at extended C-S bond distances. Once the molecule begins to decay there are several different path that it may follow. It is difficult to make observations of the full potential energy surface, as the dynamics that are occurring are ultra-fast. Ultra-fast dynamics range from picoseconds to attoseconds, these are the time-scales over which molecules rotate, vibrate and dissociate into various fragments.[12] The study of such process has been made possible since the introduction of the laser. Short light pulses enable molecular motion to be studied and an understanding of the motions to be obtained, these short light pulses can be used in several different ways in order to probe the molecules dynamics. The different ways in which these short light pulses can be used will be discussed in the following section, section 1.2. Throughout this work we will look at the development of new probes in order to study chemical dynamics, with the aim of allowing us to map a full and complete reaction co-ordinate. Building up a picture of a molecules pathway as it undergoes a photochemical reaction. The aim is to monitor the full reaction coordinate of a molecule from the initially excited state through to the formation of its multiple dissociated products.

1.2 Measurement of Chemical Dynamics

Since the 1950s many spectroscopic techniques have been available to chemists, enabling them to make static measurements of a molecules structure.[13,14] Infra-red absorption

can be used to monitor molecular vibrations, in order to be monitored the vibration mode that is being observed must cause a change in dipole moment. This technique is widely used for identifying different molecular functional groups.[15] Molecular vibrations can also be probed using Raman spectroscopy. Raman spectroscopy relies upon the scattering of light by molecules. Both Stokes and anti-Stokes scattering can be observed using Raman spectroscopy, Stokes scattering results in the molecule being excited from the ground state and returns to the first vibrational level, the energy of photon is equal to the difference between the instant light and the energy that is absorbed by the molecule. Anti-Stokes scattering occurs when the molecule is excited from the first vibrational state and gains energy from the indecent photon, when it decays back to the ground state it leads to the emission of a higher energy photon than that of the incident radiation. For a molecule to be Raman active there must be a change in polarizability of the molecule as a result of the motion. Raman spectroscopy results in a very clear spectrum and this technique can be used in several different ways, from the conventional measurement of a molecule through to biological imaging.[16–18] Another way of looking at the fine structure of a molecule is rotational spectroscopy. By analysing the molecular rotations a highly precise structure for a molecule can be obtained.[19,20]

Fluorescence or phosphorescence spectroscopy is a type of electronic spectroscopy based upon promoting an electron from the ground state into an excited electronic state.[21] The light that is emitted when the electron relaxes back to the ground state is then recorded. Fluorescence is the emission of photon when the electron relaxes straight back down to the ground state. Phosphorescence is when the electron undergoes intersystem crossing to a triplet state before relaxing back down to the ground state. The energy of the emitted electrons directly correlates to the energy gap between the two states. Typically, fluorescence has a shorter emission lifetime when compared to phosphorescence. This method has been represented diagrammatically in figure 1.1. All of techniques mentioned in this paragraph have been used to probe a molecular geometry for many years. These static probes can all be employed in order to make measurements of molecular dynamics.

Early time resolved measurements of chemical dynamics were made by George Porter and Manfred Eigen who both shared the Nobel prize for there work in 1967.[22,23] Porters

measurements used the stop flow method to monitor diffusion and the interaction of molecules on a microsecond timescale. Porter used flash photolysis in combination with the stopped flow method to observe transient intermediates within a chemical reaction. Eigen was performing measurements using electronics in order to measure, immeasurably fast reactions. During his work measured the the coming together of H^+ and OH^- ions during a neutralisation reaction in order to form water. The available light source and electronics limited them both respectively in terms of the time scale of the measurements that they could perform. In order to capture a molecules dynamics in more detail, measurements need to be performed on an ultra-fast time scale only then can a clear understanding of a molecules motion be obtained. Ultra-fast time-scales are extremely short and cover a range from picoseconds(1×10^{-12} s) to attoseconds(1×10^{-18} s). This time scale is time scale upon which a molecule rotates, vibrates and undergoes electronic structure changes which lead to dissociation. The measurements of Porter and Eigen were based on a microsecond time scale, this time scale provides information of reactants, some intermediate steps and the products that are formed, but in a chemical reaction there are many more steps and states all of which need to be understood because all of the states influence how a reaction progresses. Photo-dissociation reactions are often complex, with several different intermediate states involved, from the ground state molecule to the photo dissociated product. Photo-dissociation reactions can occur in different ways, direct dissociation, dissociation via a triplet state requiring inter-system crossing such that the intermediate steps and the geometric changes for each particular molecule will be different.

Measurements of chemical dynamics were revolutionised by our ability to produce short laser pulses whose duration was on the time scale of the fundamental motions of molecules. This enables us to pump molecules into an excited state and then probe them on the time scale over which the molecular motion is occurring. Both pulses will have a percentage of the overall energy that is available from the laser system. In order to perform these ultra-fast measurements a laser capable of producing pulses is required. Laser systems have been capable of producing femtosecond pulses since the early 1990s, which saw the dawn of femtosecond time resolved experiments.[24]

Following on from the work of Porter one example of an early pump probe experiment is the femtosecond transition state spectroscopy carried out by Zewail.[25] In one example they study iodine cyanide (ICN) and the dissociation of this molecule. Their experiment has a pump and a probe, which are delayed relative to one another using an interferometer. The two beams are then recombined to overlap in an ICN flow gas system. The experiment was done using laser induced fluorescence as a probe, by tuning the probe frequency to monitor the different reaction intermediates, as the wavelengths required were accessible the whole dissociation was captured. In this experiment they observe the dissociation of this molecule and the reaction intermediates drawing the conclusion that this technique can be used to observe the states in unimolecular and some special biomolecular reactions.[26] Due to the simple nature of ICN this can be considered to be a windowless measurement of chemical dynamics as the whole reaction co-ordinate was captured. However, this was only possible due to direct dissociation that is undergone by ICN. This type of windowless measurement is something we want to try and develop in order to gain an understanding of more molecular systems, so that the depth of understanding we have for complex molecular systems can be developed due to them being observed in a windowless manner. In order to achieve this, the techniques that we will be using are both ionisation based. Photoelectron spectroscopy and high harmonic spectroscopy will now be introduced in turn.

1.2.1 Photoelectron Spectroscopy

Photoelectron spectroscopy is the energy measurement of electrons that are emitted from solids and liquids or gases after the absorption of a photon.[27–29] The focus of this work is on photoelectron spectroscopy of gases. The emission of the photoelectron occurs by the photoelectric effect, in order to determine the binding energy of the electron to the substance. The molecule interacts with the beam of light sufficient enough to induce photoelectric ionisation, the photoelectrons that are emitted are characteristic of their original electronic state, they also depend upon the vibrational and rotational state. When we record a photoelectron spectrum we measure the electrons kinetic energy, this

can easily be converted to the binding energy of the electron which removes the additional energy that is provided from the light used cause the emission of the photoelectron.

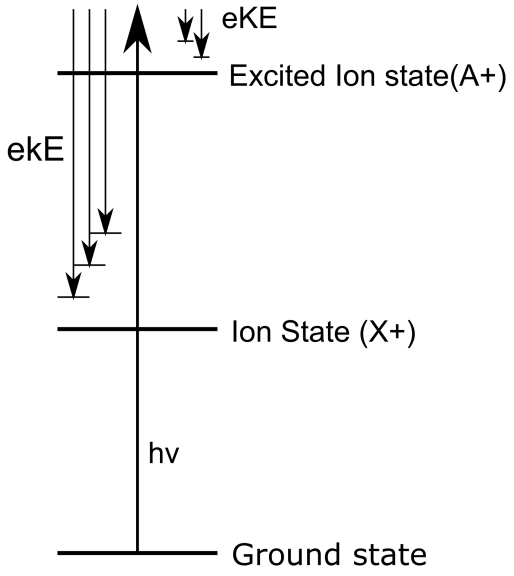

FIGURE 1.3: Schematic to show that a molecule can be examined using an ionisation probe in order to produce a photoelectron with the photoelectron spectrum produced with the overlap from the ground state to all accessible ion states. This leads to transitions into different ion states and vibrational states within a particular ion state and leads to a distinctive spectrum, for the species that is being probed in this manner.

In figure 1.3 we take a photon of very high energy in order to induce transitions into the various electronic states. From the neutral ground state (X) the molecule is ionised into the ground state of the ion (X^+), and the excited state of the ion (A^+) and the various vibrational states that are associated with those ions. These electrons will be emitted with a characteristic spectrum whose shape derives from the overlap between the neutral ground state and all accessible ion states. The energy that is given off by that electron is the electrons kinetic energy (eKE), the electrons kinetic energy can be linked to its binding energy (E_B) using the following relationship, $eKE = h\nu - E_B$, where $h\nu$ is the energy of the ionising photon. Photoelectron spectroscopy can be used to make both static measurements of the different states that are found within molecules as well as being used as a method of probing molecular dynamics when the molecule has had some dynamics initiated via a pump pulse. A photoelectron spectrum of carbon tetrabromide (CBr_4) can be seen in the figure 1.4.

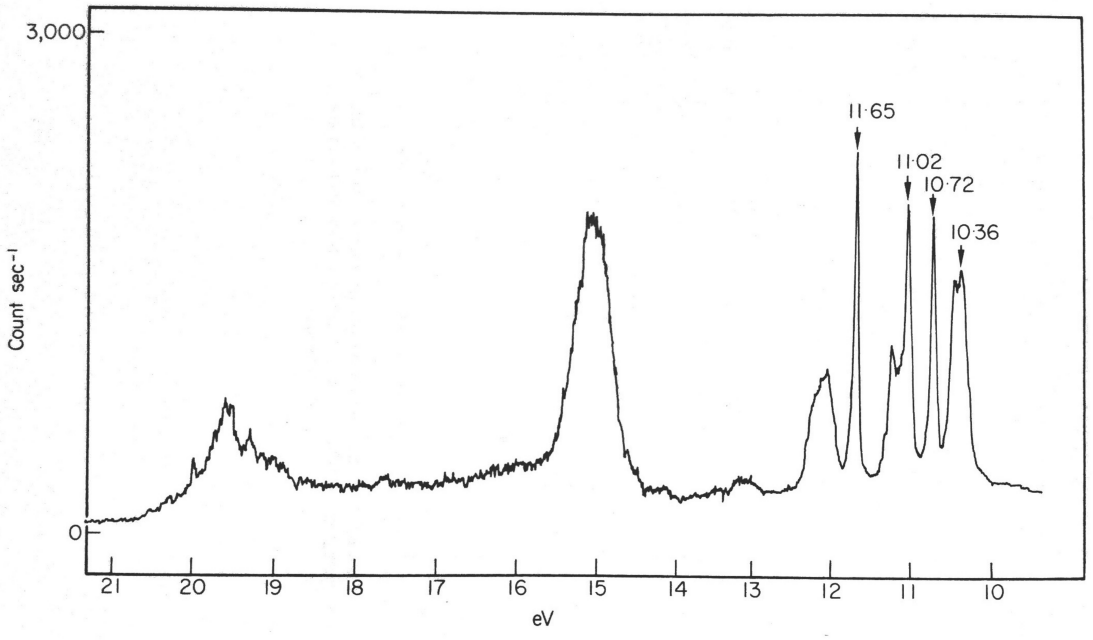

FIGURE 1.4: A photoelectron spectrum of CBr_4 shown as an example of a photoelectron spectrum. The spectrum has been scanned in from Molecular Photoelectron Spectroscopy by Turner p 239. [2]

The figure 1.4 shows the different states within CBr_4, the first ionisation band is centred around 11 eV, within this region there are several bands; 10.36 eV, 10.72 eV, 11.02 eV and 11.65 eV which all correspond to the different vibrational levels within the first ion state of the molecule and are all well defined within this image. As energy increased it can be seen there is a progression in the ion states, with the second ion state being at 15 eV, and the third ionisation band being around 19.5 eV. In order to obtain this spectrum a high energy probe was used, the probe was produced using a helium lamp, providing a maximum energy of 24.47 eV. This shows that up to the third ionisation level of CBr_4 is accessible using a helium lamp, and it also provides resolution of the vibrational bands, certainly within the first ionisation state in this instance. All states can be ionised and photoelectron spectroscopy is sensitive to electronic and geometric structure. So in principle photoelectron spectroscopy can provide a universal probe which is sensitive to both electronic and geometric changes within a molecular system.

In order to make time resolved measurements, short pulses are required such that the dynamics that are occurring can be observed. Photoelectron spectroscopic measurements can be made on a synchrotron which provides very high energy making the observation window large however, the time resolution is limited to the bunch length that is produced and therefore temporal resolution is limited to hundred of picoseconds at best. In order to get around this issue lower energy ionisation sources are used, predominantly from laser systems which are conventionally limited to 6 eV. The shorter pulse lengths enable the study of ultra-fast dynamics to be performed. By increasing the temporal resolution of the experiment the energy of the probe is limited, and this means that making a measurement of a complete reaction co-ordinate is difficult as often not all of the reaction intermediates can be ionised by the probe, and therefore photoelectrons spectroscopy is blind to these. An example of this is a measurement that was performed by Gessner, et. al. of the photo-dissociation $(NO)_2$.[8] In this study they successfully recorded the dissociation dynamics of $(NO)_2$, a schematic representation of the dynamics is shown in figure 1.5.

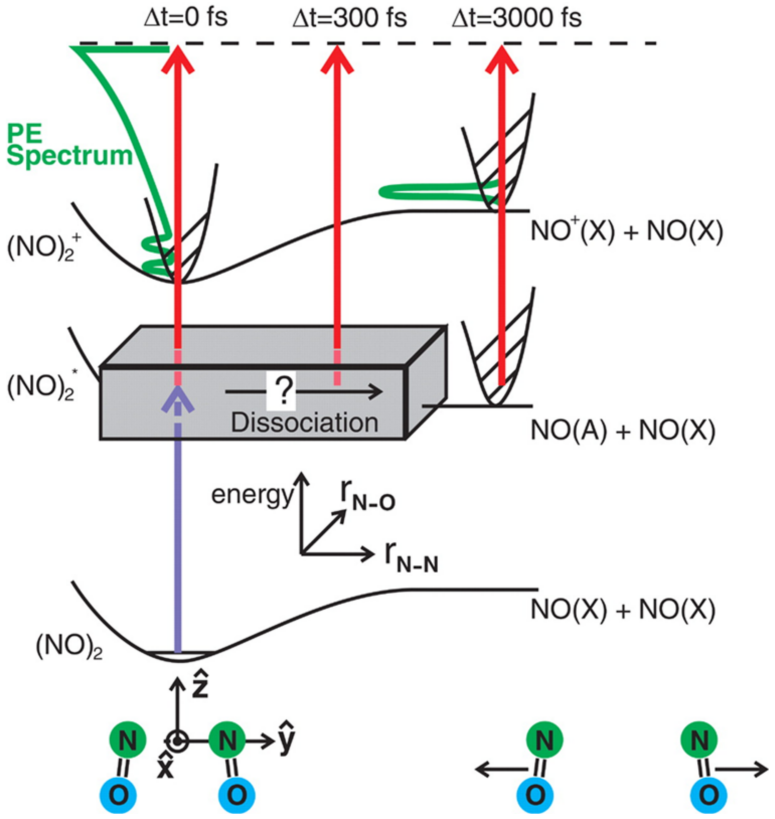

FIGURE 1.5: A potential energy surface taken from work by Gessner et. al. Upon initial excitation the reaction co-ordinate can be monitored for $(NO)_2$. The black box in this figure represents the region of a chemical reaction that cannot typically be observed experimentally.

The black box in figure 1.5 represents a region of the dissociation process that cannot be experimentally measured. In most photochemical measurements, initial conditions and starting points are known but as the reactions progresses there is a region that cannot be measured until the final products are formed.

The probe energy has limited the observation window of the various different products that are produced when a molecule is undergoing photo-dissociation, whilst maintaining good temporal resolution. In order to extend the energy range whilst maintain the ultrafast regime, high harmonic generation can be used to produce high energy photons. The production of these high energy short pulse length photons has lead to the mapping of the full dissociation dynamics for a simple molecule, Br_2. By pumping the molecule with a 400 nm probe Nugent-Glandorf et al. obtained a series of spectra showing the

dissociation.[30] The spectrum after pumping showed signals from atomic Br. After time delays of + 500 fs from time zero, although again this is a direct dissociation process the same as the ICN example previously mentioned. Makida et. al have made preliminary observations of the relaxation dynamics of 1,3-Butadiene using a 42 nm (29.5 eV) high harmonic pulse, due to the large nature of the molecule the understanding of the results is highly reliant upon theoretical calculations that are presented within the paper.[31] The time resolved spectrum shows surprisingly large depletion at time zero, significant changes at negative times and noise levels that limit the interpretation. However, this work shows that time resolved measurements of more complex molecules can potentially be performed using a high harmonic generation probe. In order to perform this type of measurement high harmonic generation needs to be used, the details of high harmonic generation will be discussed in section 1.2.2.

1.2.2 High Harmonic Generation

High harmonic generation is a non-linear process during which an intense infra red laser field is converted to Extreme Ultra Violet (XUV) radiation. Typically this process occurs in the gas phase but has also been performed on liquids and solids. In order to perform high harmonic generation a high intensity laser pulse is required. Corkum proposed that semi-classically, high harmonic generation is based on three key steps; ionisation, propagation and recombination, this leads to the production of XUV.[32] Specifically, intensities of 10^{14} Wcm^{-2} are required, so the electric field produced perturbs the Coulomb potential, these intensities are generated using a femtosecond laser systems. The electric field that is produced distorts the Coulomb potential enough that a bound electron can undergo tunnel ionisation. The electron can then be recombined with its parent ion, leading to a coherent emission of short wave radiation extending into the XUV. Before going into details of the three step model, strong laser fields and tunnel ionisation needs to be discussed.

1.2.3 Strong Laser fields and molecular interactions

The initial step in high harmonic generation is ionisation in the presence of a strong laser field. Both multiphoton and tunnel ionisation processes can occur under these conditions. An indication as to which of these processes is occurring can be obtained through the Keldysh parameter (K).[33] This provides an insight into how different species interact with laser fields. This parameter is a quantitative measure of the number of electrons that can undergo tunnelling events relative to the number of electrons that undergo multiphoton ionisation and can be calculated from,

$$K = \sqrt{\frac{I_p}{2U_p}} \tag{1.1}$$

K here is the Keldysh parameter, I_p is the ionisation potential, the term U_p is the pondermotive potential, this describes the average wiggle energy of an electron in an electric field.

$$U_p = \frac{e^2 E_0^2}{4 m_e \omega_0^2} \tag{1.2}$$

e is the charge of an electron, E_0 is the linearly polarised electric field amplitude, m_e is the mass of an electron and ω_0 is the laser carrier frequency.

If $K >> 1$ then a multi-photon regime is present, during this the number of tunnelling events per optical cycle is much less than 1. High harmonic generation is dependent upon tunnelling, so the probability of high harmonic generation in a multi-photon regime is very low. High harmonic generation occurs when $K << 1$ this is generally described as the tunnelling regime.

The tunnel ionisation rate can be calculated using a formula derived by M. Ammosov, N. Delone and V. Krainov for a general atom, the resulting formula is known as the ADK tunnelling formula.[34,35] The ADK tunnelling formula is used to allow us to predict the conditions needed to generate harmonics, this is helpful as it means experimental conditions can be known before and expected results can be predicted. ADK has been

used throughout this thesis in order to predict high harmonic generation. This is a very powerful tool as it has enabled successful predictions of the experimental conditions required to perform high haromnic generation. Once the tunnelling rate (W) has been calculated this can be used with the magnitude of the electric field to calculate the probability of ionisation occurring during a time interval and can be shown by equation 1.3.

$$P(t) = W[(\varepsilon(t))]dt \tag{1.3}$$

Where:

$$W = \omega_p \mid C_{n*l*} \mid^2 G_{lm} \left(\frac{4\omega_p}{\omega_T}\right)^{2n*-m-l} exp[-4\omega_p/(3\omega_T)] \tag{1.4}$$

and:

$$\begin{aligned} \omega_p = \frac{I_p}{\hbar}, \quad \omega_T = e\varepsilon_0/(2mI_p)^{1/2}, \quad n^* = (I_p^H/IP)^{1/2}, \\ \mid C_{n*l*} \mid^2 = 2^{2^{n^*}}[n * \Gamma(n^* + l^* + 1)\Gamma(n^* - l^*)]^{-1}, \\ G_{lm} = (2l+1)(l+ \mid m \mid)!\,(2^{-|m|})/[(\mid m \mid)!\,(l- \mid m \mid)!\,)], \end{aligned} \tag{1.5}$$

In these equations 1.4 and 1.5, I_p is the ionisation potential of the atom, or molecule of interest. I_p^H is the ionisation potential of atomic hydrogen, l and m the orbital angular momentum and magnetic quantum numbers of the atom respectively. ε_0 is the electric field amplitude and Γ is Euler's gamma function. The effective quantum number l^* and is given by $l^* = 0$ for $l < n$ and $l^* = n^* - 1$ if not (n is the principal quantum number).

Equation 1.3 is used to determine when tunnel ionisation is occurring within the time interval set in the equation (dt). This can be likened to a first order kinetics equation. It provides a description of the outgoing electron wave packets for a particular electric field. The model begins to break down when laser intensity is increased to a critical point at which the electrons can just flow over the energy barrier, this point is the critical intensity, I_c, is obtained by equating the maximum that can be induced by the

electric field in the effective potential to the ionisation potential of the bound electron and can be defined in equation 1.6,

$$I_c = 4 \times 10^9 (I_p[eV])^4 Z_R^2 W cm^{-2} \tag{1.6}$$

Ionisation potential here is expressed in eV and Z_r is the residual charge of the relevant atom of ion. Once the ionisation potential is overcome the atom or molecule will be ionised. After this point additional energy is required to allow ionisation to occur from the ion state as opposed to the neutral molecular state. This method has been used to examine and determine various laser intensities that have been required during experiments to ensure that high harmonic generation is not occurring form the ion state, and that there is sufficient laser intensity to generate harmonics.

1.2.3.1 Semiclassical Model of High Harmonic Generation

To be able to fully model the high harmonic generation process a quantum model is required. However, a good understanding of the generated radiation can be achieved by treating the process as semi-classical. In treating the process as semi-classical this enables us to characterise the process and provide mechanistic steps for the process. In 1994, Corkum proposed a semi-classical model to describe the steps that occur during the high harmonic generation, the model can be broken down into three main steps: ionisation, propagation and recombination.[32] As shown in figure 1.6

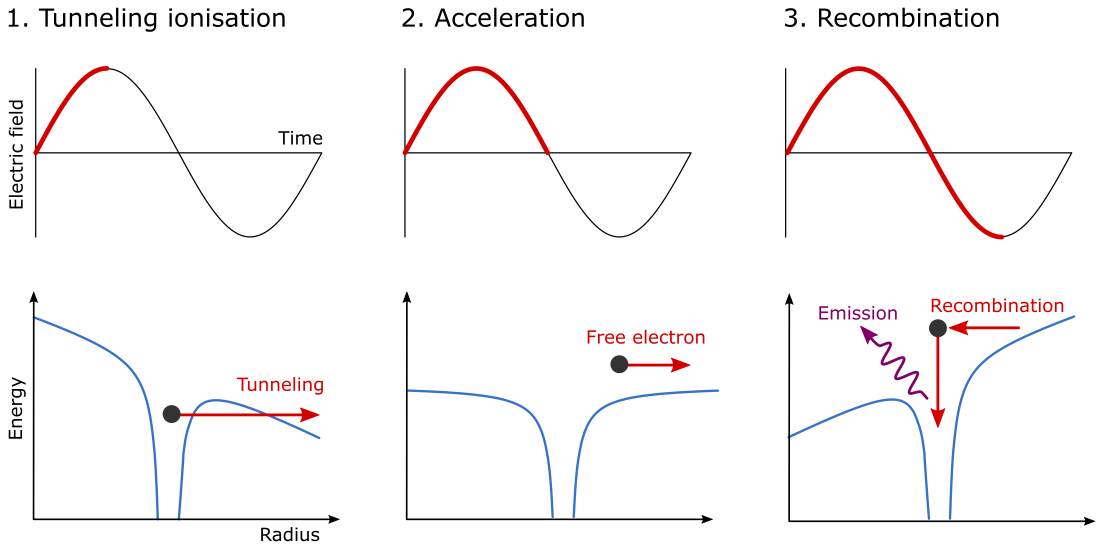

FIGURE 1.6: A diagram showing the three step model showing the different steps; (1) the electron tunnels out in the presence of a strong field, (2) the electron accelerates back towards the parent atom as the direction of the laser field changes, (3) recombination leading to the emission of XUV.

When a strong laser field interacts with an atom or molecule it can distort its Coulomb potential such that an electron can tunnel through the barrier. This electron is then set on a trajectory away from the atom or molecule. The propagation of the electron is often modelled classically using Newton's equations. The trajectories of an electron in a continuum are given by x the velocity is given by v and acceleration by a. The laser field is modelled as sinusoidal, $E = E_0 sin(\omega t)$, where E_0 is the magnitude of the electric field, ω is the angular frequency and t is a point in time. Several assumptions are made in this model; the electron has zero velocity at t_0, a position of $x = 0$ at $t = t_0$, the electrons release time $t = t_0$ and $t = t_1$ is the return time of the electron. The terms e and m are the mass and charge of an electron respectively.

$$x = \frac{eE_0}{m\omega}\left(\frac{1}{\omega}(sin(\omega t_0) - sin(\omega t) + (t - t_0)cos(\omega t_0)\right) \tag{1.7}$$

$$v = \frac{eE_0}{m\omega}(cos(\omega t_0) - cos(\omega t)) \tag{1.8}$$

$$a = \frac{eE_0}{m\omega}(sin(\omega t)) \tag{1.9}$$

The trajectory of the electron varies with the waveform, as the wave changes sign the electron changes direction. Given ideal conditions upon its return the electron will collide with the ion and this recombination step causes the emission of short wavelength radiation (XUV). Upon its return the electron gains kinetic energy due to its attraction to the ion, this additional energy helps in the production of radiation upon recombination. By substituting $\tau = t_1 - t_0$ into equation 1.8 it can be seen that the maximum energy is given by equation 1.10 and can be seen in figure 1.7:

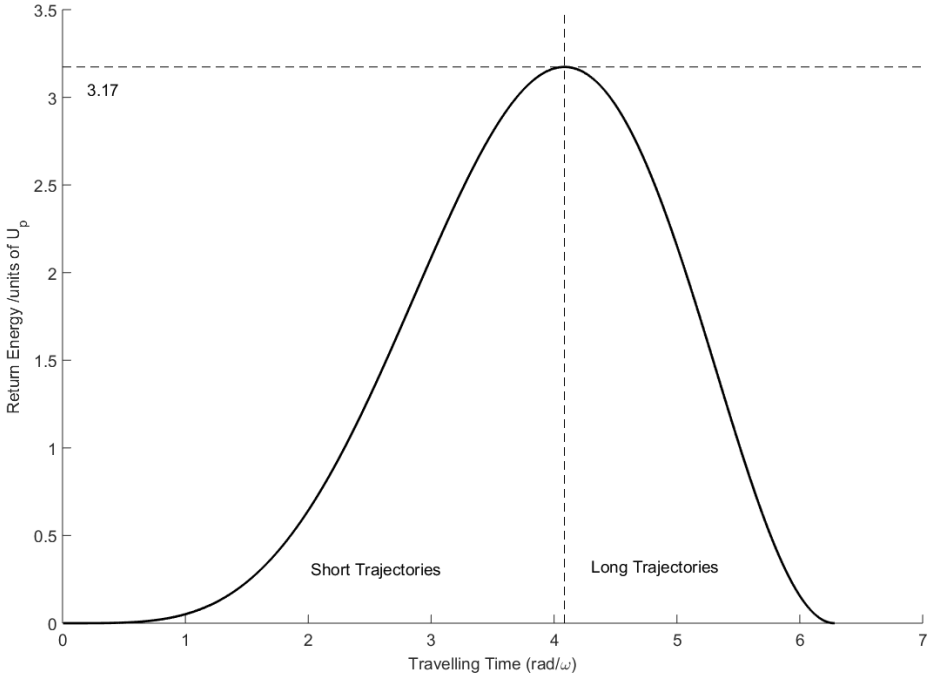

FIGURE 1.7: Energy gained by an electron in the laser field in units of U_p as a function of angular frequency. Long and short trajectory electrons are marked on the figure. It can also be seen the maximum energy gain is $3.17U_p$

$$E_{max} = I_p + 3.17U_p \tag{1.10}$$

Equation 1.10 is for the maximum energy harmonic (E_{max}) that can be generated.[36,37] I_p is the ionisation potential of the target species. From the pondermotive potential (U_p) equation 1.2 it can be seen that the maximum energy produced during harmonic

generation scales with wavelength.[38] However, the relationship between harmonic generation efficiency from a single atom and wavelength is given as λ^{-6} in terms of number of photons in compared to photons out. Such that a balance between energy and efficiency is often required.

In order to include non-linearity and recombination the quantum model would have to be used, in this, a time dependent Schrodinger equation in a strong field is solved. To solve this, assumptions are required: (1) The contribution of the wavepacket can be ignored for all states other than the ground state, (2) There is no depletion of the ground state, (3) The electron is treated as a free particle moving in an electric field with no atomic potential effects, however, some models move beyond this.

1.2.3.2 Quantum Model

The semi-classical model gives simplified yet qualitative description of high harmonic generation. Classical driving fields are used within the quantum model, as in the previous section. However, the electron is now treated as a wavefuncion inside a soft coulomb potential.[39] Previously it was treated as a point charge. A soft coulomb potential is a numerical requirement, a standard coulomb potential is described by,

$$V = -\frac{1}{4\pi\epsilon_0}\frac{e^2}{x} \tag{1.11}$$

ϵ_0 is the permittivity of free space and e is the charge of an electron. A singularity is created as x approaches 0, the solution to 1.11 tends to $-\infty$. The use of a soft coulomb potential avoids this problem, the Bohr radius (α_0) is introduced, as shown in equation 1.12.

$$V = -\frac{1}{4\pi\epsilon_0}\frac{e^2}{(\alpha_0^2 + x^2)^{\frac{1}{2}}} \tag{1.12}$$

To model the wavefunction as it interacts with the electric field of the driving laser and the soft coulomb potential, a time dependent Schrödinger equation is used as seen in equation 1.13.[40]

$$i\hbar\frac{\partial}{\partial t}\psi = \hat{H}\psi \tag{1.13}$$

$\hbar$ represents Planck's constant, ψ is the wavefunction of the electron. The driving field of the laser adds to the soft coulomb potential, leading to a potential barrier formed at specific cycles in the pulse. Equation 1.13 can be solved to model high harmonic generation. The wave-function is propagated and then the wiggle of the electron density is examined which produces the dipole.

1.2.3.3 A Typical High Harmonic Spectrum

From the three step model, it is apparent that one half-cycle after ionisation the electron turns back towards the parent ion to recombine when the laser electric field changes sign. Harmonics are produced twice each cycle, with each half cycle producing XUV. From this it can be seen that consecutive bursts lead to collisions from opposite directions, the spectral components will have the same amplitude but be in opposite phase, leading to destructive interference for even order harmonics, and constructive interference for odd harmonics. Normally only odd harmonics are observed in a high harmonic spectrum.

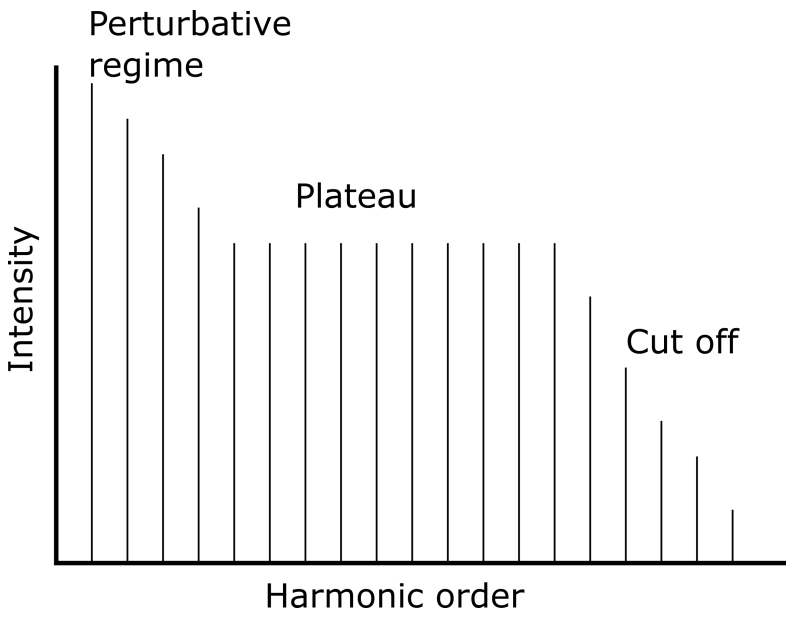

FIGURE 1.8: A schematic of a typical high harmonic spectrum showing the three different regimes, the perturbative, plateau and cut off.

A schematic of a typical spectrum as seen in figure 1.8 can be divided into three parts: the perturbative regime at low orders, the plateau region at intermediate orders and the cut off region at the highest orders. The perturbative regime is one in which perturbation theory can be applied, the harmonics in this region decrease as a power law, which can be defined as a relative change in one quantity causes a proportional relative change in the other quantity. The plateau region contains harmonics with minimal changes in intensity with increasing harmonic order. Within the plateau region two different electron trajectories are observed as shown in figure 1.7 these electrons return with the same kinetic energy leading to harmonics of the same frequency being produced.[41] Following the plateau region is the cut off region. The cut off photon energy is determined by equation 1.10.

1.2.3.4 Phase Matching

It is important that the harmonics being produced do not destructively interfere within the sample, so the generation process is as efficient as possible. For this to be achieved the phase of the driving laser field at the moment of generation must be the same phase as the harmonics that have been produced already within the generating medium. If

all the phases are the same at the moment of generation then the harmonics will add constructively, leading to the largest possible signal and the phase mismatch (Δk) will be zero. This can be shown:

$$\Delta k = k_q - qk_f = 0 \tag{1.14}$$

where k_f is the fundamental wave vector, k_q is the harmonic wave vector and q is the harmonic order. There are four factors that contribute to phase mismatch in a high harmonic experiment. These are a geometric term (Δk_{geo}), a neutral atom term(Δk_{na}), a free electron term (Δk_{fe})and an atomic phase term (Δk_{at}).

$$\Delta k = \Delta k_{geo} + \Delta k_{na} + \Delta k_{fe} + \Delta k_{at} \tag{1.15}$$

This indicates that phase mismatch is dependent upon a number of things. Experimentally, Δk_{geo} has a longitudinal dependence making the position of the gas jet relative to the focus critical.[42] Δk_{na} comes from different frequency components travelling through the medium with different refractive indices. This shows that the length of the interaction region can also effect phase matching, this can be controlled by changing the pressure of the gas at the jet, giving more or less plasma. Δk_{fe}, is due to the fact that high harmonic generation requires ionisation to occur so there will be a free electron component. The free electron term is only considered for the fundamental wavelength because the effect of the XUV is small. The magnitude of this term is affected by all the electrons that do not recombine, therefore power (intensity) affects the magnitude of this. The final term is the atomic phase Δk_{at} it is the intrinsic phase of the harmonic as a result of the kinetic energy gained from the electron in the driving field. This is the length of time between ionisation and recombination; for short trajectories this is a small effect but for longer trajectories this is larger.[43] This can also be controlled by focal position, as this can be used to optimise the trajectories that are observed.

1.2.4 High Harmonic Spectroscopy

The first high harmonic generation experiment in gases was performed by McPherson et. al. in 1987 where the highest harmonic they observed was the 17th harmonic from neon.[44] Since then many studies have been done to characterise the harmonics produced, and gain and understanding into the mechanism of there production.[45,46] High harmonic generation has numerous different applications, ranging from spectroscopic measurements to imaging.[47–51] High harmonic generation is most commonly performed in the gas phase however, it has also been carried out on both liquids and solids.[52–54]

The nature of high harmonic generation is that high harmonics can be generated providing there is sufficient laser intensity to allow tunnel ionisation to occur. High harmonic generation is sensitive to electronic structure changes and therefore can be used as a probe of time dependent changes. High harmonic spectroscopy as a probe of chemical dynamics is windowless as high harmonics can be generated from any species that is present within the reaction. High harmonic spectroscopy is a complimentary technique to photoelectron spectroscopy. Photoelectron spectroscopy probes the ionisation matrix of a molecule, whilst high harmonic spectroscopy provides information about the recombination matrix of the electron that has been used during the high harmonic generation process. In principle both techniques are windowless techniques that can be used in order to study chemical dynamics.

Shiner et al. demonstrated that high harmonic spectroscopy can provide a unique insight into the electronic structure of atoms and molecules.[55] The photoionisation cross-sections measured with a synchrotron light source can be related to the high harmonic spectra obtained in xenon. Xenon has giant inner shell electron resonances and these have been observed within spectra obtained. They also observed the Cooper minimum in krypton during HHG which allowed them to perform measurements on the recolliding electron wavepacket spectrum. This was then used in order to unravel the multiple pathways that they observed in xenon. The results here show that high harmonic spectroscopy opens the possibility to study electronic structure as high harmonic spectroscopy has shown sensitivity to the changes in the electronic structure and correlations in inner shells of molecular systems.

Shiner et al. demonstrated that a single beam experiment can lead to a new understanding of electronic structure within atoms. Work carried out by Wörner et al. demonstrates that a chemical reaction can be followed using high harmonic spectroscopy.[56] The experiment they carried out was on bromine, which when pumped with 400 nm leads to a dissociation reaction leading to the production of Br and Br^+. As the reaction progresses in time they make observations of the bond length change, which leads to the final dissociation of the molecule. The sensitivity in the bond length change is observed because when the bond length corresponds to a half integer of the de-broglie wavelength of the returning atom they see a two centre interference effect leading to a destruction in a particular harmonic peak at that time.

Since the initial demonstration that high harmonic spectroscopy can be used to monitor the photodissociation of molecules, several different molecules have been studied, all relatively small in size compared to the much larger systems that have been studied using photoelectron spectroscopy.[57] A year after the study on bromine Wörner et al. carried out a study on NO_2 this study showed that high harmonic spectroscopy revealed oscillations in the electronic character of NO_2 when the photo excited wavepacket crosses a conical intersection.[58] This showing that high harmonic spectroscopy is a powerful tool when examining non-adiabatic chemical reaction pathways.

High harmonic generation has also been performed upon a number of different hydrocarbons, showing that high harmonic spectroscopy has the potential to be extended into much larger biomolecules.[59] Despite this potential a limited number of systems have been studied using high harmonic spectroscopy. This is due to the complexity in analysing and gaining an understanding of the results, as can be seen from the small number of molecular systems the technique has been used to study. However, High harmonic spectroscopy is potentially a very powerful tool to study chemical dynamics. It is capable of giving time resolved information about structural and electronic changes through chemical reactions.[60] Compared to other ultrafast spectroscopy methods, high harmonic spectroscopy is not limited by Frank-Condon overlaps or selection rules. Ionisation potentials only effect the cut off energy of the observable region, therefore, reaction intermediates, transition states and conical intersections can potentially

be interrogated.

1.3 Summary

To summarise, chemical dynamics are complex and in order to make observations of these process several different probes can be used. The choice of probe can be any of the previously mentioned techniques, providing they are sensitive to the type of motion that the molecule is undergoing. The understanding of the time scales of molecular dynamics has progressed significantly from microsecond measurements through to femtosecond and attosecond measurements of different dynamic processes.

To enable chemists to gain a complete understanding of a reaction co-ordinate in the case of photoelectron spectroscopy a probe that has sufficient energy in order to ionise all the species found within the reaction is required. Alongside short laser pulses giving the temporal resolution that is required in order to make observations of the processes that are occurring. In order to obtain high energy probe photons with the required temporal resolution high harmonic generation can be used to produce these. This has enabled measurements to be performed on a small molecular system which directly dissociates Br_2, more complex systems have also been examined in this way but have shown that the experimental measurements needs some finesse before larger systems can be studied with confidence.

An alternative windowless technique is high harmonic spectroscopy which looks at the recombination matrix of an electron as opposed to the ionisation matrix which is examined using photoelectron spectroscopy. This method has shown promise in small molecular systems but as systems gain size the complexity of the results increase and gather a full understanding of the results is challenging.

Photoelectron spectoscopy measurements have been performed to monitor the dissociation reaction of both NH_3 and CS_2, including the development of this technique in order to use a high harmonic generation probe, so that a complete reaction co-ordinate can be studied. A high harmonic spectroscopy experiment has been developed and built so

that measurements can be made on small molecular systems, details of the development of the system and measurements on CCl_4 will be presented within this thesis.

Chapter 2

Experimental

In this chapter the experimental details will be discussed at length. Throughout the work presented in this thesis two laser systems have been used. In this section the details of the beam lines will be provided, alongside the end stations that have been used in order to perform the experiments. Photoelectron spectroscopy experiments have been performed at Artemis in the Central Laser Facility using both velocity map imaging and time of flight spectrometers. High harmonic spectroscopy experiments have been developed in Southampton, an overview of the laser system and beam paths will be given in this chapter with more details of the development of the beam line will be provided in chapter 3.

2.1 Introduction

Throughout the experiments presented in this thesis we have used a variety of laser systems, vacuum systems, detectors and spectrometers which will now be discussed. Two laser systems were used for the work presented. The laser system at Southampton was used for the development of a high harmonic spectroscopy experimental system this work is presented in chapters 3 and 4. For the photoelectron spectroscopy experiments that were carried out at the Central Laser Facility on Artemis the results are presented in chapters 5 and 6. The laser system at Southampton is used and maintained by the

different students that are based within the laboratory, whilst at Artemis the laser system is maintained by the staff at the facility, and as such only a general overview of the Artemis system and the beam path that we used will be presented here. The various strong field spectroscopic measurements performed throughout this work require an ultrashort laser pulse. In order to achieve this several different interconnected experimental components are required. This primarily includes; a base laser system capable of producing high intensity pulses, optical components that allow us to produce the different pump and probe pulses which have different intensities, and or wavelength, a vacuum system and various detection methods. The different experimental tools used in order to conduct both high harmonic spectroscopy and photoelectron spectroscopy experiments on a variety of different molecules are also described in detail.

2.2 Southampton Laser System

The laboratory in Southampton has an ultrafast femtosecond laser system. The laboratory is shared amongst several different users and groups who all have role in maintaining the system. The main focus of the work that I have carried out in Southampton has been to develop and perform high harmonic spectroscopy experiments on different molecular systems. In order to perform high harmonic generation a peak intensity in excess of 10^{14} Wcm^{-2} is required. The relationship between peak power and different laser parameters is given in equation 2.1.

$$P_{peak} = \frac{P_{avg}}{f_{rep}\tau a} \tag{2.1}$$

The peak power (P_{peak}) of a laser system is related to the average power (P_{avg}), pulse length (τ) and repetition rate (r_{rep}) and a is the area. The laser system used throughout the experiments has a fixed repetition rate of 1 kHz. For the desired peak power to be achieved a short pulse and high average power is therefore required. The average power is normally limited by the components within the laser system, whilst the pulse length is controlled by the bandwidth that is produced by the oscillator and gain narrowing in

the amplifier. In order to achieve these intense laser pulses several stages are used, each stage can be seen in figure 2.1.

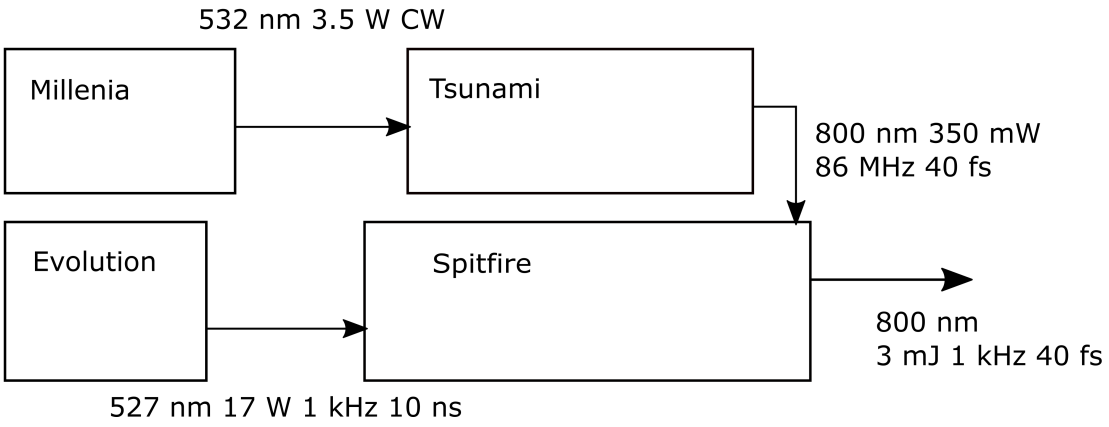

FIGURE 2.1: A diagram to show the layout of the Southampton laser system, showing each unit involved with producing the overall laser pulse. Initially the Millennia pumps the Tsunami producing the seed for the Spitfire, the Spitfire is pumped by the Evolution resulting in the final output pulse from the Spitfire

Figure 2.1 shows the overall system which is comprised of a Spectra Physics Millennia which is used to pump the Spectra Physics Tsunami (Ti:Sapphire) oscillator. The oscillator produces 350 mW, 40 fs pulses at 86 MHz repetition rate. The oscillator pulse goes into the amplifier, Spectra Physics Spitfire Pro Chirped Pulse Amplifier (CPA), this is pumped via the Positive Light Evolution 20. The Spitfire is able to increase the power of the pulse from 350 mW to 3 W with a pulse length of 40 fs at a 1 KHz repetition rate, more than sufficient to allow us to perform high harmonic generation, and therefore carry out experiments.

At the start of the system is the Spectra Physics Millennia; a Nd:YVO_4 diode based laser system which provides approximately 3.5 W of continuous wave radiation (CW) at 532 nm, to the Spectra Physics Tsunami (oscillator) to generate the seed for the amplifier. In order to produce a pulse train from the oscillator mode locking is used. This allows the light to pass through the cavity in such an alignment that is more energetically favourable for the light to propagate through the system as a short train of pulses as opposed to a CW. Repetition rate of the oscillator is determined by the round-trip time,

which is dependent upon the cavity length which is on the order of a few metres leading to a repetition rate of approximately 86 MHz.

It can be seen by mode locking that the peak power is increased from the initial CW input. If an average output power of 350 mW, pulse length of 50 fs and a 86 MHz repetition rate leads to a pulse energy of approximately 10 nJ. This demonstrates that modelocking leads to an improvement in the peak intensity. This improved is still not significant enough to perform high harmonic generation so an amplifier must be used in conjunction with this to achieve such a large gain in peak power.

Mode locking occurs when several wavelengths of light are taken and combined together leading to both constructive and destructive interference between the different wavelengths that are being combined.[61] The broader the wavelength range that goes in the shorter the pulse that comes out. If you consider a number of sine waves being coherently combined, the greater the number of different frequencies, the shorter the region where only constructive interference can occur and therefore the shorter the pulse that will be produced. Mode locking can be performed in two main ways; actively and passively, both of which are used within Southampton. To initially start the process of mode locking an Acousto-Optic Modulator (AOM) is used. The reason for using this is that it offers more stability and increased repeatability over the conventional method of applying force to an optic. If light is considered in the frequency domain and has an optical frequency (ν) and is modulated in amplitude at a frequency (f), the resulting side-bands have optical frequencies of the $\nu - f$ and $\nu + f$. The production of side-bands leads to the broadening of the CW pulse and starts the production laser pulses. Once this process has started passive mode locking takes over, this is where the overall path length of the cavity allows the gain medium to be saturated at a particular time leading to the production of a laser pulse.

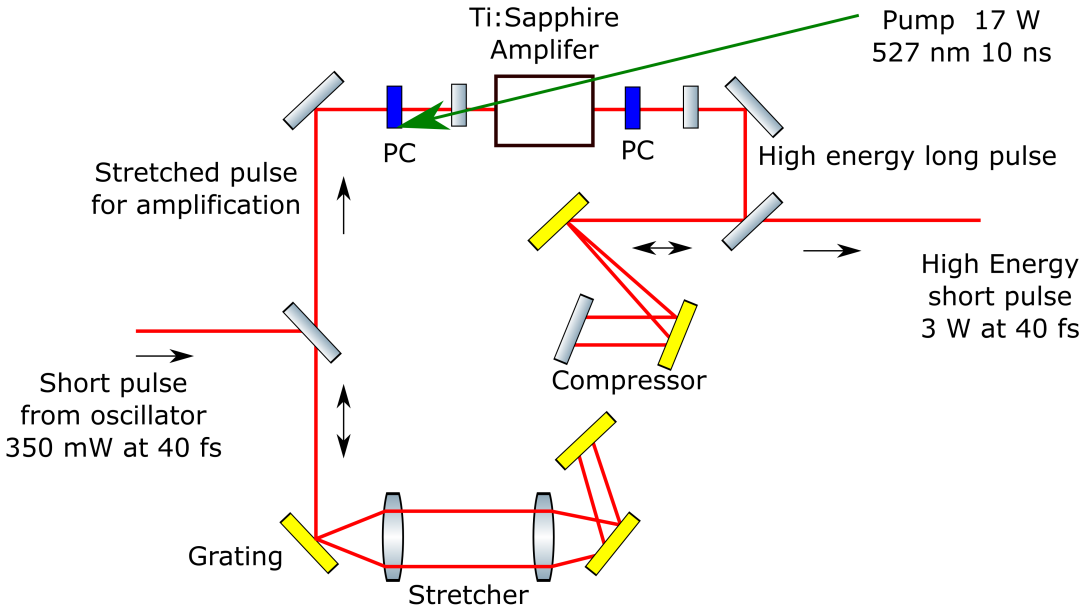

FIGURE 2.2: A schematic to show a chirped pulse amplifier configuration, firstly the oscillator pulse goes to the stretcher, it is then amplified in the Ti:Sapphire crystal which leads to a long high energy pulse. The pulse is then compressed in the compressor resulting in the high energy short pulse output.

The seed is then passed into the amplifier (Spitfire Pro CPA), the amplifier is then pumped by the Positive Light Evolution 30, which is a Nd:YLF diode based pump laser outputting green light at 527 nm. To achieve a sufficient peak power, the pulse produced from the Tsunami (oscillator) is passed into a CPA, in this instance the Spitfire. A general configuration of a CPA laser can be seen in figure 2.2 with all of the key optical components of the amplifier. The amplification occurs within a gain medium in the laser system at Southampton this is Ti:Sapphire crystal. The gain occurs in a similar mechanism to that observed during fluorescence. The pulses that are produced from the oscillator first need to be stretched as they have high pulse energy (10 nJ based upon 350 mW average power, pulse length 50 fs and 86 MHz repetition rate). If the pulse was not stretched first, this would lead to pulse distortion via self focusing and self modulation in the gain medium (due to a changing refractive index leading to a blue shift in wavelength). Once the pulse has been stretched it passes through the Ti:Sapphire crystal and is then amplified with the combination of the pump pulse

from the Evolution. The amplifier has a regenerative cavity, where the light pulse that is passed into the amplifier does several round trips in order to produce a pulse of maximum power. Overall the final pulse has done 13 round trips of the cavity, the number of round trips is controlled by two pockel cells within the amplifier which are used to switch the pulses in and out of the cavity. The timings of these is controlled via electronics, and can be tuned for optimal amplification of the pulse. Once the pulse is amplified it is then compressed, this is done using a pair of gratings in order to disperse and recombine the different frequencies. Leading to the production of an 800 nm 3 mJ 40 fs laser pulse at a 1 kHz repetition rate.

2.2.1 Laser Diagnostics

In order to check that the laser is working to the desired specification there are several diagnostic tools at our disposal in Southampton. There are three main parameters that are routinely measured across the system; power, the spectrum of the oscillator output and the overall output pulse length and spectrum. The power is measured between the Tsunami (oscillator) and the Spitfire (amplifier). Ideally the measured power here will be 350 mW, this measurement is taken using a thermal power meter. The spectrum is also measured at this point for two main reasons. Firstly, to ensure that the central wavelength that is being passed into the Spitfire is consistent. Secondly, it is checked to aid in maximising the bandwidth that is produced by the Tsunami during mode-locking. The power is also measured after the amplifier. Generally speaking 3 W is the optimal output as this is the maximum achievable power. This is also measured with a thermal power meter. If something looks awry the spectrum can also be measured at the output of the amplifier, this tends to only be done if the pulse length is much longer than expected. The spectra are measured on an Ocean Optics HR2000 CG-UV-NIR. Various input fibres can be used with this spectrometer in order to measure different wavelength regions. The broader the aperture of the fibre the shorter the wavelength that can be measured.

The pulse length is less straight forward to measure as the ultrashort pulses have to be measured against themselves, as there is no shorter event to be able to measure

them against. In order to do this in Southampton we use a Swamp Optics Grenouille FROG (Frequency Resolved Optical Grating) this is permanently in place with a 2% beamsplitter from the main beam used for diagnostics.[62,63] In figure 2.3 a diagram of the layout of general FROG system can be seen, A FROG splits the beam into two, one beam is then delayed with respect to the other, through the extension of its path length. The two beams are then crossed in a non-linear crystal, BBO (Beta Barium Borate) the second harmonic signal is the recoded onto a spectrometer. The FROG measurement gives a spectrogram of delay vs frequency which allows the overall pulse length to be calculated. An iterative Fourier phase retrieval algorithm is then used to reproduce the spectral phase of the pulse, meaning that coherence can be checked simultaneously. A Grenouille FROG differs from the standard FROG as it has no moving parts and uses a prism in order to separate the beam into two, in order to measure the pulse length.

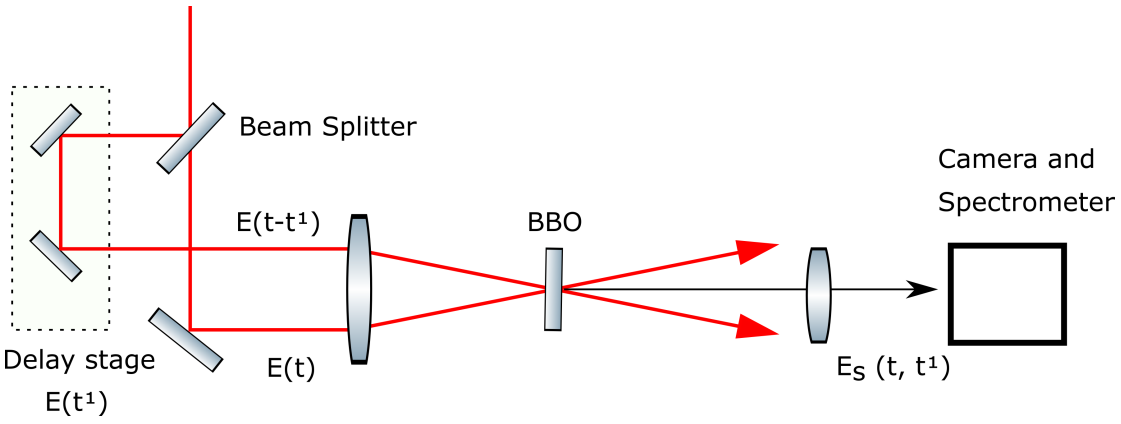

FIGURE 2.3: A diagram to show the optical path inside the FROG, t represents the initial pulse t^1 is the delay induced by the delay stage and E_s is the measured signal.

2.2.2 Harmonic Generation and non-linear Optics

BBO's are non-centrosymmetric crystals that are used within optics to generate harmonics through non-linear properties.[64] Harmonic generation can be put as one simple expression but to understand the process this needs expanding:

$$P(t) = \epsilon_0 \chi E \tag{2.2}$$

P is the induced polarisation of the charge density within the BBO crystal, ϵ_0 is the permeative free space, χ is the susceptibility of a material to the electric field leading to a degree of polarisation, and E is the electric field. By expanding this as a Taylor series function you arrive at the following:

$$P = \epsilon_0(\chi_1 E_0 sin(\omega t) + \epsilon_1 \chi_2 E_0^2 sin^2(\omega t) + \epsilon_2 \chi_3 E_0^3 sin^3(\omega t)\dots) \tag{2.3}$$

In equation 2.3 we define the electric field as $E = E_0 sin(\omega t)$ where ω is the angular frequency of the light, with ϵ being a constant which changes with respect to the order of the term. For a non-centrosymmetric system all the even terms are non-zero, due to symmetry. If there is an even oscillating field and an odd distribution this leads to zero net effect and therefore all odd terms are zero. This is how the second harmonic can be generated through the use of non-linear optics. Therefore for a fundamental beam of 800 nm the second harmonic would be 400 nm. The 400 nm generation process is second harmonic generation, and this looks at second term in equation 2.3. Using trigonometric identifiers:

$$sin^2(\omega t) = \frac{1 - cos(2\omega)}{2} \tag{2.4}$$

Equation 2.4 shows that the light is converted from 800 nm to 400 nm in the crystal. In order to generate the third and fourth harmonics used in chapters 5 and 6 sum frequency generation is used this combines the 400 nm and 800 nm or the 266 nm and 800 nm respectively. Once again using trigonometric identifiers and equations 2.3 and 2.6 in this case the electric field can be written as $E = (E_1 sin(\omega_1 t) + E_2(sin\omega_2 t))^2$.

$$sin(\omega_1)sin(\omega_2) = \frac{1}{2}[cos(\omega_1 - \omega_2) + cos(\omega_1 + \omega_2)] \tag{2.5}$$

Where ω_1 and ω_2 are 800 and 400 nm respectively (or 800 and 266 nm for fourth harmonic generation), there is a change of unit here between frequency and wavelength but these are easily interchangeable using $c = \lambda\nu$. There is clearly an energy change here. This is

conserved throughout as one photon is produced during this process for every two that go in, as seen in equation 2.6, where ω represents the frequency of light:

$$\omega_3 = \omega_2 \pm \omega_1 \tag{2.6}$$

2.2.3 Optical Paths

Initially, a single arm experiment was performed in order to generate harmonics and gain an understanding of the process. Following this, a pump-probe experiment was set-up in order to carry out some simple measurements of molecular dynamics.

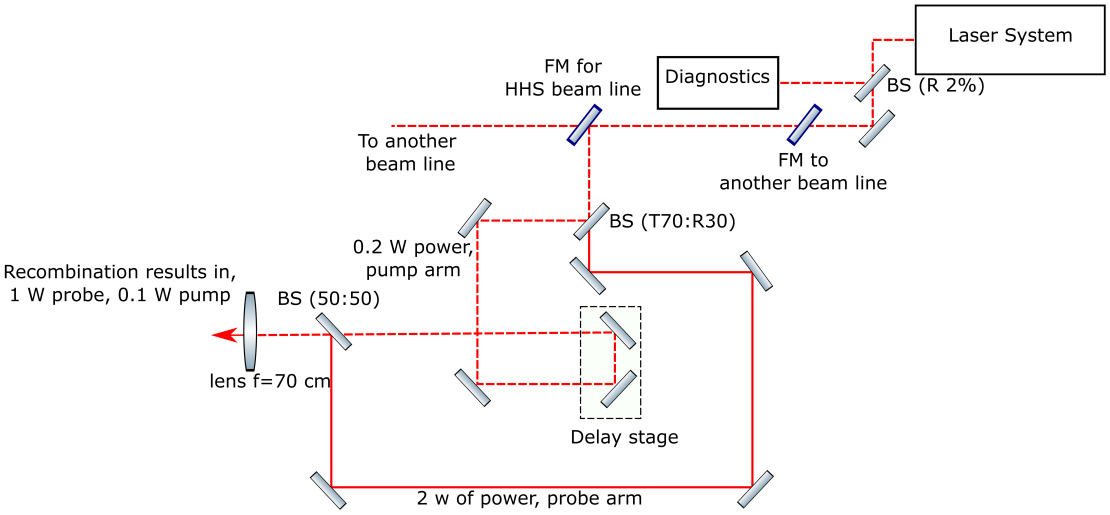

FIGURE 2.4: A diagram to show the optical path used in Southampton for pump, probe experiments, beamsplitters are shown as BS, and flip mirrors are shown as FM.

In figure 2.4 the beam path for the experiment can be seen. There are two arms to the experiment, this is split by a 70:30 beam splitter, in order to create one arm which is much more intense than the other. The pump arm, the weaker arm (30), is delayed relative to the probe arm by using a delay stage. The stronger arm (70), the probe arm, has a half wave plate within it in order to control the amount that passes through the final beam splitter 50:50 is used to recombine the two beams co-linearly. The delay between the two arms is controlled using a Newport delay stage, this is a motorised stage

with a range of 15 cm. Once the two beams have been recombined they are then focused with a 70 cm focal length lens into the interaction region. After recombination, temporal overlap between the pump and probe beams needs to be found. This is done by placing a BBO crystal after the beam splitter where the two beams are recombined. Using a half waveplate in the probe arm of the experiment the power in this arm is reduced so it as a close in energy to the pump as possible. The delay stage is then scanned from one end to other and the interference between the two arms at time zero results in a flash in the blue light that is being generated in the BBO due to the increased intensity. Once the time zero position has been found the spatial overlap can be optimised by the interference fridges between the two beams, maximum overlap results in the overall beam shape being circular with no stripes going across it either horizontally or vertically.

2.3 Artemis

The second of the two laser systems used for the work that will be presented within this thesis uses Artemis at the Central Laser Facility, Didcot. Artemis is a facility that offers ultrashort laser and XUV pulses, it has many end stations available and can be used to perform several different types of experiments including time resolved spectroscopy in gases, liquids and condensed matter, as well as XUV imaging. The Artemis facility provides ultrafast laser pulses from a Ti:Sapphire CPA laser system at 780 nm. The laser system is a KM Labs RedDragon. This employs a two-stage amplification leading to a maximum output of 11 mJ. Both amplifier stages require the Ti:sapphire crystal to be cryogenic cooled because of the additional heat load that is added by the multi-pass system. The cryogenic cooling system uses helium gas, in order to reduce the temperature of the Ti:sapphire crystal to approximately 50 K.

2.3.1 Overview

The laser system has the standard multi-pass bow tie configuration in the amplifier as seen in figure 2.5. This leads to number of passes of the amplifier crystal with a high level of overlap, the additional passes lead to highly efficient gain in the amplifier crystal.

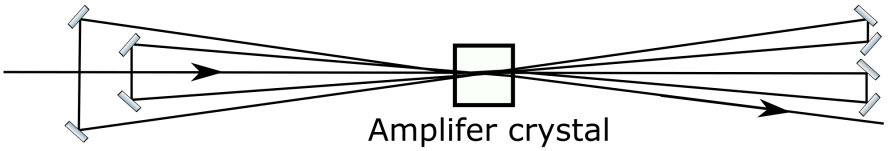

FIGURE 2.5: A diagram to show the beam path of a multi pass amplifier in the bow-tie configuration.

The output wavelength of the amplifier is 800 nm which can then be tuned to a range of 235 nm to 15 microns, using an Optical Parametric Amplifier (OPA) enabling the users of the facilities to have a many wavelengths at there disposable. The OPA was not used during any of the experiments we have carried out, because unfortunately it cannot be tuned to the 200 nm UV pulse that is required to pump the molecules that we wish to study. The laser has two compressors, enabling the optimisation of both pump and probe beams to be carried out individually. The two compressors have been invaluable throughout the experiments we have carried out at Artemis. The ability to compress each arm individually has enabled us to optimise both the cross correlation times in the experiment and the pulse energy produced during the high harmonic and fourth harmonic generation processes. A fourth harmonic generation pump has been used with two different probes, 400 nm, and high harmonic generation for the measurements that have been performed at Artemis. Once the pulse has been compressed and travelled down the bench it arrives at the vacuum system which it travels down to finally reach the end station that is being used for the experiment.

The beam line consists of several vacuum chambers that allow for high harmonic generation, wavelength selection and focusing of the harmonic beam these are described in section 2.3.2.2.

2.3.2 The Optical Path and the Beam Line

2.3.2.1 Optical paths

In order to get the light into the various chambers so it can interact with a sample and to allow both the pump and probe arms to be recombined, several optics are required.

Figure 2.6 shows a schematic of the optical path that has been used to perform the different experiments that have been carried out at Artemis.

The probe arm of the experiment comes out of the laser and then has a fold in it to ensure that the path length of the pump and the probe match up as closely as possible. Following the fold in this beam it is then passed into compressor one. When the beam exits the laser it is uncompressed, because travelling a large distance across the table whilst compressed can lead to the pulse being distorted via its interactions with the air. This is particularly important for high harmonic generation as optimisation of the pulse length leads to an increase in overall photon flux. Pulse distortions due to interactions with the air have a significant effect within the fourth harmonic generation set-up the distance from the second compressor to the experiment is long approximately 8 m. After the first compressor, we perform second harmonic generation in order to turn the fundamental 800 nm beam into 400 nm.

The photon energy that is required to make a full observation of all photo dissociation intermediates and fragments needs to be greater than the ionisation potential of the various fragments. The energy range which can be used has two key criteria, energy over the ionisation energy for the fragments of a molecular reaction is required but the total energy that can be used is limited to being below the ionisation potential of helium 24.6 eV. Helium is commonly used as a carrier gas and due to its high ionisation potential it remains unobservable in the overall spectrum. This limits the harmonic energy either to 16 eV or 21 eV. The next lower energy harmonic of 11 eV limits the energy available for one photon ionisation and therefore all molecular fragments would not be observable. The next higher energy harmonic of 26 eV would lead to the ionisation of helium therefore it would be observed within the experiment and overwhelm the overall signal within the experiment as generally most gas mixtures are 5% target and 95% helium. The selection of the harmonic used during the experiment is based on which has the most photon flux. The harmonics are generated with 400 nm beam as opposed to 800 nm as we have found that by using 0.5 W of 400 nm we achieve much greater photon flux at 21 eV approximately 10^10 photons per second. Photon flux at the required energy is key to

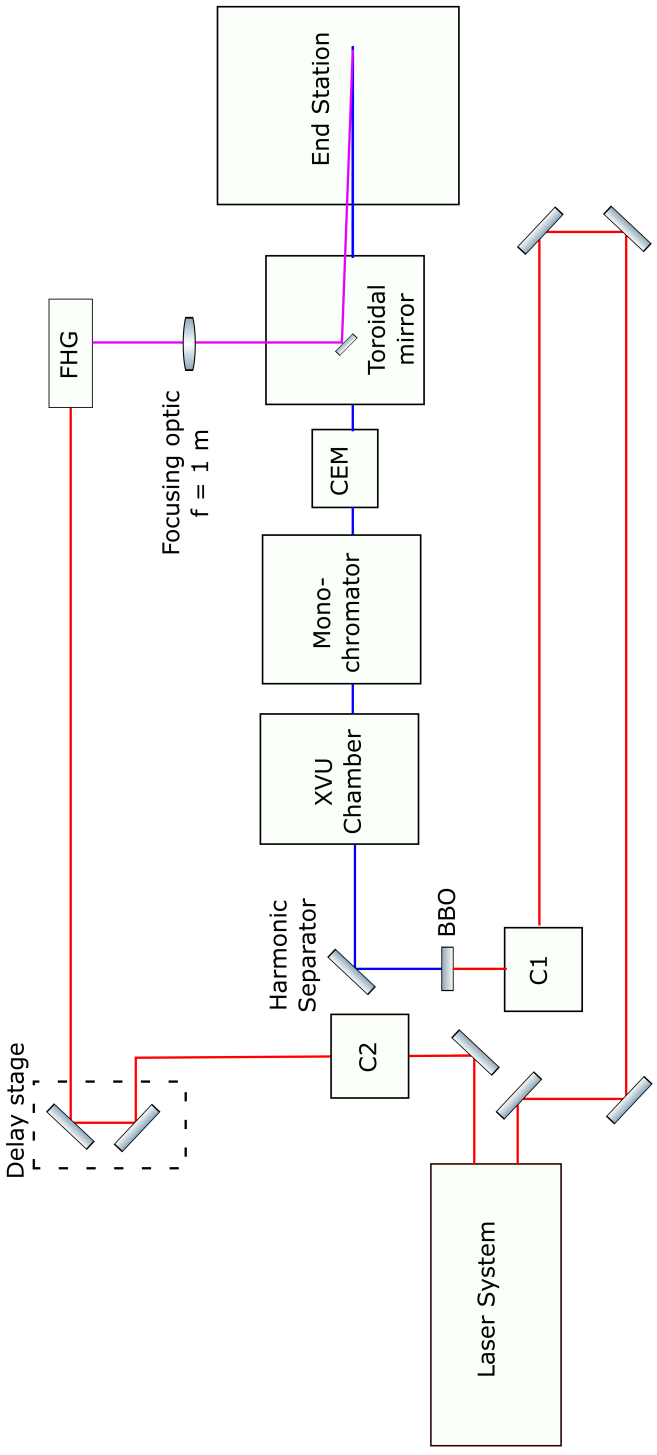

FIGURE 2.6: The beam line at Artemis, including the optical path used, C1 is compressor one, C2 is compressor two and FHG is fourth harmonic generation. The beam is split before it leaves the laser system, one arm is used for the probe, this goes to C1, this is frequency doubled in the BBO, a harmonic separator is used to remove the 800 nm, high harmonic generation is performed using the 400 nm beam. The harmonics are generated in the XUV chamber, the desired wavelength is selected in the monochromator, then the beam passes the CEM chamber into the toroidal mirror chamber where it is focused into the interaction region of the end station. The pump beam leaves the lasers, to the delay stage to control the relative delay between the two pulses, fourth harmonic generation is performed and the beam is then focused and folded into the interaction region of the end station using a D shaped mirror in the toroidal mirror chamber.

these experiments as it will reduce the collection times and therefore make observations possible.

The pump beam is compressed as it leaves the laser and travels down the table, through a delay stage in order to control the relative delay between the pump and the probe beams. In the area just outside the toroidal mirror chamber, fourth harmonic generation is performed. In order to do this several steps are required, initially the beam is split into two using a 70 % transmissive beam splitter, the transmitted beam is then converted into the third harmonic. Third harmonic generation takes the fundamental beam, frequency doubles this into the second harmonic using a BBO crystal, then a calcite plate is used in order to compensate for the relative delays between the two frequencies (800 nm and 400 nm), with a wave plate in order to give both beams the same polarisation as during second harmonic generation the 400 nm light is generated with perpendicular polarisation, both the 400 nm and 800 nm are mixed in a BBO crystal resulting in the generation of the third harmonic 266 nm. The reflected arm 30 % is time delayed so that it arrives at the same time as the 266 nm beam and is crossed in a BBO crystal in order to produce the fourth harmonic, 200 nm. The figure 2.7 shows a schematic for the fourth harmonic generation set-up that was used throughout the experiments at Artemis.

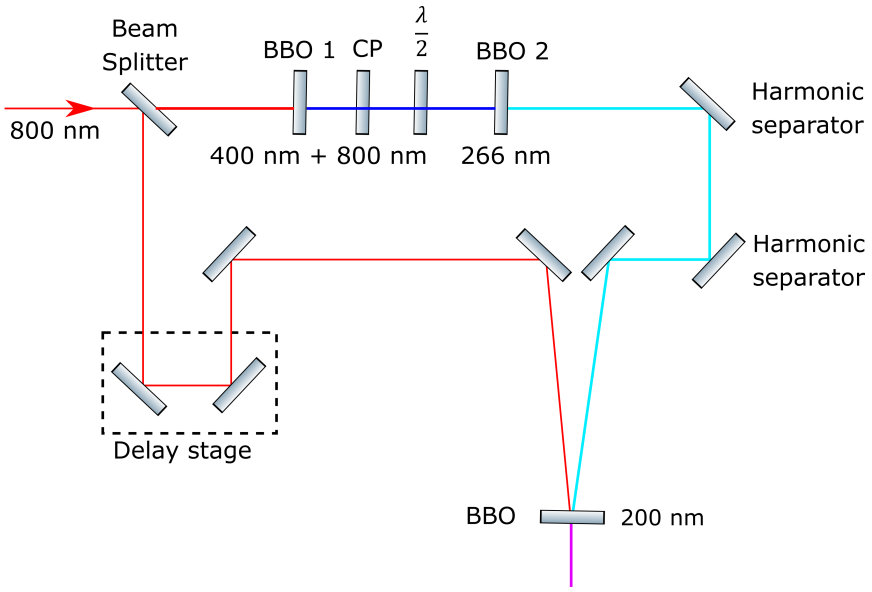

FIGURE 2.7: A diagram to show the optical set-up used to perform fourth harmonic generation to produce the 200 nm pump beam used throughout the experiments performed at Artemis. CP is the calcite plate, and $\frac{\lambda}{2}$ is a half waveplate.

Due to the set-up being so far (approximately 8 m) from the compressor, the pulse arrives already distorted from the interactions with the air, therefore the conversion efficiency for this process at Artemis is low. The set-up was initially built in Southampton before being transported up to Artemis for the beam time, in Southampton the distance from the laser to the set-up is much shorter and doesn't have the same issues so the conversion efficiency was considerably better. In Southampton there is approximately a 15% overall conversion efficiency from the input wavelength to the desired wavelength. At Artemis the overall conversion efficiency is dramatically reduced, especially during the fourth harmonic generation stage due to beam being distorted getting good spatial overlap in the final crystal is non-trivial and limits the efficiency such that overall from start to finish there is a 0.5 % conversion efficiency, starting with 5 W we end with 2 mW of 200 nm. Whilst the pulse distortions occur at Artemis fortunately there is ample input power from the laser system such that the generate fourth harmonic is sufficient enough to excite molecules and therefore photo-dissociation reactions can occur. Even though the distortions lead to a longer pulse length.

2.3.2.2 XUV Beam Line

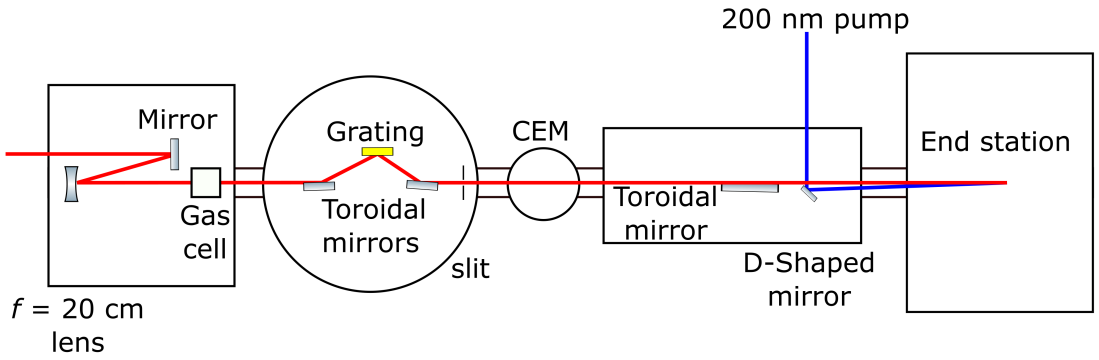

FIGURE 2.8: A diagram showing the details of the XUV-beamline at Artemis, with the chambers corrolating to those in Figure 2.6, with additional details shown. In the XUV generation chamber there is a focusing mirror into the gas cell, following this the monochromator with two toroidal mirrors and a grating, then the CEM, onto the toroidal mirror chamber with the toroidal mirror to focus the XUV beam and the D-shaped mirror to fold the pump beam into the interaction region, and finally the end station.

In figure 2.8, a diagram of the XUV beamline can be seen. The XUV generation chamber has a gas cell which is used for the high harmonic generation process, the gas cell is differentially pumped. The gas cell is encased within a cube which has apertures that allow the light to both enter and exit, this cube has a high throughput IGX vacuum pump attached to it in order to remove as much gas as possible. The chamber itself is also held under vacuum hence the gas cell is differentially pumped. Before the gas cell there are two steering optics and the focusing mirror, which are contained within the chamber. This prevents any damage to the window as the beam enters the chamber. If a focused laser beam is placed onto a window it can be burnt causing a hole to be formed in the throughput beam which would lead to odd phase matching conditions and a lack of power during the high harmonic generation process. The gas cell which is held within the small box as above, has a 100 μm aperture for the beam to enter the cell in order to interact with the gas, this leads to high harmonic generation. After the gas cell there is a gate valve, this gate valve has a window in it such that the fundamental laser beam can enter into the monochromator and proceed down the system so alignment can be

carried out however the window must be removed to allow the generated XUV to pass down the system.

The gas used in the gas cell in order to perform high harmonic generation is argon. The focal length lens used throughout these experiments is 20 cm leading to a very tight focus to produce the high intensities that required in order to perform high harmonic generation. The gas pressure is controlled by a mass flow metre, supplied by Bronkhorst. The mass flow metre can be set between a range of 0 and 200 SCCM, SCCM is a flow unit which measures standard cubic centimetres per minute. The high harmonic generation chamber has a roughing pump which is used to back a large turbo pump. The large turbo pump is used because of the high flow rates that can be used within the gas cell in order to maintain a working pressure in the chamber of 10^{-4} mbar when harmonics are being generated.

The monochromator is designed such that it maintains the temporal coherence of the generated harmonics.[65] When light enters into the monochromator it first interacts with the toroidal mirror in order to focus the beam onto the grating. The focused light is passed onto a diffraction grating, in order to select a specific wavelength of light. Following this, the selected wavelength of light is then passed on to a second toroidal mirror which re-collimates the beam. This beam is then passed through a diffraction slit as it exits the monochromator. The slit is used to control the amount of the selected wavelength that can exit the monochromator. The slit width can be controlled, this controls the frequency resolution of the light that is exiting the monochromator, as well as the amount. Uniquely, the grating within the monochromator is aligned such that the lines upon the grating are parallel to the beam. It has been found that this is the best way of maintaining temporal coherence whilst having high efficiency for the selected wavelength. The monochromator at Artemis covers a large range of 12-120 eV, this large range is achieved by having five different diffraction gratings that can be each individually selected depending upon the experiment that is being performed. The light then exits the monochromator chamber and heads towards the toroidal mirror chamber.

In between the monochromator and the toroidal mirror chamber sits a channel electron multiplier (CEM). The CEM is used to measure the harmonic spectrum and flux that is

being produced as seen in figure 2.9, this allows for the optimisation of harmonic flux and it also ensures that the desired wavelength is being isolated by the monochromator. The CEM is manufactured by Dr. Sjuts, the detector has also been commercial calibrated, so the energy of the harmonics that is being measured is known.

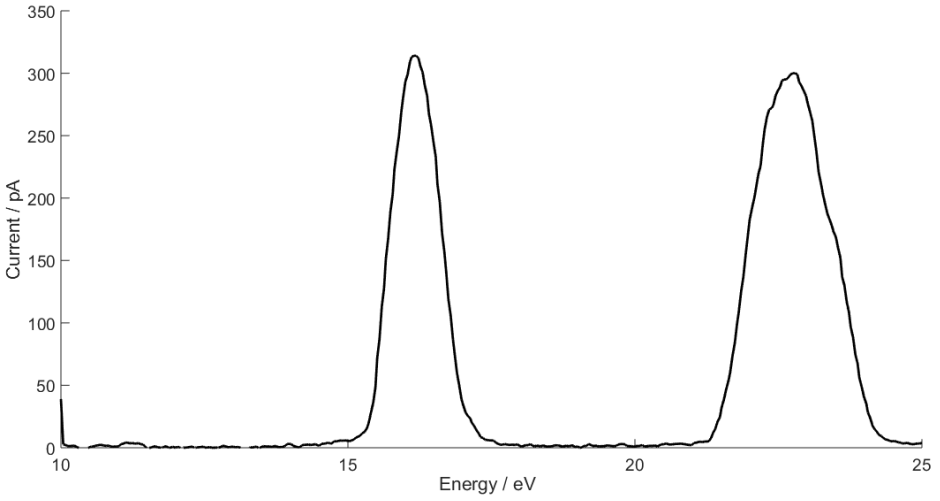

FIGURE 2.9: Spectrum obtained using the CEM to show harmonics produced at 400 nm, here it can be seen that there is slightly more photon flux at 16 eV.

The toroidal mirror chamber is a box chamber, within this there is a 1 m focusing toroidal mirror. The toroidal mirror is mounted on a series of highly precise stages, meaning that it has motion in the XYZ axis and its tilt and twist can also be controlled. This allows the position of the XUV focus to be optimised into the centre of the interaction region. The reason that the toroidal mirror must be movable is that whilst the experiment can be aligned using the fundamental beam there is always a small discrepancy between the position of the fundamental beam and the XUV. Sitting just after the toroidal mirror is a D-shaped mirror to fold the pump beam in as close as possible to the probe beam. Allowing us to have a smaller crossing angle as possible as the two beams enter the end station, leading to optimal overlap. The D-shaped mirror is also mounted on a movable mount such that this beam can be steered exactly on top of the XUV beam. This gives us some control of both beam position as they enter the end station. The focused beams are then in the end station chamber, and can be optimised to the centre

of the interaction region. The recombination of the two beams at the interaction region is what leads to a pump probe experiment being able to be performed.

2.3.3 End Stations

The Atomic Molecular Optical (AMO) end station can be configured so that either an electron Time of Flight detector or Velocity Map Imaging (VMI) detector can be used. We have conducted two different experiments at Artemis which have used the same main body of the end station with different detectors. The use of our chosen detectors meant modifications also had to be made to the top section of the end station.

When referring to the main body of the chamber we are specifically talking about the bottom section. This section contains a 1 kHz pulse nozzle (Amsterdam cantilever) with a 100 μm aperture.[66] Once the gas has passed through this aperture the resulting expansion passes through a 1 mm skimmer and enters the interaction region of the spectrometer. There are also two large turbo pumps attached to this section of the chamber enabling us to use reasonably high gas pressure in order to create molecular beams throughout the experiments have been performed. The base pressure of the end station is 1x10^{-7} mbar with a working pressure of 1x10^{-3} mbar when a molecular beam is being formed.

2.3.3.1 Velocity Map Imaging

The VMI spectrometer has been built by the Artemis staff and is of the standard Eppink and Parker three plate design.[67] It is comprised of a repeller, extractor and ground plate. The repeller plate sits below the interaction region, the other two plates sit above the interaction region. The skimmed molecular beam enters the interaction region through a 2 mm hole in the repeller plate. The extractor and ground plates also have a hole in the centre of them to allow either the electrons or ions to pass through to the detector, in our case we will be detecting electrons. The figure 2.10 shows the configuration of the plates within the VMI detector set-up that has been used throughout the experiments performed. The pulse gas jet and skimmer are used to provide the molecular beam for

the experiments. The repeller plate has a small aperture of 2 mm in order to maintain a flat field across the bottom of the detector, whilst the extractor and ground plates have larger apertures of 10 mm. The distance between the ground plate and detector is 30 cm, providing the flight time for the electrons before they arrive at the detector. Voltages are applied to the plates, the repeller plate has 1470 V and the extractor plate has 0.7 x R so in this case that is 1000 V. The back of the MCP detector has 2000 V applied to it throughout the experiments. The VMI spectrometer is surrounded by mu-metal shielding to prevent stray magnetic fields interacting with the spectrometer.

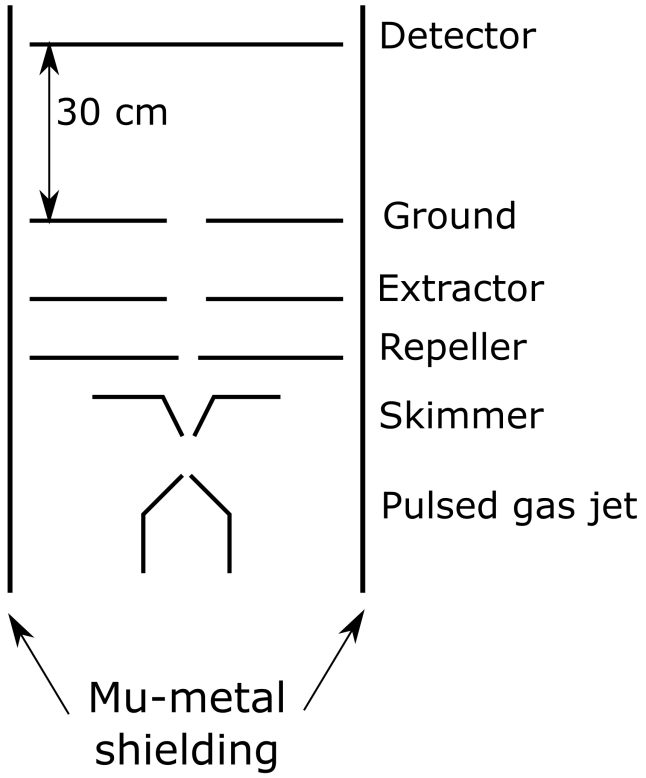

FIGURE 2.10: A schematic of the VMI, showing the three plate design up to the detector, the flight tube of 30 cm is shown. The apertures in the plates allow the electrons to pass through and up onto the detector, the reduced size in the repeller is maintain a flat field across the bottom of the detector. With the whole thing being surround by mu-metal shielding.

The detector consists of a 70 mm diameter MCP and phosphor screen which is then imaged using a sCMOS camera (PCO Gold Edge 5.5). Both the pump and probe beams are focused in the centre of the interaction region, directly below the centre of

the detector as seen in the figure 2.10 above, to ensure the images collected are well resolved. The crossing angle between the two beams is minimised to 3° . This was vital to increase the signal-to-noise ratio and therefore reduce collection times. The spatial overlap of the two beams was monitored using a LuAG:Ce phosphorescent crystal that can be placed into the centre of the interaction region. In order to place the crystal in the centre of the interaction region the voltages used on the VMI plates and detector must be reduced to avoid any possibility of electric shock. The crystal was mounted on an translation arm which could be manually pushed in and out of the chamber, a stop was put in place at atmosphere when the arm reached the centre of what would be the interaction region. The phosphorescence from the crystal was imaged using an electron multiplying charge-coupled device (EM-CCD). Both the pump and probe beams are linearly polarised in the plane of the detector, this is perpendicular to its flight axis, this is done to obtain angular information.

2.3.3.2 Time of Flight

The electron time of flight that we have used is a commercial spectrometer, made by Kaesdorf. The spectrometer is a ETF11 it is the the simplest design offered, collecting electrons only. It has a 3 mm aperture at the entrance and it is essential to get the interaction region central to this in order to get maximum collection efficiency. The drift tube can be used to both accelerate electrons into the detector and decelerate them depending on positive and negative voltages respectively. We found the optimal settings for the detector to be drift tube 10 V, its lowsest possible setting without it being off. The lens on 70 V which is used to pull in as many electrons as possible, this changes with energy range, and the MCP on at 2.25k kV.

2.3.3.3 VMI and Time of Flight comparison

Time of flight provides no angular information from a single measurement, whereas a VMI can provide angular information but often has lower resolution, increased noise and requires a large signal. This is due to everything here being angularly resolved so to get a good signal more photoelectrons are needed. The VMI required a lot cleaner

signal to noise ratio as well as a larger signal. Therefore making the small signal changes that are expected from a UV pump XUV probe experiment very difficult to see using a VMI spectrometer. In order to perform experiments that have an XUV probe small signal changes need to be observed and well resolved in terms of energy, this is why we chose to change away from the VMI. The small changes in signal and relatively closely spaced energy gaps can be better resolved using this method. The noise within a time of flight is also greatly reduced relative to that in a VMI, and there was generally less background signal present.

Chapter 3

Development of a New End Station for High Harmonic Spectroscopy

In this chapter I outline the development of a high harmonic spectroscopy experiment in Southampton, including the development and commissioning of a new flat field spectrometer. Results obtained using the experimental set-up that is developed throughout this chapter are presented in chapter 4.

3.1 Introduction

In order to perform high harmonic spectroscopy experiments several components are needed, all of which must work together to gather experimental data. These include; a laser with sufficient intensity to perform high harmonic generation, a gas supply to deliver sufficient density required to generate harmonics with enough intensity for detection, a vacuum system to ensure the generated wavelengths reach the detector and finally a detector in order to observe the generated harmonics. As seen in chapter 2, at Southampton we have a laser with a peak power that enables high harmonic generation to be performed. The laser is a femtosecond system supplied by Spectra physics with an

output power of 3 mJ at a 1 kHz repetition rate and a pulse length of 40 fs. As previously discussed in 1.2.2, high harmonic generation requires an intensity of 10^{14} Wcm^{-2} which is more than achievable with the system because of the overall peak intensity that can be produced from the laser. The components within my experiment consist of vacuum chambers, backing and turbo pumps, gas jet, and a spectrometer. These components must all be assembled in such a way that leads a successful experiment being performed and data being gathered. The experiment must be performed under vacuum conditions in order to prevent the absorption of the generated XUV by air, in order to record a high harmonic spectrum. High voltages are required in order to operate both the micro channel plate (MCP) and the phosphor screen which will be covered in more detail later. Therefore the spectrometer must be held under a low vacuum pressures (1×10^{-5} mbar) to prevent the ionisation of air and therefore inhibit arcing of the high voltages. This is important as arcing will cause deterioration of the detector and reduce its lifetime. In order to achieve low pressure in the spectrometer several pumps are used throughout the experiment.

Throughout my time in Southampton the experiment has gone through several iterations to get it into its current state. Within this chapter I will be describing the initial setup process of the experiment, its limitations and the extensive development work that has followed. The experiment in its final state has been used to obtain time resolved data, this will discussed in chapter 4.

3.2 Vacuum Chambers

Upon starting my PhD the experiment was a series of vacuum chambers on the laser table that were no longer functional and a lot of work was necessary to get the experiment back up and running. I will now describe the set-up as it was initially, following this I will discuss the limitations and changes that have been made over the course of my PhD.

The initial experiment was composed of two vacuum chambers and a spectrometer which has the ability to detect the generated XUV, and a gas jet in order to deliver gas to the experiment. A diagram of the set-up can be seen in figure 3.1 below.

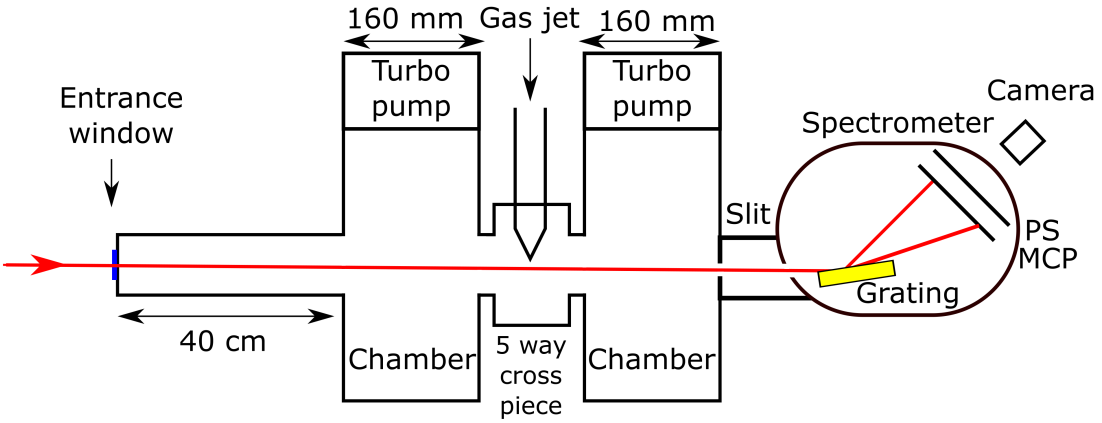

FIGURE 3.1: A figure showing the initial experimental set-up, composed of two vacuum chambers, a gas jet and the spectrometer, which has a grating, MCP and phosphor screen (PS) which is imaged using a camera

The turbo pumps are backed by roughing pumps, with there being an additional turbo that is not shown in figure 3.1, as it is on the spectrometer and is small in size compared to the other two which are used within the experiment. The small turbo is used to ensure that the pressure within the spectrometer is always in the 10^{-5} mbar region to prevent arcing across the MCP and phosphor screen.

The laser initially enters the set-up via a window which is placed on a 40 cm tube so that the intensity of the laser does not burn the entrance window as this could lead to several problems. If the entrance window has the beam tightly focused upon it, it will cause a burn mark and therefore leave a hole in the transmitted laser beam. If the burn is severe it could lead to the window weakening and then breaking. As a result a rush of air would enter the set-up and this would lead to arcing across the MCP and phosphor screen. Once the light has entered via the window it propagates down the system towards the gas jet which is positioned at the laser focus. The interaction region is located within a five way crosspiece with the fifth section of this being used as an observation window at the interaction region. This allows the plasma produced during

high harmonic generation to be observed and therefore phase matching is much simpler because the position of the plasma relative to the jet can be optimised by eye. On either side of the five way cross piece there are two vacuum chambers each with a turbo pump attached (these are mainly there for pumping purposes) and the light then propagates towards the spectrometer. Once the light has propagated down the experiment to the spectrometer it enters through the slit and then reaches the grating where it is diffracted onto the MCP and phosphor screen.

In the initial design of the set-up, the gas jet consists of a tapered glass capillary providing a continuous gas flow to the experiment. The gas jet is mounted on some stainless steel tubing and held in place via a compression fitting, it is fixed in position in the X plane relative to the laser beam (left/right). The height can be manually adjusted by releasing the compression fitting and sliding the stainless steel tubing by hand, resulting in limited movement and no repeatability in this action. This limits the accuracy with which the high harmonic generation process can be optimised and therefore leads to the reduction in overall flux compared to when all these parameters can be finely tuned. In order to finely tune the generation process with the set-up in this configuration, the final mirror before the focusing lens has to be adjusted to optimise the laser position relative to the gas jet. However, this leads to poor alignment into the spectrometer. Whilst the high harmonic generation process is being optimised the gain in flux and therefore expected gain in overall signal from doing so is not as sufficient as expected due to the misalignment into the slit of the spectrometer. This issue can be simply resolved by mounting the gas jet so that it can be precisely moved, this change is described later within this section. The experiment has a large volume so pumping down from atmospheric conditions takes a considerable amount of time. The base pressure of the system was 1×10^{-5} mbar, with a working pressure of 1×10^{-3} mbar, with 100 mbar of backing pressure behind the gas jet. Furthermore, when there is gas being used within the experiment to generate harmonics the pumps have to work hard, causing them to heat up to beyond there optimal working conditions. Overall, whilst the initial configuration can be used to generate harmonics and gather spectra it is very difficult to optimise the high harmonic generation process and the excess volume leads to pumping issues. This set-up was used to perform initial experiments in order to gain an understanding

and appreciation for the high harmonic generation process and the experimental factors that are important. After performing initial experiments it was realised that XY manipulation of the gas jet is required and the reduction of the experiments volume will greatly reduce the loads on the pumps and therefore allow more gas to be used within the experiment.

The changes that were made to the system following these realisations can be seen in figure 3.2.

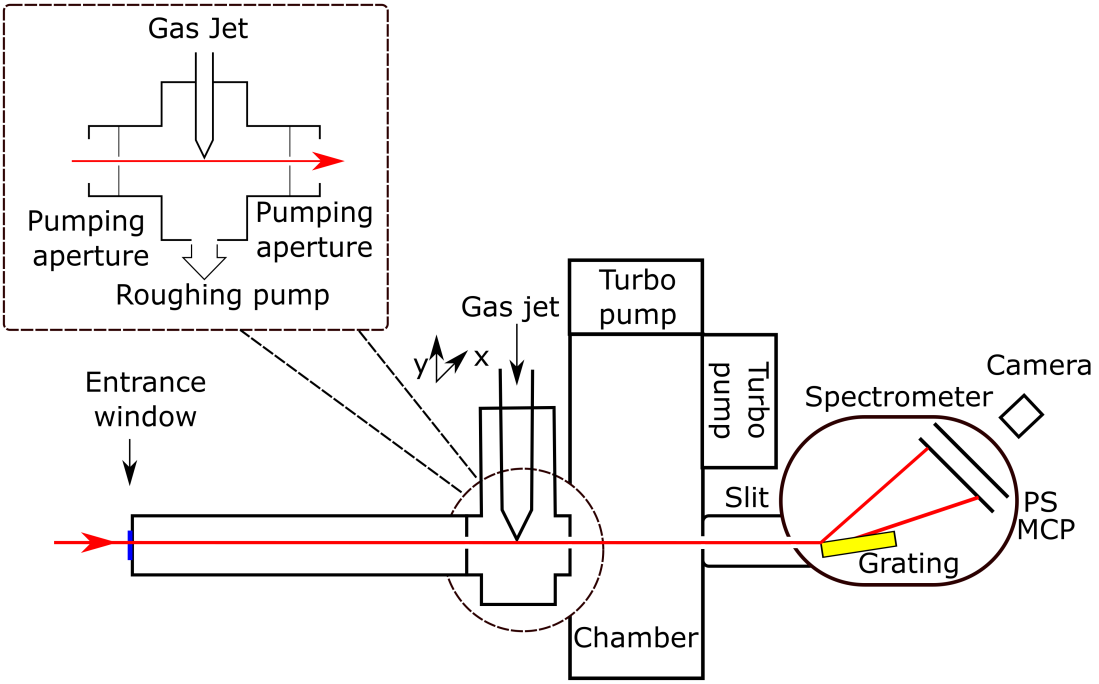

FIGURE 3.2: A figure showing the new experimental configuration, with the removal of one of the vacuum chambers and the addition of x, y manipulation on the gas jet, z is controlled using the focusing lens this is mounted on a stage. The insert in the figure shows the pumping apertures that have been added to the experiment around the gas jet.

The volume of this configuration is considerably smaller when compared to the initial configuration as seen in figure3.1. This is achieved by the removal of one of the vacuum chambers, whilst maintaining the same level of pumping because both turbo pumps are now attached to the same cylindrical chamber. This keeps the overall pressure in the system as low as before, with the gas going into the experiment under the same

conditions. This leads to comparable spectra with much less load on the pumps and a higher pumping efficiency.

The 5 way cross piece within which the gas jet mounted had some plastic inserts made to act as pumping apertures. These are 8 mm in diameter to allow the beam to easily make its way through and help considerably when using higher gas pressures. The addition of a roughing pump opposite the gas jet has been made, which has greatly increased pumping efficiency under load. This will prove critical when helium is used within the experiment due to its low pumping efficiency. The two plastic discs do not effect the movement of the gas jet nor the viewing of the interaction region through the window, whereas other options such as a metal sleeve would effect the observation of the interaction region. The increased pumping efficiency has resulted in a base pressure of 1×10^{-6} mbar and a working pressure of 1×10^{-4} at 100 mbar backing pressure behind the gas jet, enabling high pressure behind the gas jet to be used. The increased pumping efficiency has also enabled experiments to be carried out to test pumping efficiency and different sized gas jet apertures and asses how this effects the overall harmonic flux. Water cooling was added to both large turbo pumps in order to reduce the running temperature of the pump. Therefore the pumps can be left on with no over heating concerns. The addition of the XY manipulation means that all three degrees of freedom can be controlled, with the Z axis being controlled by having the focusing lens for the experiment on a manipulation stage. Care must be taken to make sure the lens remains perpendicular to the beam when moving the stage to adjust the focusing position. If the lens is not mounted perpendicular to the beam it will lead to a shift in the pointing of the beam when the focal position is adjusted. With the addition of the XY gas jet manipulation the pumping apertures can be added to the experiment with ease because the beam no longer has to be moved to the tip of the gas jet in order to obtain optimise harmonic flux, eliminating the concern of clipping the beam on the apertures.

3.3 Gas Delivery

In order to further develop the experiment we wanted to perform spectroscopic measurements on molecules that did not occur in the gas phase at atmospheric temperatures and pressures. In order to do this a new gas delivery system has been designed and built. With molecules or atoms that are in the gas phase at atmospheric conditions this is simple. For inert gases plastic tubing can be used as the carrier without any concern. For molecules that are not inert using plastic tubing would be hazardous, as it would lead to the breakdown of the plastic and potential release of the molecule into the atmosphere of the laboratory. Stainless steel tubing will be used throughout the design of the new system for anything other than inert gases. The system design can be seen in figure 3.3.

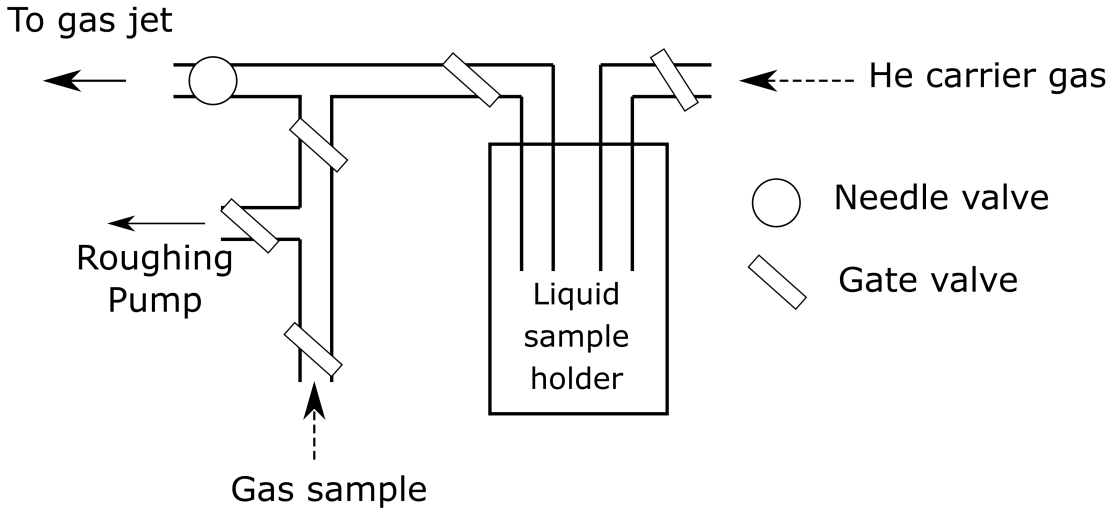

FIGURE 3.3: A diagram of the gas delivery system used for the experiment, showing that both liquid and gas samples can be used. When using a liquid sample it is possible to have He as a carried gas flow over the liquid sample.

In figure 3.3 everything other than the line for inert gases (argon/nitrogen) is made from stainless steel. There is a liquid sample holder as well as the option to have an inert gas connected at the same time. The liquid sample holder can be exchanged for more stainless steel tubing to allow the attachment of a non-inert gas cylinder such as carbon disulphide. The liquid sample holder will be used to get low vapour pressure liquids

into the gas phase with ease due to the reduction of pressure in the holder. This can be achieved via the tube that is connected to the roughing pump and therefore allows the sample holder to be pumped on. In order to get a liquid into the gas phase there are several options. One option is to rely upon the molecule having a sufficiently high vapour pressure under the vacuum conditions at room temperature so that a sufficient amount is in the gas phase to produce the minimum backing pressure (behind the jet) required. From many tests using inert gases (argon/nitrogen) this pressure is approximately 50 mbar for our set-up. If this is not possible, or slightly more gas pressure is needed to achieve a good high harmonic flux, we have the option to flow a carrier gas over the liquid sample holder, increasing the pressure due to the addition of the carrier gas but also providing an increased density of the desired molecule. Helium was the chosen carrier gas for this experiment due to its high ionisation potential. Because of helium high ionisation potential we are unable to generate harmonics solely from helium with the laser intensities used within our experiments, and therefore the carrier gas will not contribute to any spectra obtained. The low ionisation potentials of the molecules that we wish to study means that it is necessary to use low laser intensities, relative to those required to generate harmonics from helium, to avoid generating harmonics from the ion of the molecule we wish to study. The third option is to heat the container but this would also require all of the tubing to the end of the gas jet to also be heated and practically this is challenging. This was not required in any of the experiments performed to date.

The gas jet is a critical component of the experiment, which can dramatically effect the quality of the results obtained. The gas flows through the jet and into the interaction region where the atoms or molecules interact with the electric field of the laser and undergo the high harmonic generation process. The gas jet is of a simple design. The glass-blowers take a small piece of quarter inch glass tubing and pull this to produce as fine a tip as possible. The aperture of these are then measured using a Dynolite camera, this is done by measuring the pixels across the aperture and then comparing this to the pixels that are required for 1 mm in length, leading to a calibration. This is done by holding the gas jet next to a ruler. An image of this can be seen in figure 3.4 below:

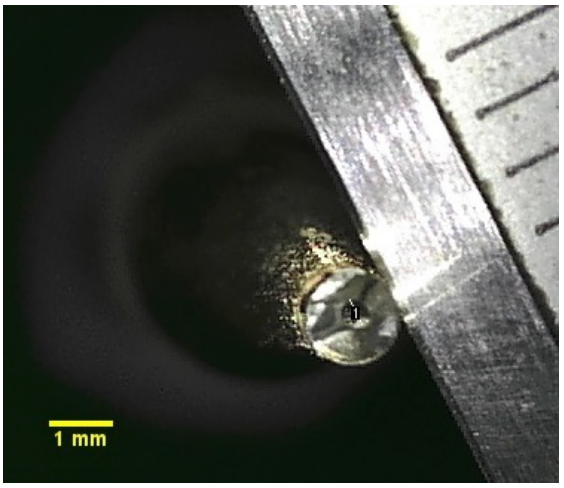

FIGURE 3.4: An image of measuring the aperture of the gas jet, the aperture of this jet is 400 μm.

The gas jet is connected to the stainless steel gas delivery system using a piece of small flexible plastic tubing to go around the outside of the metal tubing. This allows the gas jet to be placed inside the plastic tubing which is sealed using Torr seal in order to create a fully sealed connection between glass and metal. Gas jets are replaced once the tip of the jet gets burnt from being too close to the focal position of the laser. When the tip of the jet gets burnt by the laser it leads to two possible scenarios. Firstly the end of the jet can be sealed over by the melting of the glass and therefore no gas can flow from the jet. Alternatively, the end of the jet is burned and the hole is enlarged which leads to a reduction of gas density at the tip and a loss of signal. The life span of the gas jet is dependent on the experiment being carried out and varies between a few days to several months. When using low vapour pressure molecules, burning of the jet is much more likely due to the focal position of the laser having to be closer to the tip to be in the region of the highest gas density and therefore obtaining the best harmonic flux.

The size of the aperture at the end of the gas jet controls the size of the interaction region. As the gas comes out the end of the jet there are different regions of gas density, the very tip of the jet is a small intense region of gas. After this there is a region of silence continuing further from the jet until reaching the Mach disk.[68,69]

Unless the beam is on the tip of the jet the most intense region is the first Mach disk. The location of the Mach disk is dependent upon; the diameter of the nozzle (d), backing pressure of the jet (P_{jet}) and the background pressure of the chamber (P_{pg}). The relationship for the location of the Mach Disk is given by equation 3.1:

$$X_M = 0.67 \times d \times \sqrt{\frac{P_{jet}}{P_{bg}}} \tag{3.1}$$

X_M is the distance of the Mach disk from the tip of the jet. The Mach disk is the ideal position to carry out experiments in. It has the highest density of gas without being right at the tip of the jet which could lead to burning the jet as previously discussed. Whilst the Mach disk is ideal for carrying out experiments with high gas density for those with a low gas density it is experimentally simpler to perform the experiments at the tip of the jet. For example with argon, finding the Mach disk is simple as there is an intense region of harmonics and as you go further from the tip of the jet this decreases until the point at which you are in the Mach disk. However, with CCl_4 finding the Mach disk is extremely difficult due to the low backing pressure that is available and therefore the best harmonic flux can be found at the tip of the jet. Exceptional care must be taken when performing experiments at the tip of the gas jet to avoid burning the gas jet. To prevent this the height is carefully adjusted (in the Y dimension) to lower the jet to the beam on low laser power. Therefore if the beam does hit the tip of the jet there is not enough intensity to burn it. Secondly the optical path is boxed to avoid any instabilities that could be induced from air currents in the room. Finally the gas delivery system has been reinforced to avoid any vibrations of the metal sheet that it is mounted upon from being accidentally knocked, moving to much whilst adjusting the gas pressure or from the vibrations caused by the roughing pumps.

A 200 μm gas jet is optimal because it gives good photon flux and remains simple to obtain a good signal. A smaller jet 100 μm was tested but achieving high photon flux from this jet took much longer due to the higher level of alignment required because of the reduced size of the interaction region.

Furthermore, creating a $100\mu m$ jet is extremely difficult due to how the glass is pulled and therefore I have only been able to test this once. A gas jet that is larger than $200\mu m$ leads to too much gas entering the experiment and therefore results in pumping issues. Due to the increased volume of gas at the interaction region, this greatly increases the load on the turbo pumps and the roughing pump opposite the jet leading to concerns of causing damage to the pumps. Additionally it leads to a reduction in photon flux due to the disruption caused at the tip of the gas jet by the additional atoms present because the produced harmonics are absorbed by the addition molecules or atoms. In a general case the harmonic intensity increases as gas pressure increases. The harmonic yield for the majority of harmonics within a spectrum scales quadratically with pressure.

3.4 Spectrometer

The spectrometer that has been used to perform the majority of the measurements presented in this thesis is a Rowland spectrometer. This employs a concave diffraction grating in order to spread the harmonics which are then diffracted onto a curved Micro Channel Plate (MCP) and phosphor screen set-up which is then imaged using a camera. The spectrometer was designed and built by in Troitsk University Russia in 2006, the company has since dissolved and there is a considerable lack of information about them in the instruction manual. A figure showing the optical layout of the spectrometer can be seen in figure 3.5.

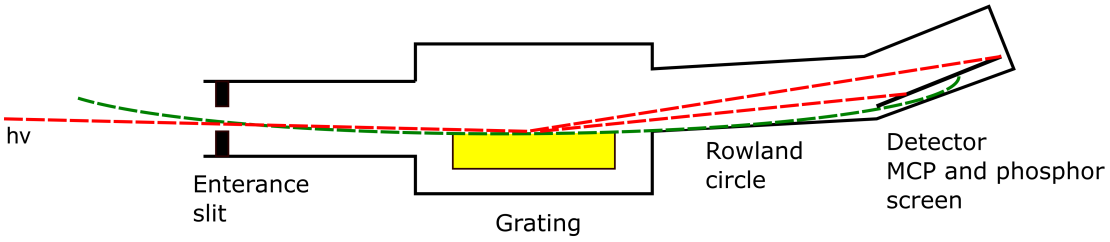

FIGURE 3.5: A schematic of the Rowland type spectrometer, showing the Rowland circle with the green line, alongside all key components with the spectrometer.

The produced XUV and fundamental wavelength enter into the spectrometer though the entrance slit. The slit width is important as it not only provides a differential pumping aperture but it is also used to control the spatial resolution of the individual harmonics. The larger the slit the broader the harmonics appear when imaged. When measuring a spectrum of a substance such as argon, where lots of different energy harmonics are produced, this effects the appearance of the spacing of the harmonics. If the slit is too wide it effects the spectral resolution and can lead to the spectrum appearing as a broad smudge which is almost continuum like. The harmonics should appear as a typical spectrum as seen in chapter 1.2.3.3. The smaller the slit the greater the spectral resolution of the spectrometer, however there is a compromise here between photon flux and resolution. Through the experiments that have been carried out we have found the optimal slit width to be approximately 100 μm because this leads to sufficient harmonic flux such that exposure times are not excessively long and each harmonic is clearly separated.

The light then arrives at the diffraction grating, where the different wavelengths of light are separated out onto the MCP. Figure 3.6 shows a schematic representation of the MCP and phosphor screen set-up, with a zoomed in section of the MCP. The single MCP is used to amplify the signal onto the phosphor screen which is then imaged using a camera. MCPs are made up of several small channels that a high voltage can be applied to, leading to the amplification of the signal that hits the plate. The level of amplification is dependent upon the voltage that is applied to the MCP. When light hits the MCP, it generates a cascade of electrons through the channels. The cascaded electrons hit the phosphor screen causing this to glow. The phosphor screen is then imaged with a camera to obtain the high harmonic spectrum.[70] Over the course of this work two cameras have been used due to technical problems with the first. Initially, the camera being used was a Princeton Instruments Pixis 400 in conjunction with a Nikon camera lens. The Pixis has a charged-coupled device (CCD) chip this offers much higher resolution than a standard complementary metal-oxide-semiconductor (CMOS) chip. A CCD chip however, has longer read out times and is much more costly. This camera was replaced with an AVT-Manta-G-235, which is a fraction of the cost of a new Pixis

camera as it has a CMOS chip architecture, and doesn't have any cooling, however is still of suitable quality for the experiments.

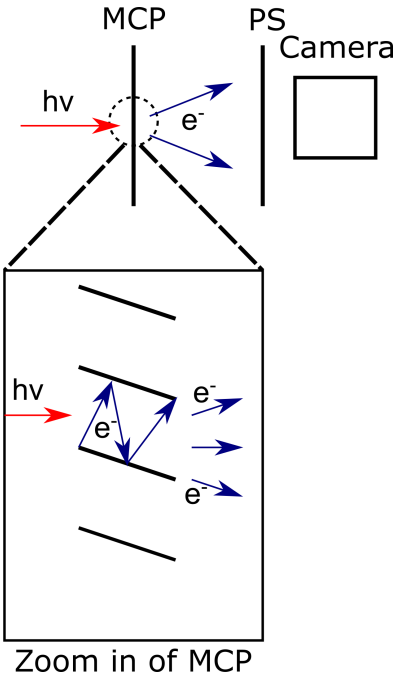

FIGURE 3.6: A schematic showing the MCP and phosphor screen (PS) configuration that is imaged by the camera in order to record a high harmonic spectrum

There are several limitations with the spectrometer, not being able to contact the original manufacture to get details about specifics that are not listed within the manual. The MCP in the spectrometer is curved, the radius of curvature is unknown these are also no longer standard. Easily obtainable commercial MCPs are generally flat meaning that it is hard to replace the curved MCP. The wiring to the detector is another issue with this spectrometer, the connection to the phosphor screen is poor. It relies upon a flat connector being pressed onto it to make a good connection and this is not something that can be soldered for fear or damaging the phosphor. This spectrometer also has a limited wavelength range over which it can operate. At 800 nm the lowest energy harmonic detectable is the 13th which is 61 nm or 20.32 eV. Molecules with a low ionisation potential also have low cut off energies which can be calculated using equation 1.10, and therefore the observable harmonics from these molecules will be limited. To be able to carry out a high harmonic spectroscopy experiment a minimum of five harmonics are needed as seen in previous studies. This is to give enough information from the

molecule, as a bond length change in time will be seen as a change in individual harmonic intensity with time. Using the current spectrometer with its range of 72 nm to 32 nm these observations are not possible so I have designed a new spectrometer. In theory higher energies are easily recorded with the Rowland spectrometer as the grating is interchangeable allowing observations of these higher energies to be made. However, due to the low ionisation potential and the 800 nm driving wavelength we have available to us we cannot reach these high energies with molecules. No grating for lower energies is available therefore making these observations is not possible. In order to achieve this a new spectrometer has been designed and will be discussed in 3.4.2.

3.4.1 Calibration of a High Harmonic Spectrum

Each time the experiment is re-aligned the harmonic spectra that have been obtained need to be calibrated to ensure the energy range that is being observed. This is done so that the raw image in pixels can be converted to intensity (arb. units) and wavelength (nm). Wavelength and energy can be easily converted between using $E = hc/\lambda$ so that a figure of intensity vs energy in eV can be produced. The wavelength used throughout all the experiments performed is 800 nm, only odd harmonics are generated during these experiments. To calculate the wavelength of the harmonics generated from 800 nm the following equation 3.2 can be used:

$$\lambda_q = \frac{\lambda_0}{q} \tag{3.2}$$

In equation 3.2 λ_0 is the fundamental wavelength, q is the harmonic number and λ_q is the wavelength of the generated harmonic. Only the odd number harmonics wavelengths are then taken forward into the next step of the calibration.

The raw image collected is then processed to provide an un-calibrated spectrum via summing across the central region of the harmonics that have been recorded. The un-calibrated spectrum is then compared to the predicted position of the harmonics, the two relate by a simple $y = mx + c$ line. The method takes the difference between two harmonics that have been recorded in pixels, and then compares this to the difference

in nm, reuslting in m, with an offset c being using as the start point is unknown. The calibration will provide the solution to the number of pixels per nm, resulting in a calibrated spectrum which can be seen in figure 3.7. The calibration is checked by marking on the expected position of the harmonics, conforming that that the calibration is accurate.

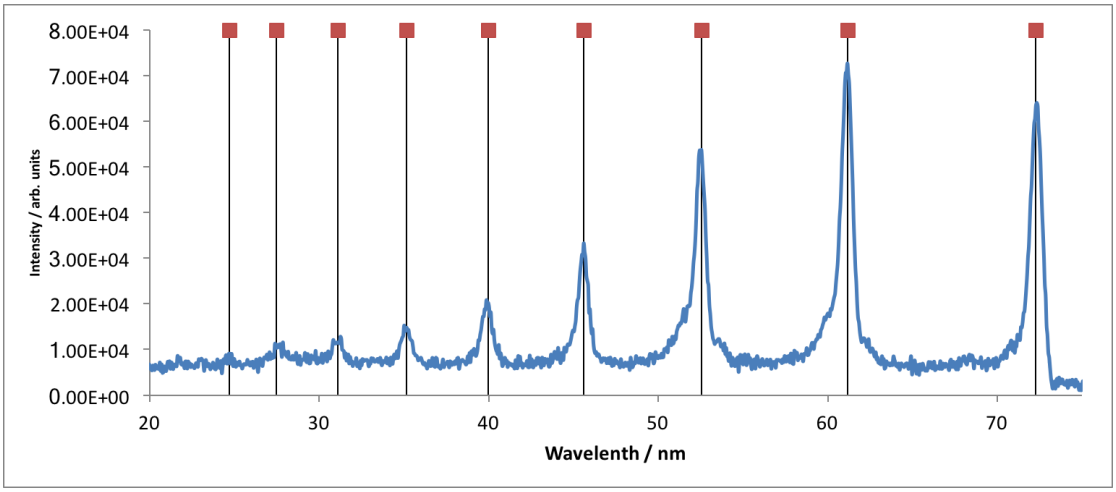

FIGURE 3.7: A calibrated high harmonic generation spectrum of N_2. Showing the predicted position for each harmonic agrees with the calibrated spectrum as the lines for the predicted peaks match the peaks in the spectrum that has been obtained.

3.4.1.1 Autocorrelation experiment

A way to simply test the set-up and the optical path being used is to perform an electric field autocorrelation experiment, using the high harmonics. The experiment was performed to ensure that there were no pre-and post pulses in the experiment and in order to check the electric field autocorrelation time. This experiment was carried out in argon, the two arms of the auto-correlator were set-up as if performing a high harmonic spectroscopy experiment with a 1 W arm used and a 200 mW arm. This was done to ensure the clearest electric field autocorrelation was obtained with any extra peaks present being resolved. The experiment has had some issues with bad optical coatings especially on the half wave plate which was used to control the relative polarisation between the two arms of the experiment. The electric field autocorrelation experiment was performed with both arms parallel to each other in terms of polarisation. We found

that using a wave plate with a bad optical coating led to a post pulse 200 fs after the main pulse, with about 10% of the intensity of the main pulse. Whilst this may appear trivial the next experiment we had planned was one which measured molecular vibrations, this 10% post pulse is enough to set up a new vibrational wave packet leading to some very confusing results.

Additionally, we had concerns about the mirrors that are being used in the experiment. All the mirrors used throughout the experiment were dielectrics. To ensure that the mirrors were mounted the correct way round so that the coated surface was being used for the reflection, we built a single shot auto-correlator to check each optic individually. The single shot auto-correlator was of a simple design employing the optics used throughout the experiment, but instead of recombining both beams co-linearly in the 50-50 beam splitter the beams were crossed and then passed into a piece of BBO. The optical path that was used for this can be seen in figure 2.4, with the replacement of a BBO for the beam splitter. The delay stage was then scanned to look for pre-and post pulses within the experiment. Each optic was then systematically checked to confirm if there was any issue with that particular optic. The single-shot auto-correlator was examined by eye, with the central point showing that the two pulses are overlapped in time and space. Once this test had been performed an electric field autocorrelation was once again performed leading to the result as seen in figure 3.8.

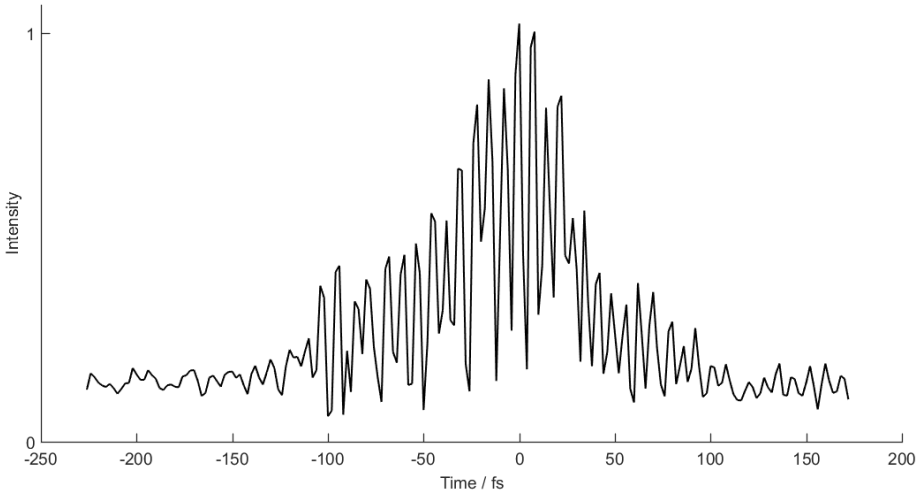

FIGURE 3.8: An autocorrelation scan performed using harmonic generation, the time resolved trace is from an isolated harmonic, and shows that there are no pre or post pulses remaining in the experiment.

The figure 3.8 shows that after checking each optic, there is on longer a pre or post pulse in the experiment and that the beam path is ready to be used to perform high harmonic spectroscopy experiments the results of which are presented in chapter 4.

3.4.2 Flat Field Spectrometer

In order to detect lower energy harmonics produced from molecules with low ionisation potentials whilst using an 800 nm driving field, a new spectrometer had to be designed and commissioned. The low cut-off of these low ionisation potential molecules means that they are out of the detection range for more than one or two harmonics of the Rowland type spectrometer. The new spectrometer was designed such that even low flux signals can be easily ascertained. The new spectrometer is of the flat field design as this enables a wider range of wavelengths to be accessible with a single grating. The grating angle can be changed and the angle at which the detector is placed relative to the fundamental beam can be altered, leading to a greater range of accessible wavelengths in the detector. The spectrometer must be capable of collecting even the smallest amount of

XUV, enabling the detection of the smallest signal change allows for improved studying of molecular dynamics.

Initially, the flat field spectrometer was designed with a few specific molecules in mind, NO_2 NH_3 and HNCO, all with an ionisation potential of approximately 10 eV. The cut-off for these molecules was calculated by simply using the cut-off equation 1.10. This was then combined with the ADK code in order to ensure the harmonic cut off was reach via the ground state only. The range for this spectrometer is based around the cut-off for these molecules which is approximately 30 nm, or 40 eV, and we want to capture the maximum number of harmonics possible so the desired range is from 80 nm, or 15 eV, to cut off. Using the 800 nm driving field in Southampton this gives a harmonic range of 9-20 that will be covered by this spectrometer.

In order to obtain the angle at which the various wavelengths of generated XUV are diffracted from the grating, the grating specifications are required. A range of these were easily obtained from manufacturers. In order to calculate the angle at which generated XUV is diffracted we used a script written by David Neely from the Central Laser Facility.

The code was used with his permission. In principle it takes the wavelength range desired and this light is then diffracted off the grating using the predetermined specifications. The grating specifications are inputted from the details obtained from the manufacturers prior to running the calculation. The grating we chose to use for the flat field was a 1200 line grating, this is the same grating that is used in the flat field at Artemis, and suitable for diffracting the wavelength range we wish to cover whilst remaining within budget. Increasing the number of lines on the grating and the blaze angle of these lines increases the cost dramatically. The output is then the focal position for the various wavelengths of the different grating angles that were under investigation as seen in figure 3.9. The code then enables you to place a detector across the wavelength range at a particular grating angle in order to grasp how best cover the whole range that is desired. Getting the detector into the correct position initially proved difficult because the focal plane of harmonics being projected needs to be flat to ensure good spatial resolution.

If the harmonics are curved the MCP would also need to be curved, if avoidable this is desirable in terms of simplicity, cost and availability.

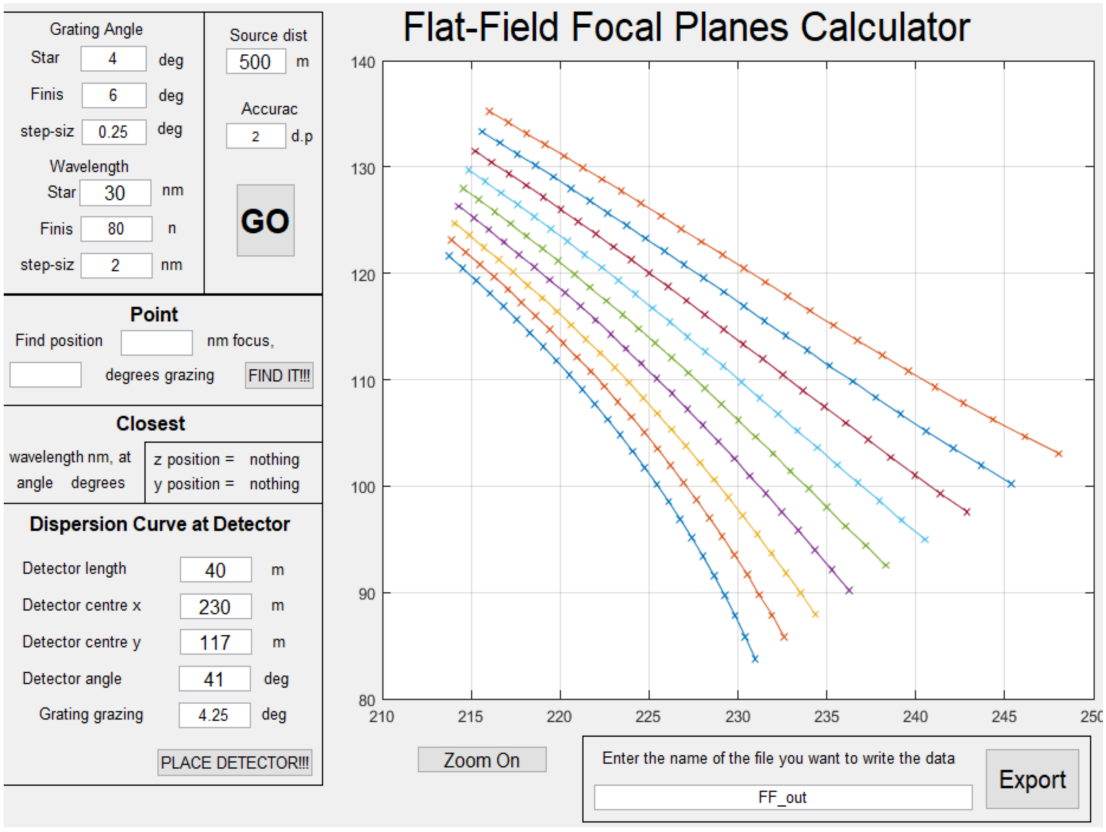

FIGURE 3.9: An output from the flat field design code showing the different focal planes at different grating angles. The wavelength range is set on the left hand side from 30 nm to 80 nm. With the grating angle ranging from 4 to 6 degrees, showing the different projections at a particular wavelength for each grating angle.

From the output of the code as shown in figure 3.9 it is possible to place the detector and work out if the position will result in the harmonics being projected onto it without any dispersion. Once the detector has been placed this enables its position to be checked and ensures that the desired range will be covered in the length of the detector. The position that the detector will be placed in can be seen in 3.10.

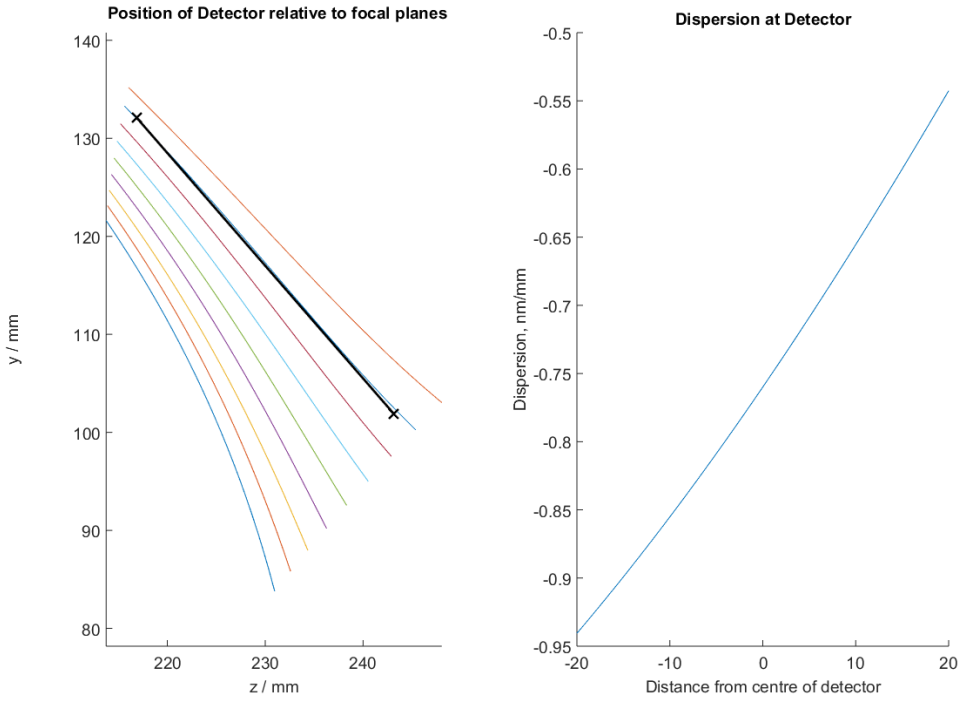

FIGURE 3.10: A second output from the flat field code, (Left) optimum detector positions calculated for various grating angles between 4-6 degrees in steps of 0.25 degrees covering the wavelength range defined in figure 3.9. (Right) wavelength dispersion at the detector for the detector position marked with a cross in (Left)

With regards to detection it was decided a chevron stack MCP phosphor screen stack was the optimal choice because they have good signal amplification. The wavelength that we want to cover diffracts and fits well onto a 40 mm MCP. The other option for detecting XUV is a CCD camera. These have a slightly faster read out time and less distortion of the signal as they don't have the same amplification processes as the MCP, however the chip of the camera can easily be damaged if any of the fundamental 800 nm beam strays onto it. They also have to be held under vacuum and relative to the MCP phosphor screen stack are very expensive. The reason for choosing dual MCP's is to ensure that even the smallest signal change can be easily observed thanks to the additional amplification of the second MCP.

A vacuum chamber is required for the flat field design, and this needed to be of specific dimensions and size in order to have the required equipment in the correct positions to

obtain a spectrum. The chamber needed to house the grating, a goniometer to move the grating angle and a beam block to prevent excess scatter from the fundamental onto the MCP. The chamber itself would also need to have several flanges on it in order to get light into it, check the vacuum pressure, control goniometer and view the grating. It would also require a breadboard inside in order to mount the goniometer and grating assembly and a flange in order to facilitate the attachment of a turbo pump. Once again due to the high voltages that are required when operating the MCP and phosphor screen the vacuum chamber must be able to reach the low 5×10^{-5} mbar. In order to reach this vacuum pressure a 300 L/s magnetic turbo from Leybold will be used, this is much larger than the turbo that is on the current spectrometer. However, the overall volume of the new spectrometer will be greater.

The chamber was designed with the aim of simplicity, and therefore maintaining its ease of use. Whilst allowing for flexibility in the positioning of the large component of the turbo pump due to limited space within the laboratory. The design for the chamber can be seen below in figure 3.11:

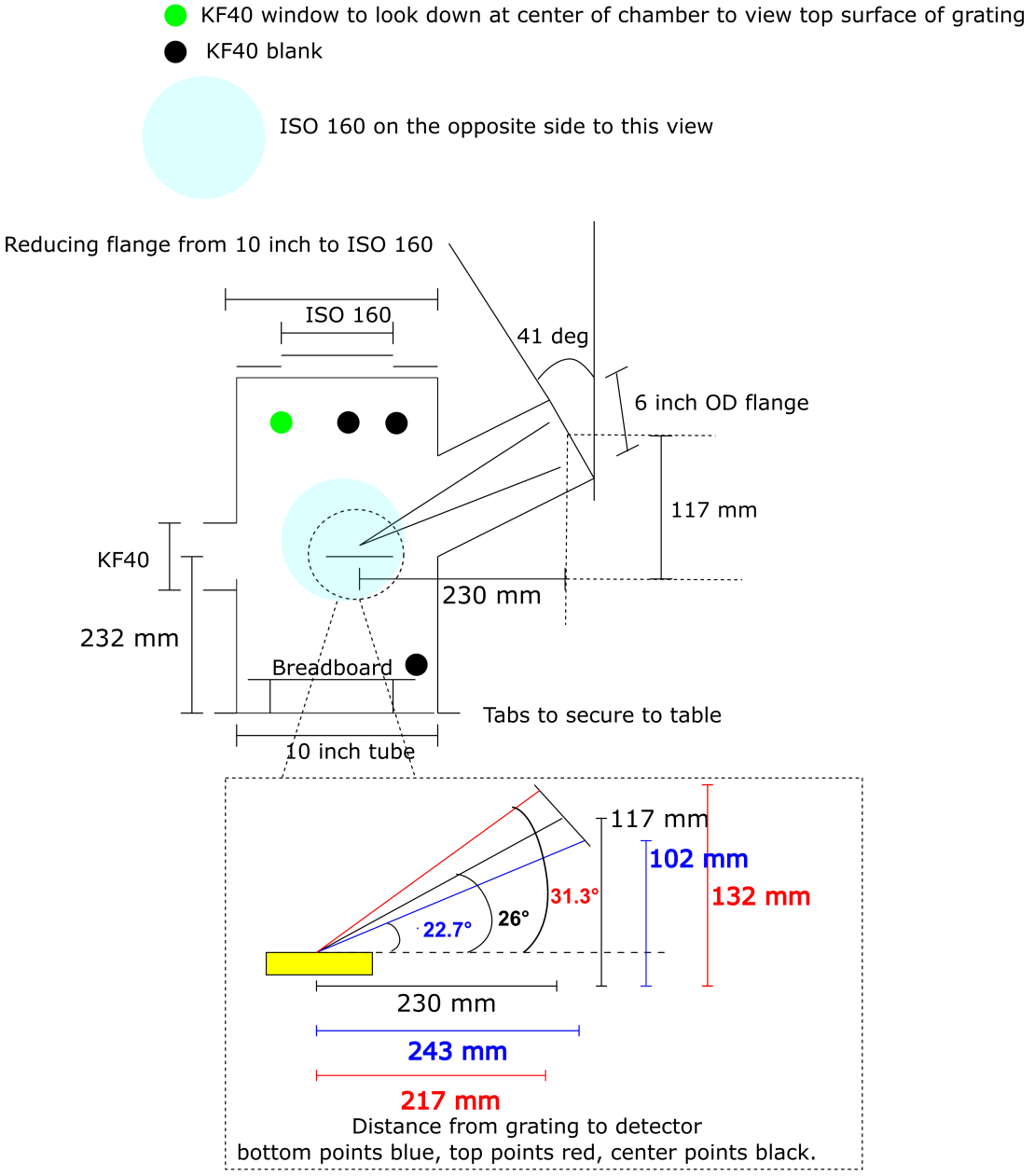

FIGURE 3.11: A diagram of the design of the flat field spectrometer, showing key flanges marked onto the design alongside the angles and measurements from the centre of the grating to the edges of the detector which is 40 mm in length. The angles and measurements are extracted from the output of the design code as seen in figure 3.9

Upon the spectrometer's arrival it was assembled and commissioned. The new spectrometer worked considerably better than the old spectrometer. Before the grating an

iris was placed and this was mostly closed in order to act as a pin hole, this is equivalent to the slit in the Rowland spectrometer, to provide good spatial resolution for the harmonics. Following the grating a beam block was placed to stop as much of the residual fundamental beam as possible going up onto the MCP, so the signal will be as clear as possible. It clearly picked up signals and had a much high resolution. For comparison over the new spectrometers energy range and to show it has considerably better resolution compared to the old spectrometer there is a comparison spectrum between CCl_4 (IP = 11.47 eV) in both old (solid line) and new spectrometer (dashed line) in figure 3.12. It is clear there is stark contrast between the two. The exposure time required to ascertain the image from the old spectrometer 1.5 seconds compared to the new spectrometer where the image only took 0.5 seconds to acquire.

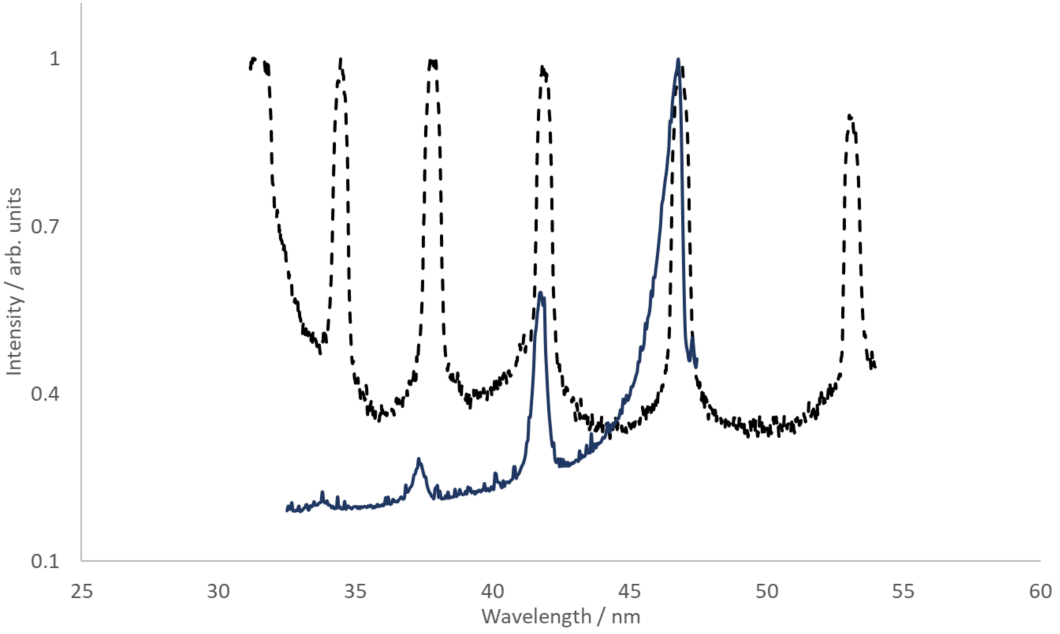

FIGURE 3.12: A figure comparing the difference between the new flat field spectrometer and the Rowland type spectrometer. This data has been normalised, the dashed line is the spectrum recorded on the flat field spectrometer whilst the solid line is the spectrum recorded on the Rowland spectrometer

The improvement shown in figure 3.12 is dramatic, firstly the flat field includes an additional low energy harmonic. Secondly, the number of harmonics recorded is vastly

different, the old spectrometer there are three harmonics present on the new spectrometer there are six clear harmonics. Thirdly the exposure time in order to collect these images is a third of the time using the new flat field spectrometer. The wavelength range that has been recorded on the flat field is not the range over which we aimed for originally however this can be tuned by adjusting the grating angle, which requires the grating to be movable on a goniometer. The grating is currently mounted on a goniometer but unfortunately the feed through in order to move this component had a very large lead time, so the full range over which the spectrometer can work has not been thoroughly assessed. But, in figure 3.12 it can be seen that the flat field offers large improvements compared to the Rowland spectrometer. The obtained spectrum also shows the successful design and commissioning of the new flat field spectrometer.

3.5 Summary

In this chapter I discussed the development of a high harmonic spectroscopy experiment in Southampton. An electric field autocorrelation experiment is presented here, which was done in order to prepare the experiment for a time resolved study of carbon tetrachloride this work is presented in chapter 4. A new flat field spectrometer has been designed built and commissioned showing a marked improvement on the Rowland type spectrometer. The flat field spectrometer has extended the experiments capabilities, it has greater sensitivity and a more suitable wavelength range for high harmonic spectroscopy experiments on molecules. The experiment now has the capability to perform high harmonic spectroscopy measurements, and the spectrometer can be used in order to develop the high harmonic generation source for future time resolved XUV probe photoelectron spectroscopy measurements.

Chapter 4

High Harmonic Spectroscopy of Carbon Tetrachloride

In this chapter I describe the experimental results obtained from the pump-probe high harmonic spectroscopy experiment of carbon tetrachloride. The experiment measures the vibrational motion and is a proof of principle demonstration of an experimental configuration that has been developed in Southampton.

4.1 Introduction

High harmonic generation has been used to study a number of different molecular systems investigating dissociation dynamics, vibrational dynamics, electronic structure and also to image molecular orbitals. Some notable systems that have been studied using high harmonic spectroscopy are, Br_2, NO_2, SF_6 and several small hydrocarbons.[56,58,59,71,72] The most relevant example to the work that is being presented in this chapter is the work that has investigated molecular vibrations. A system that has been studied several times is SF_6. Using this molecule, high harmonic generation has been shown to be sensitive to molecular vibrations. In these experiments Ferré et al. used an 800 nm non-resonant pump to Raman excite vibrational modes in the SF_6 molecule these were then probed by a time delayed pulse which generated high harmonics. SF_6 is a

competitively large molecular system with relatively slow molecular vibrations. SF_6 has been well studied using high harmonic generation, due to its high ionisation potential and large cross sectional area, making it optimal for high harmonic generation.[71,72]

Alongside SF_6, N_2O_4 has also been studied using high harmonic spectroscopy in order to probe molecular vibrations. In the study Wen at al resolved interactions between vibrationally excited and unexcited N_2O_4.[73] This dimer system is large, with a slow molecular vibration between the two nitrogens which provides a clear signal. High harmonic generation is sensitive to molecular vibrations in these molecular systems, however the study has not been extended into other molecular systems. As such the question of why high harmonic generation is sensitive to molecular vibrations remains experimentally unanswered. We have performed this experiment on an additional system with the aim of providing more conclusive evidence for this problem. Photoelectron spectroscopy has shown sensitivity to molecular vibrations, the vibrational motion modulates the photoelectron intensity through changes in the Franck-Condon factor. If high harmonic spectroscopy can successfully resolve vibrations then this is additional information could also be obtained when studying a photodissoication reaction using high harmonic spectroscopy.

As a first proof of principle experiment using the new experimental configuration and liquid sample holder we aimed to study the vibrational dynamics of carbon tetrachloride (CCl_4) following Raman excitation. The aim of the experiments carried out in this chapter was to test the sensitivity of high harmonic generation to molecular vibrations and to observe the effect of the Fermi resonance within CCl_4. CCl_4 has four Raman active bands and a Fermi resonance from the two F2 anti symmetric stretching bands seen at 790 and 762 cm^{-1} interacting with the combination band ($\nu 1 + \nu 4$) . The four Raman modes can be seen in Table 4.1 below:

Mode	Vibrational period (fs)	Wavenumber (cm^{-1})
A1 (sym str)	72	459
E (bend)	153	217
F2 (anti sym)	42	790
F2 (anti sym)	43	762
F2 (umbrella)	106	314

TABLE 4.1: A table showing the Raman active modes and oscillation frequencies for each mode,[74] a Raman spectrum of these modes can be seen in figure 4.1.

The Raman modes for CCl_4 are relatively slow oscillations due to the relatively heavy nature of the molecule, compared to much smaller and lighter molecules such as methane. This is ideal for high harmonic spectroscopy measurements using our laser system because our time resolution will be limited by the cross correlation between the pump and probe pulses. The figure 4.1 shows a Raman spectrum of CCl_4 showing the different vibrational modes and their relative intensities.

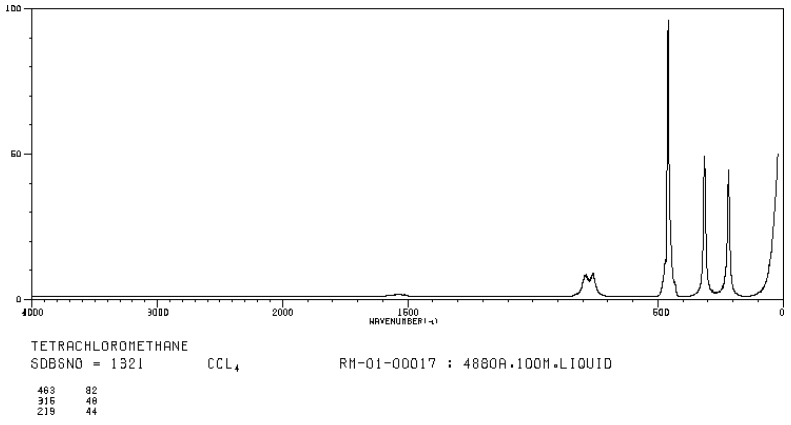

FIGURE 4.1: A Raman spectrum showing the different observable vibrational bands in CCl_4 [3]

4.2 Experimental

The time resolved pump probe experiments were carried out using two 800 nm beams, each of different intensity. An 800 nm, 100 mW pump beam was used in order to excite the vibrational wavepacket of CCl_4. The 800 nm probe beam, 1 W, was used to perform high harmonic generation. The ionisation potential of CCl_4 is 11.47 eV, from ADK calculations we can predict that 0.6 W of probe energy is sufficient to perform high harmonic generation whilst avoiding ionisation from the ion.[34,35] The output from the ADK calculations can be seen in figure 4.2 showing that no ionisation is only occurring from the ground state across a whole laser pulse.

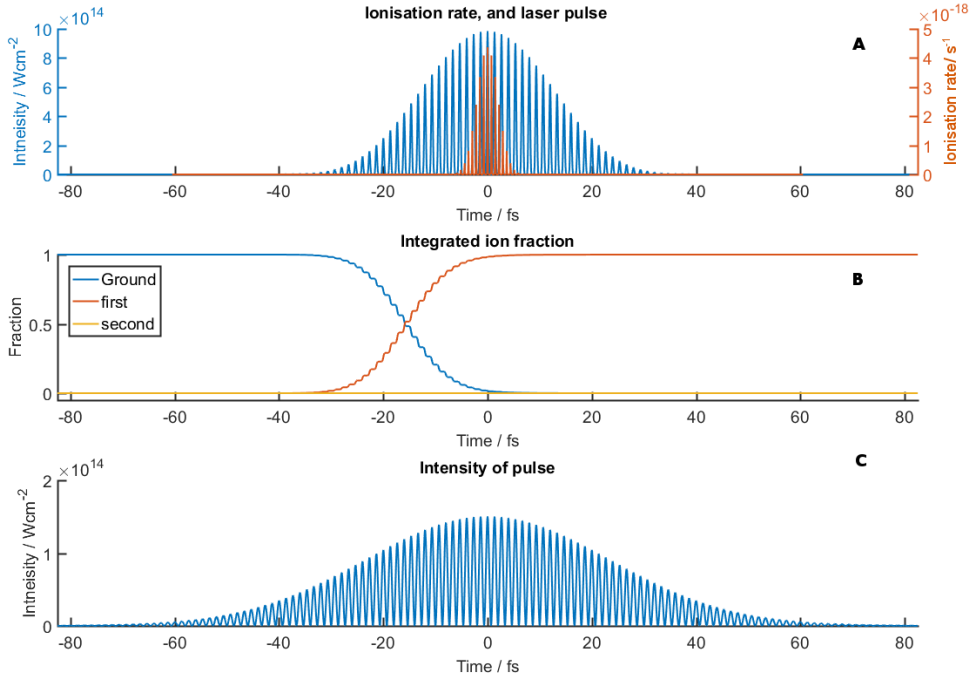

FIGURE 4.2: A figure of the output from the ADK code, showing the intensity required to perform high harmonic generation from CCl_4, whilst avoiding ionisation and high harmonic generation from the ion. A shows the ionisation rate from the ground state blue line and the first ionisation state orange line, B shows the state populations for the neutral ground state and the singly ionised molecule (first) and the doubly ionised molecule (second) and C shows the intensity across the laser pulse.

Figure 4.2 C shows the intensity across the laser pulse, A shows ionisation rate from the ground state, blue line, and from the first ionisation state orange line. B shows the state populations throughout the laser pulse. The figure shows that the ground state is being completely ionised just before the peak of the laser pulse. During the experiment we found that we needed to drive high harmonic generation slightly harder so that a spectrum could be observed so 1 W of laser power is used. The reason for needing to drive harder than predicted is that the ADK calculation is atomic, and the single MCP has limited signal amplification.

In order to control the time delay within the experiments the two beams are moved relative to one and other. The time delay is controlled via a delay stage as seen in figure 2.4. When the probe pulse comes first, this is negative time and there should be no dynamics occurring here as the pulse used to start the molecular dynamics is yet to arrive. Once the pump and probe pulse are overlapped we have to find time zero. Time zero can be found using the method described in chapter 2.2.3. Following this the pump pulse arrives first initiating the dynamics with the probe making observations of the dynamics started by the pump. The experiment was carried out from -200 fs in order to get a background signal to measure the noise level within the experimental set-up. The experiment was then scanned out to approximately 1000 fs in steps of 10 fs with a spectrum being collected at every time delay. The reason for scanning out to 1000 fs is to ensure that all of the oscillations from the molecule are collected and observed experimentally. The 10 fs time step was chosen because of the finite cross correlation between the two pulse, smaller step size would not have shown more information.

The experiments were performed using the equipment and process described in Chapter 3 and are only briefly described here. The laser is focused using a 70 cm focal length lens it then enters into the vacuum system via a window. The focal spot is at the interaction region of the gas jet. The intensity from the focused laser beam at the gas jet leads to the generation of high harmonics. The harmonics then propagate down the set-up into the Rowland type spectrometer where they are detected and recorded.

In order to get CCl_4 into the gas phase the liquid sample holder was used. CCl_4 has a low vapour pressure such that under vacuum there should be approximately 50 mbar

of gas pressure behind the jet. Whilst this backing pressure is low, from previous tests we know that it is sufficient for us to generate and obtain a harmonic spectrum. In order to increase the weak signal obtained from CCl_4 the slit into the spectrometer was widened slightly. High spectral resolution is not required because only three harmonics are being observed. This is due to the low ionisation potential of CCl_4 and therefore low cut off energy and because of the limited energy range of the spectrometer more harmonics cannot be detected.

In order to collect each data point the image that is gathered from the camera was collected for an exposure time of 1.5 seconds before moving to the next image. The camera used is free running therefore, to ensure that each image collected is a fresh image of the desired time point a wait time of two seconds was built into the program that controls the stage and the camera. This guaranteed no overlap between time steps in each time step recorded. Multiple collections will be made from -200 fs through to 1000 fs (one complete cycle) recording a spectrum at each time point. At the end of each scan the experiment is stopped and the signals re-optimised due to the low collection efficiency of spectrometer. Each cycle will be repeated 6 times so that an average of all the data points can be used offering improvements in signal to noise. We chose not to collect the data 6 times before moving on to the next point because throughout the experiment there is a loss of signal over a long time. The signal maintains a constant level for the time period required to perform one complete acquisition cycle. More information will be given on the cycles and how this has affected the analysis process later in this chapter. The spectrometer is calibrated using the method shown in chapter 3.4.1 using harmonic generation in argon.

4.3 Results and Discussion

A high harmonic spectrum of CCl_4 is shown in figure 4.3. This is obtained at -200 ps, the probe arrives before the pump so the spectrum is equivalent to the spectrum obtained by the probe only.

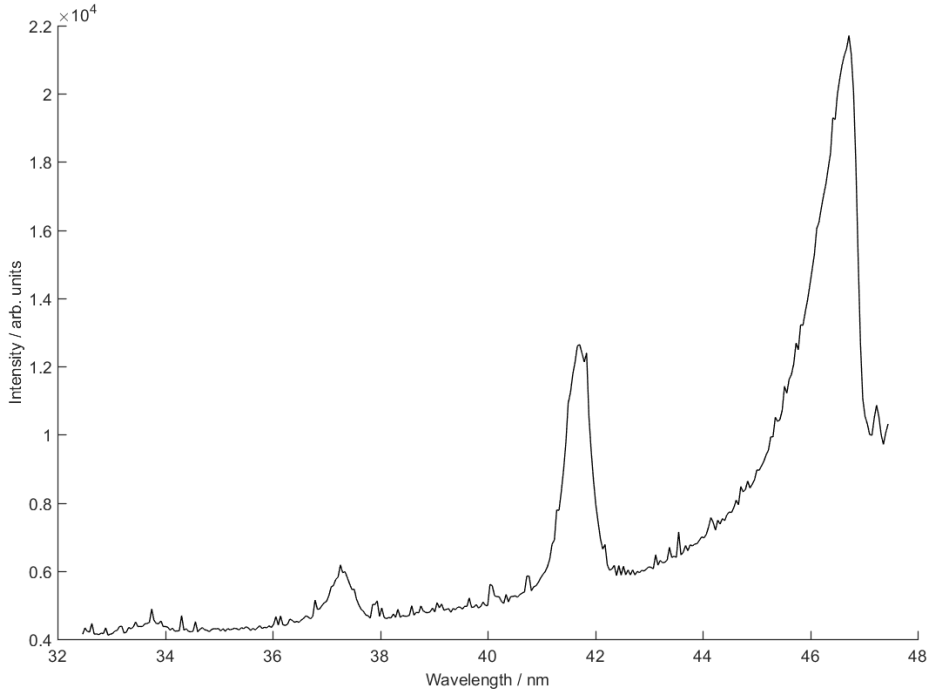

FIGURE 4.3: A harmonic spectrum of CCl_4, obtained at -200 fs, showing the 13th, 15th and 17th harmonic of the fundamental 800 nm beam with a laser power of 1 W.

In figure 4.3, two harmonics can clearly be seen, with a small third harmonic present. The harmonics are the 13th, 15th and 17th harmonics of the fundamental 800 nm probe beam. In order to process the data, a harmonic spectrum for each time point must be initially extracted from the image. Extracting a spectrum is carried out by integrating across the region in which the harmonics are present in the image. Once a spectrum has been obtained for every time point, each harmonic can be looked at in turn resulting in a a plot of the time dependent intensity for a particular harmonic order. Throughout this work harmonic 13 will be used as this harmonic has the most signal and is least affected by experimental drift which leads to a loss of signal. Once a time dependent spectrum has been obtained this can then be Fast Fourier Transformed to give a frequency spectrum.

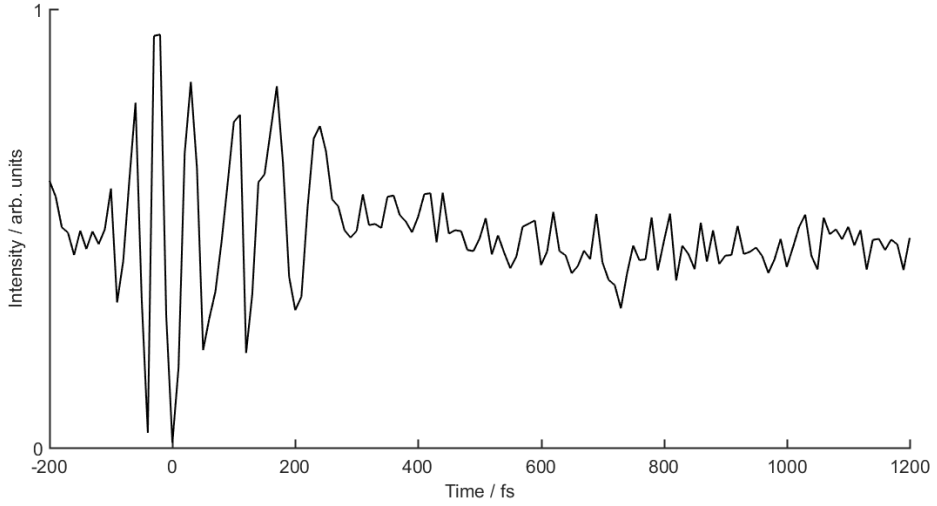

FIGURE 4.4: Time dependent intensity of the 13th harmonic of CCl_4, measured by a 1 W 800 nm probe following Raman excitation of the vibrational wavepacket.

Figure 4.4 shows the time dependent intensity of the 13th harmonic can be seen for a single experimental run. In figure 4.5 we plot the time dependent intensity of the 13th harmonic for every individual cycle. In this figure it is clear that there is a discrepancy in the time zero position within the spectrum because of the off set between the peaks in the different experimental runs. Whilst the stage was capable of making a precise step of 10 fs each time it moved, its ability to move back to the same starting position was not as precise. The data has been adjusted such that the peak of the time zero signal overlaps in every time dependent spectra that has been acquired. The error here in the stages accuracy was $\pm$ 8 fs. This can be seen in figure 4.5, showing the data before it was corrected for the stages accuracy limitations, it can be seen that whilst all the peaks do not overlap their shape is the same.

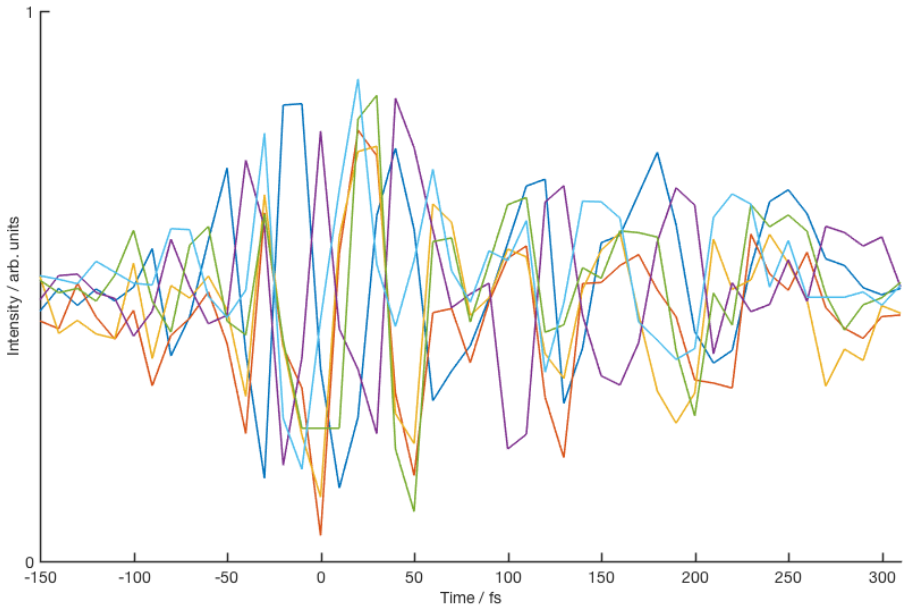

FIGURE 4.5: Time dependent harmonic intensity plots from each data run, showing the discrepancy in the time zero position between the runs.

The miss alignment in features shown in figure 4.5 can be corrected for by an average shift of the spectra by ±10 fs, this corrects for the accuracy of the stage. The corrected data is shown in figure 4.6. The shift made is minimal but it brings the centre of mass for each time zero peak to the same position. These corrections are within the limit of the stage and produce peaks which are all overlapped. From this we can sum all the time dependent spectra to produce a frequency spectrum via a Fast Fourier Transform.

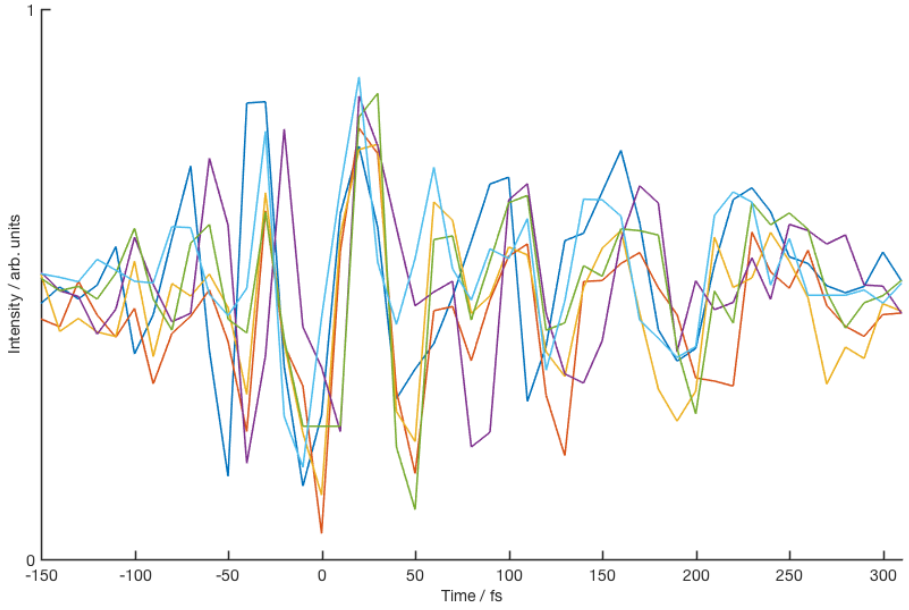

FIGURE 4.6: Time dependent harmonic intensity plots from each data run, showing the small adjustment made to correct for the time zero position.

Once all the data has been corrected for the time zero position, it is all summed together in order to try and remove as much noise from the spectrum as possible. The summed spectrum can be seen in figure 4.7.

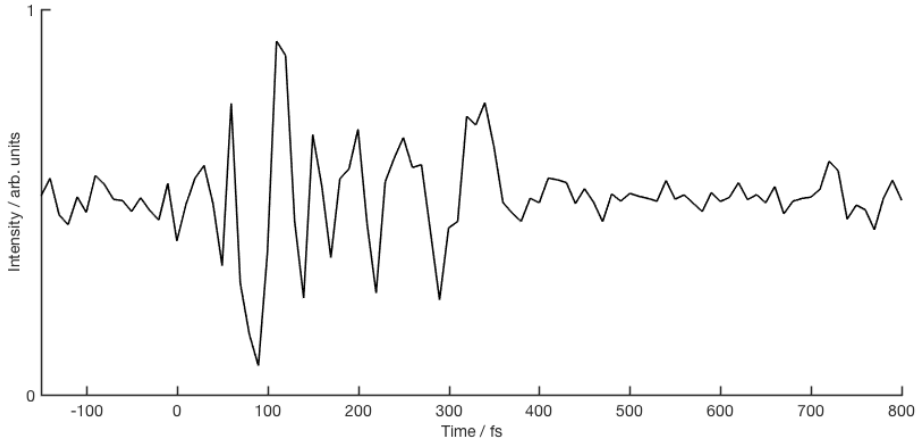

FIGURE 4.7: Time dependent harmonic intensity plot of all data runs summed together and normalised. The oscillations seen here are due to the molecular vibrations of CCl_4

In order to obtain a frequency spectrum a fast Fourier transform is performed upon the data. For each set, Fast Fourier Transforms are performed, for the raw data, the difference between the raw data and the smoothed data where the smoothed data takes a three point rolling average over the raw data, and the data before and after time zero, plots of these can be seen in figure 4.8.

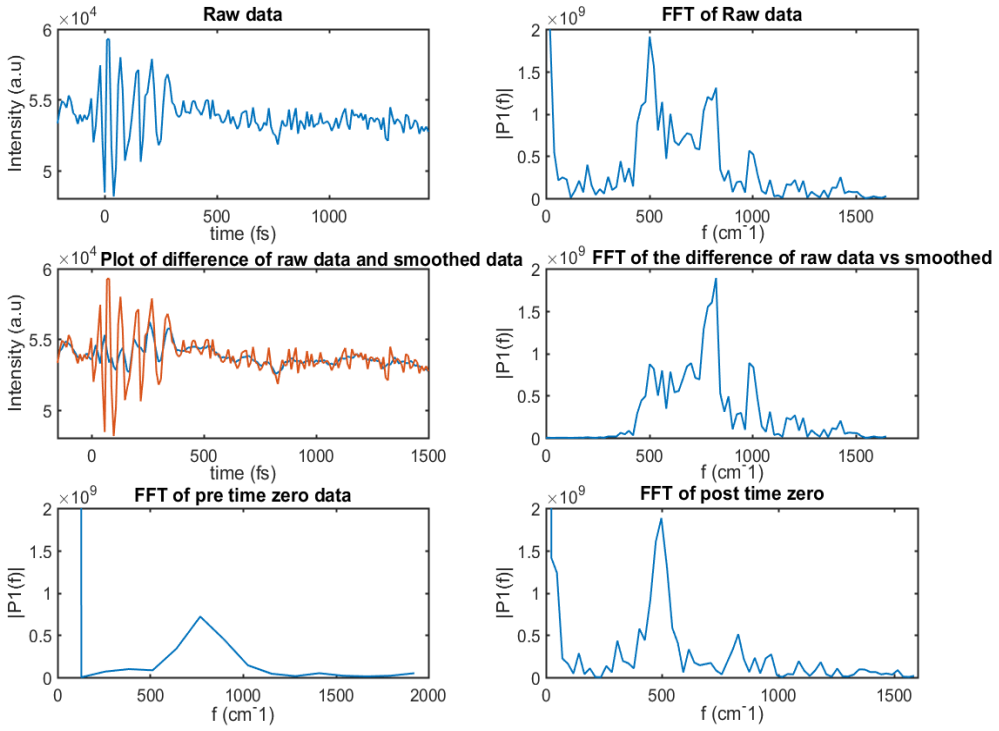

FIGURE 4.8: Raw data of harmonic intensity against time and the fast Fourier transforms performed on this data under different conditions, for the raw data set, the difference between the raw data set and smoothed data, the data before time zero and for the data after time zero. This is the data from a single run.

In figure 4.8 it can be seen that the Fast Fourier Transform for the raw data has significant contributions from the time zero peak. The Fast Fourier transform of the difference between the raw and smoothed data is in an attempt to dampen any noise within the raw data. However, this results in a significantly shifted spectrum as it removes signals from the spectrum that could provide significant information about the molecular vibrations. The Fast Fourier Transform with the clearest peaks in it is the one that is

taken from +50 fs. This is due to the removal of the interference effects that are caused as the two pulse overlap in time. The oscillation is induced by an intensity effect when the pulses are overlapped in time and therefore does not contribute to the molecular vibrations. The Fast Fourier Transform of the signal before time zero shows that there is some noise within the frequency spectrum but this is small.

Inspection of figure 4.8 shows that the region over which the clearest Fast Fourier Transform is obtained for the molecular vibrations within CCl_4 is with the removal of the time zero signal through to the end of the oscillations that are observed within the time trace. The total harmonic time dependent spectrum that is seen in figure 4.7 is Fast Fourier Transformed from +50 to 400 fs to try and remove as much noise from the experiment as possible, resulting in the cleanest frequency spectrum for the molecular vibrations. Figure 4.9 shows the Fast Fourier Transformed data with assignments of the vibrational bands.

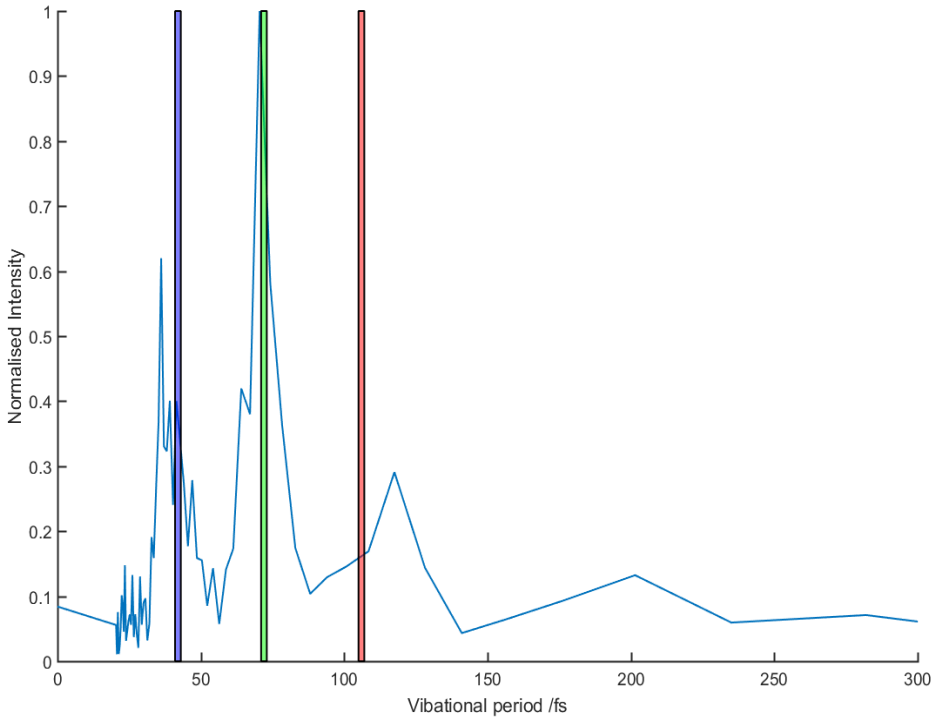

FIGURE 4.9: Fast Fourier transformed data of the summed time dependent harmonic intensity, including assignments from the know vibrational bands of CCl_4. Green is the A1 symmetric stretch, Blue is the F2 antisymmetric stretch and Red is the umbrella mode.

From figure 4.9 we note that not every Raman active mode has been observed experimentally. Comparing this to the Raman spectrum can be seen in figure 4.1, the Raman spectrum has considerably higher resolution than the spectrum we have obtained using high harmonic generation as the probe. The limited resolution is mainly due to the number of vibrational cycles that we observe. Other contributing factors are the time step limited by the stage, and the cross correlation time between the pulses. The shape and height of the different bands that are shown within both spectrum are not similar. The high harmonic spectrum is noisier, there are less points to make up each rise and fall and they appear broader. There are three clear peaks within the spectrum, two of which can be assigned as being the A1 symmetric stretch and the F2 anti-symmetric stretch respectively. The third peak is offset compared to where it would be expected due to

the limited number of vibrational cycles we observe, this is an experimental limitation. This peak is assigned as the F2 umbrella mode because there is a rise in the spectrum correlating to the expected period of this mode.

The peak that is expected at 150 fs, the bending mode (E) is absent due to the short lifetime of the vibrational wave packet. All oscillations within the raw spectra are over by 600 fs. The high harmonic generation process seems to be sensitive to these small changes that are induced from the created vibrational wavepacket. We have observed three out of four of the Raman active bands. The resolution of these bands is not exceptional however they can be clearly assigned.

The lack of observation of the peak at 150 fs can be attributed to the short time lifetime over which the oscillations within the spectrum have been observed. To investigate the effect of short lifetime of the observed oscillations on the Fast Fourier Transform, we create a series of simulated time traces and see how the duration effects the retrieved Fast Fourier Transform. This was be done by taking a series of sin waves of the same period as the expected oscillations, these sine waves are then cut between 500 fs and 1 ps. If we take the simulated spectrum and look at the Fourier transform of 500 fs it looks almost identical to our experimentally obtained spectrum. However if you look at the simulated spectrum where the oscillations have a lifetime of up to 1 ps all of the expected peaks can clearly be seen within the Fourier transform. Therefore it can be concluded that we do not see the 150 fs oscillation because of the short period over which the oscillations survive within the experiment. Figure 4.10 shows the simulated spectrum being Fourier transformed with the oscillations being cut at 1.4 ps and 500 fs. It is important to note that in the simulated spectrum the oscillations all have equal intensity and are not scaled as would be expected from the known Raman Spectrum.

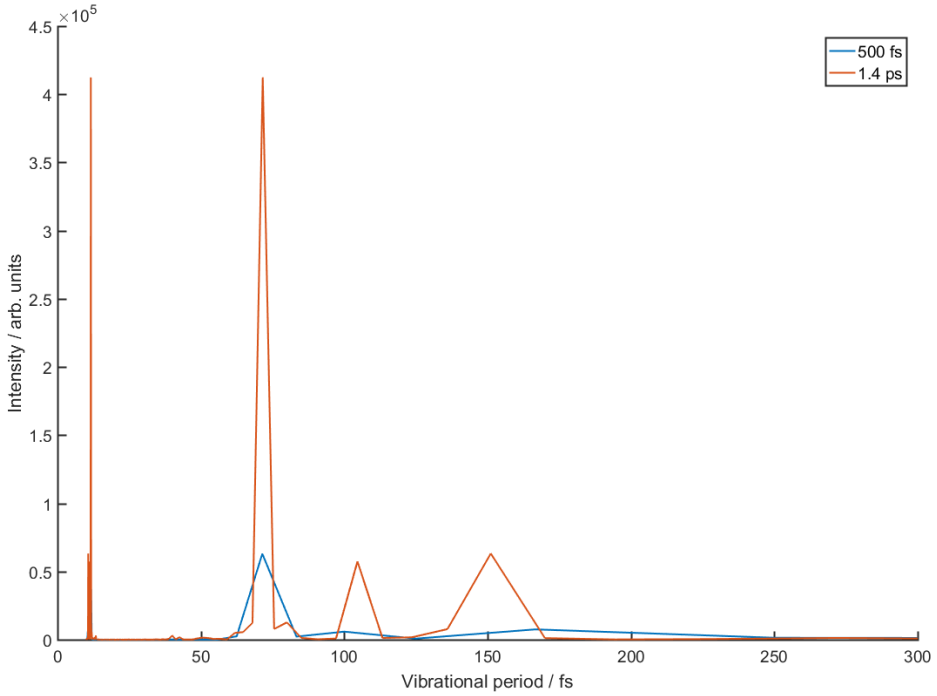

FIGURE 4.10: Fast Fourier transform of simulated data including assignments from the know vibrational bands of CCl_4.

Alongside the number of oscillations that are measured the time at which the oscillation is occurring relative to its measurement via the laser pulse will effect the observed peak. The simulation shown in figure 4.11 shows that for a 21 fs oscillation being measured with a 10 fs pulse, as the oscillation and laser pulse become offset in time relative to each other the Fast Fourier Transform changes significantly in shape. This shape change will the overall resolution of the spectrum. Whilst the oscillation is not on the same time as the oscillations in CCl_4 it clearly demonstrates the effect of the point at which oscillation is measured relative to the laser pulse on the Fast Fourier Transform. Increasing the number of samples that are taken will lead to this being averaged out so that a single peak appears in the Fast Fourier Transform, however this was not possible due to the short lifetime of the observation window. The number of cycles that were obtained could be increased in order to try and overcome this, however the short life of the observation window will have a greater effect on observing all of the vibrational bands within CCl_4, as seen in figure 4.10.

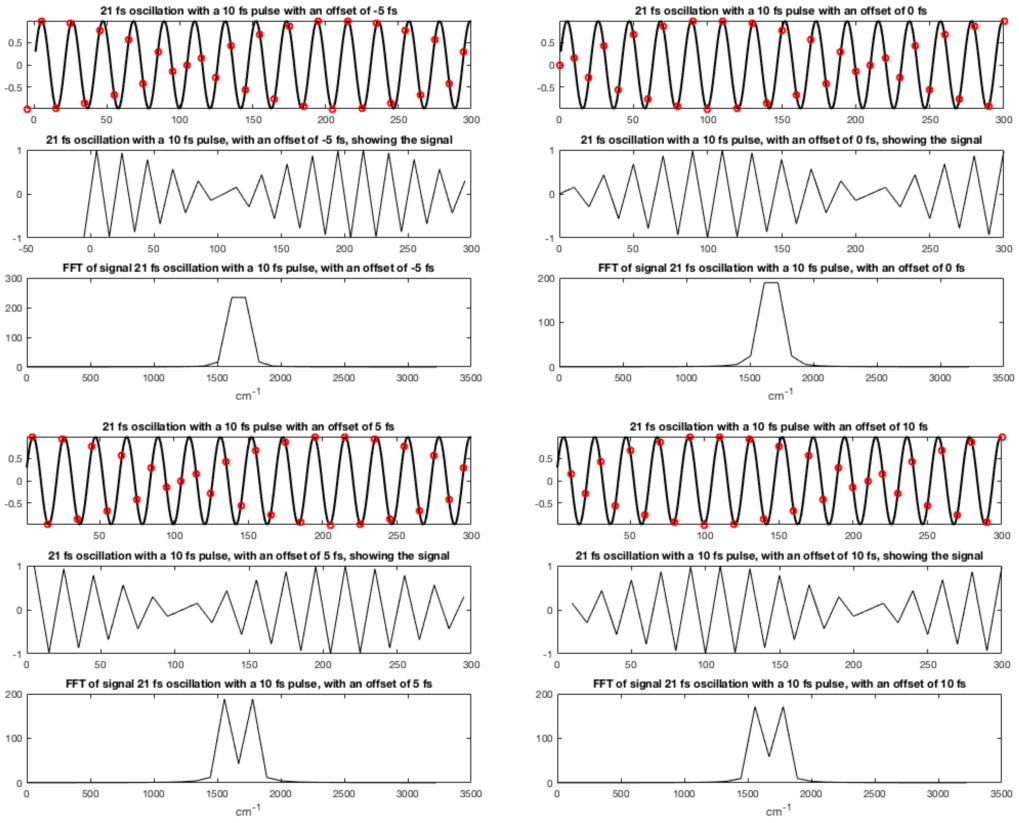

FIGURE 4.11: Simulation of making an observation of an oscillation on a 21 fs time scale using a 10 fs laser pulse. Including a Fast Fourier Transform of this signal showing a significant change in the shape of the Fourier Transformed data which is dependent upon where the oscillation is measured relative to the laser pulse. Each panel shows an offset between the oscillation and the laser pulse, from the top left, the offset is, -5 fs, 0 fs, 5 fs, 10 fs respectively. The offset in measurement results in a significant change in the Fast Fourier Transformed signal.

4.3.1 Theoretical work

In this section I will be discussing some theoretical work which has been carried out, with the intention of trying to gain an understanding of why high harmonic generation is sensitive to the small changes that occur during molecular vibrations. The high harmonic generation process can be broken down into three simple steps, ionisation, acceleration and recombination. From the three step model we can see that ionisation affects the high harmonic generation process. Therefore if the ionisation potential changes as the

molecule undergoes vibrational motion, the harmonics produced will change in intensity as ionisation potential effects the ionisation rate. The ionisation rate can be approximated using atomic ADK. The recombination step is dependent upon the overlap of the initial ground state vibrational wavepacket that is produced with the ion state vibrational wavepacket. The changes that occur during the 1.3 fs where the laser field is accelerating the electron are significant where you have light atoms. For example, hydrogen atoms move the fastest and result in a significant change in this time period. For heavier atoms the effect is shown to be insignificant due to their slower motion. During the time until recombination we can approximate the motion within the molecule to be zero.[75] In terms of the vibrational period, the overall change as a percentage of each vibrational mode can be seen in table 4.3.1:

Mode	Vibrational period (fs)	Percentage change in 1.3 fs
A1 (sym str)	72	1.8
E (bend)	153	0.85
F2 (anti sym)	42	3
F2 (umbrella)	106	1.2

TABLE 4.2: The percentage change in each vibrational mode over 1.3 fs, which is a half cycle of 800 nm the time over which high harmonic generation occurs.

As can be seen in table 4.3.1 the percentage change for each molecular vibration is small over the time required for high harmonic generation and we will be focusing on the change in ionisation potential across each vibrational mode. One thought is that the ionisation potential change from one edge of the vibrational wave packet to the other is sufficient enough that the harmonics produced whilst the molecule is undergoing this type of motion can be observed. If we examine the symmetry group for CCl_4 (Td) the transition to each of the modes from the ground state to the ion state is allowed. Especially considering ionisation relaxes symmetry constraints. The ionisation step results in the relaxation of symmetry rules as with photoelectron spectroscopy.

In order to do these computational calculations the initial structure of CCl_4 will be found and optimised for the various vibrational frequencies calculated. These calculations were done using Gaussian 09, with a density functional theory calculation (B3LYP) and a basis set of pDVZ. Initially the calculations were performed with a very small basis set in order to keep the calculations computationally cheap and quick to run. The initial calculation was carried out with 6-31g. These calculations were benchmarked against the NIST computational database, CCBDC, to confirm there accuracy.[76] The vibrational frequencies obtained from both basis sets identically matched those on NIST, therefore confirming the calculations accuracy.

The calculations performed show a high level of accuracy when benchmarked. However, the pDVZ basis set is quite small considering the large size of the Cl atoms that are to be considered within CCl_4. The large number of electrons means that a larger basis set is required in order to get calculation as accurate as possible. The method that we have selected is not necessarily the best method for a high level of accuracy in the absolute energy obtained across the potential energy curve. However, the shape of the curves are critical here to allow us to calculate the change in ionisation potential across each vibrational mode. Whilst the absolute energy for each point on the potential energy curve may not be absolute, the overall shape for the vibrational mode will be correct. The accurate shape will provide us with a simple model of the change in ionisation potential which we can use to assess the effect of the change in ionisation potential across a vibrational mode on high harmonic generation. The assumption here is that providing the shape is the same, the overall numerical accuracy is not critical in providing insight into the effect upon the high harmonic generation process. At the equilibrium geometry the ionisation potential is identical to the know value for CCl_4 but as we progress across the vibrational motion toward the edge the accuracy may not be exact in number, however the relative change should remain accurate.

Upon confirming we had the initial starting geometry optimised and the various vibrational frequencies agreed with the expected values from the database further calculations were performed. For a series of configurations along each vibrational mode we calculate the difference in energy between the ground state and the ion, which is equivalent to

the ionisation energy. This allowed us to calculate the ionisation potential across each vibrational mode relative to a bond angle or length change within the molecule. In the projection upwards to calculate the ionisation potential, the heavy nature of Cl is such that the molecular geometry will remain unchanged. The high harmonic generation process occurs in half a laser cycle which at 800 nm is 1.3 fs. Over this time the heavy Cl atom has moved a distance which is approximately zero. For each potential on the surface the change in ionisation potential is then calculated with the relative change in the particular bond length or angle for the mode being examined. The ionisation potential is calculated from the difference between in energy between the ground state and the ion state, the vertical transition.

We then consider the change in ionisation potential over the energy range experienced by the vibrational motions in our experiment. The assumption here is that we start in the ground state and have maximum vibrational quantum number of three for each vibrational mode, so the full range for each potential includes $v = 1$ to $v = 3$. The table 4.3 shows the maximum change in ionisation potential experienced by the molecule over a vibrational period.

Mode	Energy change (eV)
A1 (sym str)	0.14
E (bend)	0.07
F2 (anti sym)	0.25
F2 (umbrella)	0.14

TABLE 4.3: Each mode in CCl_4 and the change in ionisation energy across each mode. Assuming that there is a maximum vibrational quantum number of three for each mode.

Examination of the potential energy surfaces show that from the equilibrium geometry every mode (other than the symmetric stretch) has a minimum either side of the equilibrium geometry in the ionisation potential. From this we might expect to observe each vibration at twice the vibrational frequency, with the exception of the symmetric stretch as seen in figure 4.12. The minimum either side of the equilibrium geometry would increase the ionisation yield increasing the harmonic intensity, we might then expect to

observe each of these at twice the expected frequency. While this simple theory predicts this we do not observe this in the experiment.

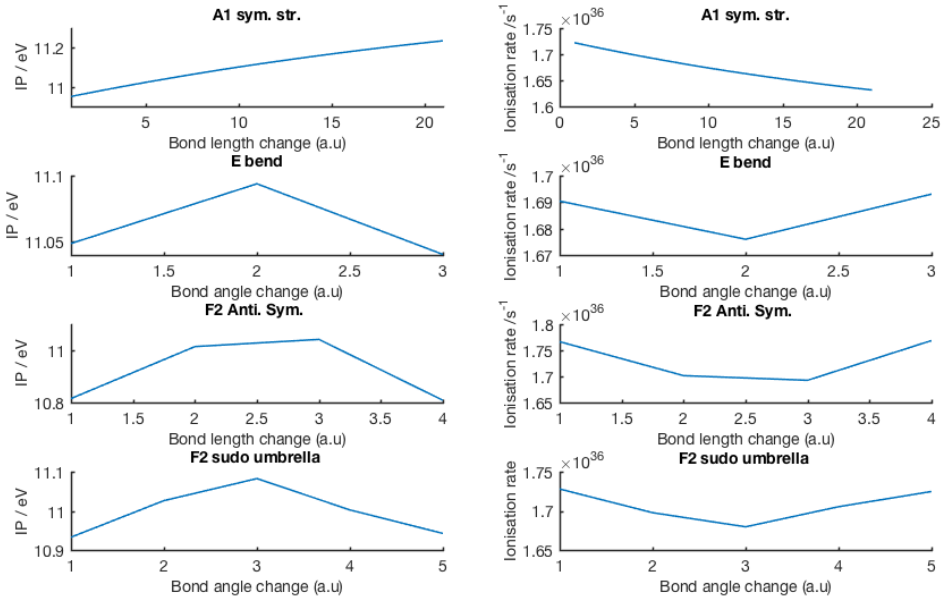

FIGURE 4.12: Change in ionisation potential for each mode, and atomic ADK calculations for how the ionisation rate changes with IP across these.

As a first approximation we calculate the ionisation rate using atomic ADK theory. The change in ionisation rate for the mode (F2 anti sym) with the maximum change in ionisation potential is 4%. This change is minimal, suggesting that changes in harmonic yield would be negligible. The origin of the sensitivity of high harmonic generation is therefore not from this, and recent theoretical work suggests there is interference between vibrational pathways.[72]

4.4 Conclusions and Further work

Through the observation of vibrational motion in CCl_4 we have commissioned and optimised a new experimental capability for high harmonic spectroscopy. The experiments allow us to monitor simple vibrational motion. However this is limited by rotational de-phasing effects. Preliminary calculations to look at the sensitivity of high harmonic

generation to various process have been carried out however these have been inconclusive. In order to gain a comprehensive understanding of what is happening to the vibrational wavepacket in CCl_4 additional experiments could aid with the understanding.

Chapter 5

Photoelectron Spectroscopy of Ammonia using multiphoton ionisation at 400 nm

The work presented in this chapter is based on publication Smith et al. Phys. Chem. Chem. Phys. 2016, **18**, 28150-21856, the work has been carried out at Artemis in the Central Laser Facility, UK.

5.1 Introduction

The UV photolysis of ammonia has provided a model system for the study of non-adiabatic dynamics. In the $\tilde{A}$-state (first electronically excited singlet state) the dynamics of dissociation involve transitions at a conical intersection. Competing non-adiabatic and adiabatic dissociation processes leads to hydrogen abstraction in conjunction with ground or excited state NH_2 molecular fragments forming respectively.[77–94] Whilst ammonia's molecular structure is relatively simple it exhibits complex photochemistry, therefore these processes can be investigated in a small molecular system. The lack of universal detection techniques that can provide clear information about the full reaction mechanism drives the continued interest in this small molecular system. To improve

the observation window attainable with a photoelectron spectroscopy probe, a resonant multi-photon ionisation probe at 400 nm was used. This probe ionises the molecule through the $E^{'}$ $A1^{'}$ Rydberg state allowing access to a different set of vibrational states when compared to direct ionisation of the $\tilde{A}$-state. This probe also increases the time period over which ionisation can occur.

A large proportion of information about the excited state potentials important to the photodissociation dynamics of the ammonia $\tilde{A}$-state, arises through potential energy surface calculations.[78,81,90,95,96] The structural and dynamical features important in the dissociation process have been emphasised by the theoretical studies. The electronic ground state of ammonia has an equilibrium pyramidal structure while the excited $\tilde{A}$-state has a planar equilibrium structure. This results in a vibrational progression in the umbrella mode, ν_2, which dominates the UV absorption spectrum. In the electronic excitation process a lone pair electron is promoted from the nitrogen atom into a Rydberg type orbital of $3s$ character. N-H bond length extension leads to a small barrier large enough to make the lowest two vibrational states of the dominant ν_2 mode bound. As the H-NH_2 bond is extended further the orbital increases in σ^* character leading to dissociation. At extended N-H bond lengths the ground and excited state potentials cross at a conical intersection where the molecule can dissociate into ground or excited state molecular fragments. This is dependent on the energy available and how the molecule traverses this region. In full dimensional calculations of the potential energy surface, the conical intersection is only seen at planar geometries.[81] The threshold for excited state product formation is 6.02 eV, which lies significantly above the barrier to dissociation (5.94 eV) seen at shorter N-H bond lengths.

Based on absorption spectroscopy, initial measurements suggested lifetimes in the $\tilde{A}$-state were on the order of 35 fs.[86,87,92] Subsequent measurement and analysis of the energy partitioning between the internal molecular motions of the NH_2 fragment and the kinetic energy released[85,93,97,98] demonstrate that tunneling leads to vibrationaly cold molecular fragments. It also shows that the vibrational energy in the NH_2 fragment increases with the photon energy.[85] Once the energy is adequate to drive formation of the excited state NH_2 fragment, this process is observed. Generally the relative portion

of excited state fragment increases with increasing energy.[85] As a result the dynamics can be roughly divided into three regions. Firstly, when dynamics are below the barrier to dissociation, the dissociation time scale is controlled by tunnelling, resulting in very low levels of vibrational excitation in the ground state NH_2 fragment produced. Then, as higher vibrational states are excited, over the barrier dissociation becomes possible and a shorter dissociation time is expected and observed. Finally, at energies above the barrier but below the adiabatic dissociation threshold ground state dissociation products are formed. As the excitation energy is increased above 6.02 eV, fragments from the excited state can also be formed and the two channels effectively compete with the dynamics at the region of the conical intersection controlling which dominates.

More recently time resolved photoelectron spectroscopy and time resolved kinetic energy release measurements have been applied to this problem. Resonant ionisation of the hydrogen fragment has been used in kinetic energy release measurements to highlight the different lifetimes associated with different levels of internal energy in the molecular fragments.[77,79,94,99] Various decay pathways have been correlated with the different lifetimes, with some invoking complex dynamics around the conical intersection as a possible intermediate where population can be trapped for several hundred femtoseconds before dissociation occurs.[99]

The effectiveness of photoelectron spectroscopy has been limited by the often restricted observation window afforded by the available UV probes. At its base level, photoelectron spectroscopy is a universal detection technique as all states can be ionised. The practical limitations arise from the ionisation potential changing as a function of molecular geometry. With conventional laser sources the overlap of the excited state wavepacket with the molecular ion states is therefore rather short lived, limiting the observation window. Combined with this, it is desirable to reduce the background contribution to the retrieved photoelectron spectrum such that the energy of the probe photons is often lower than the maximum available. In ammonia the use of a lower energy stops the probe from exciting the $\tilde{A}$-state, which would make measuring the early time dynamics difficult due to significant probe pump contributions at early times. This restricts the probe wavelength to being >215 nm. Recent experiments have restricted the observation window to

the first 75 fs following excitatoin by using a 240 nm probe.[77] However, the ion kinetic energy release measurements suggest the lifetime associated with dissociation can be up to 400 fs for some dissociation processes.[99] This means there is a large component of the excited state dynamics not being measured by either technique. Increasing the energy of the probe to 200 nm is unlikely to increase the observation window extensively. Furthermore, when combined with the issues surrounding the analysis of the early time dynamics it is unlikely to provide any extra information from a probe at 240 nm. By using a very high energy probe the restriction on the observation window could potentially be removed however, these experiments are extremely complex.[100–102] One potential solution is to use multiphoton ionisation of the excited state population while maintaining an almost background free signal. The information content can often be maximised if one of the absorption processes is resonant with an intermediate Rydberg state. The time dependence of the resonance conditions provides ample data to analyse the time dependence of the signal. In the experiments described below, we use a multiphoton probe at 400 nm to increase the observation window available to photoelectron spectroscopy measurements and can monitor excited state population out to several hundred fs. The absorption of the first probe photon populates the $E'\ ^1\mathrm{A}_1'$ Rydberg state that allows for an extended view of the excited state potential surface. By ionising through the Rydberg state we also access a different set of final ion states, allowing access to the lowest vibrational levels of the molecular ion. The use of a resonant multiphoton probe maximises the observation window through changes in the Franck-Condon (FC) factors involved in the ionisation process, maintaining overlap with the accessible ion states for extended period. The measurements show none of the complications associated with high energy single photon probes and provide vibrational state dependent lifetimes that allow us to separate the adiabatic and non-adiabatic pathways to dissociation.

5.2 Experimental

A full description of the experimental details are presented in chapter 2.3, and as such a brief description of the experimental will be provided here. Both the pump and

probe arms of the experiment are separated before compression, allowing for independent control of the pulse energy and compression. The pump pulse is produced via fourth harmonic generation (FHG) of the fundamental (800 nm), generating photons at approximately 200 nm. The 200 nm beam is produced using standard non-linear optics with sequential second, third and fourth harmonic generation in BBO. Second harmonic generation takes place by frequency doubling whereas both third and fourth harmonic generation take place via sum frequency generation. The energy per pulse generated at the fourth harmonic is controlled through the use of a waveplate in the third harmonic generation arm which controls the efficiency of the mixing process. The pulse energy is kept to 2 μJ, which maximises the pump probe signal while maintaining a low to pump photon ionisation background signal. It is essential to make sure that a low pump photon ionisation background signal is maintained throughout the experiment so that in all collected ionisation signals there is little background from this multiphoton process. The pump beam is focused to the centre of the interaction region of the VMI spectrometer, with a 1 m focal length mirror where it intersects the molecular beam. To generate the probe, 1 μJ of the 800 nm beam is frequency doubled in BBO to produce approximately 5 μJ at 400 nm. The absolute pulse energy is controlled using half waveplate before the doubling crystal to control the phase matching in the crystal and desired intensity at the interaction region. The probe beam is then reflection focused in the toroidal mirror chamber, using a 1 m toroidal mirror to the centre of the interaction region of the VMI spectrometer where it crosses with the pump beam. The pump probe delay is controlled using a motorised translation stage which moves the pump beam relative to the probe beam in time. A molecular beam is used, this is is produced using a pulsed nozzle gas jet (Amsterdam cantilever) and a skimmer. The gas used throughout the experiment is 5% ammonia in helium, with the nozzle being backed by 1 bar of pressure, this is insufficient pressure to lead to significant formation of ammonia clusters.

The data was collected using a VMI spectrometer which is described in chapter 2.3.3.1. Time steps were recorded from -300 fs to +500 fs in steps of 20 fs, each cycle was recorded and saved. Each cycle was recorded with short exposure times to avoid saturation of the camera. Each step was recorded progressively in time as opposed to sitting on a data point and collecting for along time accumulatively in order to prevent any experimental

fluctuations effecting the data. For example if the laser intensity drops; the gas runs out or there was an electrical fault, the affected run could be removed from the data. A total of 100 cycles were recorded and used throughout this work, this resulted in good signal to noise levels so each peak in the spectrum can be assigned.

5.3 Results and Discussion

The photoelectron velocity distribution is obtained from the two-dimensional images by means of POP. POP peels the image from the outside to the central point, using the polar onion peeling method.[103,104] The code outputs a cut through the reconstructed 3D photoelectron distribution that resulted from the experimental image. To obtain a spectrum POP integrates the image radial from the centre to obtain a velocity spectrum, this can be converted into kinetic energy via $\frac{1}{2}mv^2$ which is calibrated from know bands in argon photoelectron spectrum. The photoelectron kinetic energy is proportional to r^2, where r represents the distance from the centre of the image. Energy distribution spectra are subsequently produced by converting from a velocity distribution by multiplying the integrated photoelectron count by the 1/r Jacobian factor. The photoelectron angular distribution can also be acquired from the output of the POP code. The photoangluar distribution following one-photon ionization of an isotropic ensemble of closed shell species using plane polarized light takes the form $I(\theta) \propto 1 + \beta P2(cos\theta)$, where θ is the angle between the laboratory frame z-axis and direction of ejection of the electron, β is the anisotropy parameter and $P2(cos\theta)$ is the second-order Legendre polynomial. When processing the images, a background image with no laser on just gas is taken, in order to remove the background signals from the spectrum. Additionally, the single colour spectrum is subtracted from the image which is the 200 nm alone signal, this spectrum was taken at -2 ps. The probe only signal is negligible. A raw VMI image of this can be seen in figure 5.1.

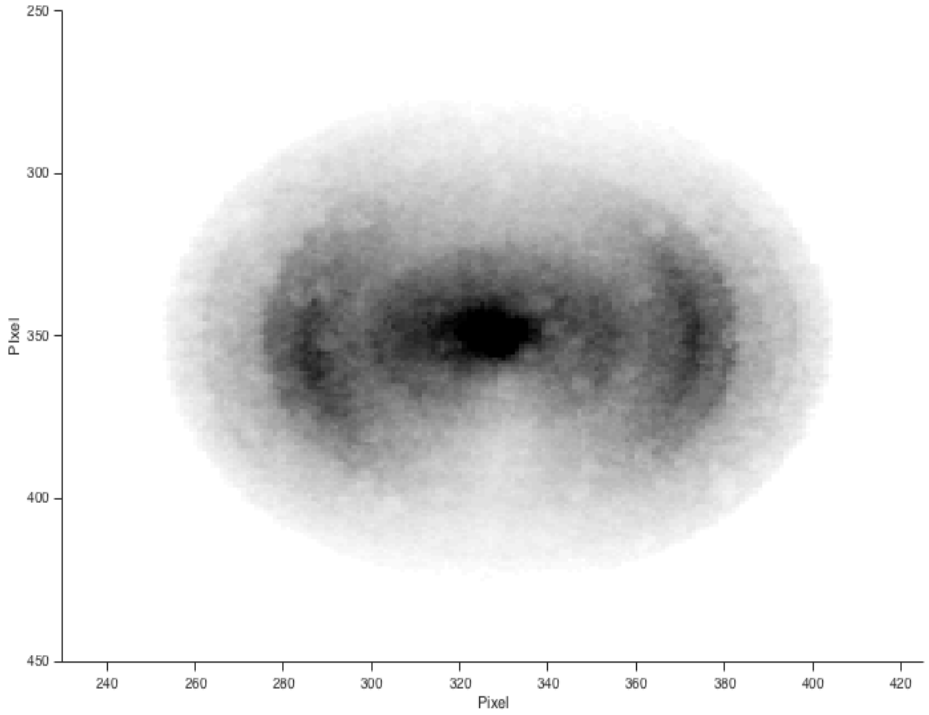

FIGURE 5.1: A raw VMI image that has been collected, this is before processing with POP in order to obtain a spectrum

This image is then processed using POP to allow us to obtain a photoelectron spectrum at a particular time step. The time resoled spectrum is obtained by processing every image, to get a spectrum at each time point resulting in the overall time dependent spectrum, this can be seen in figure 5.2

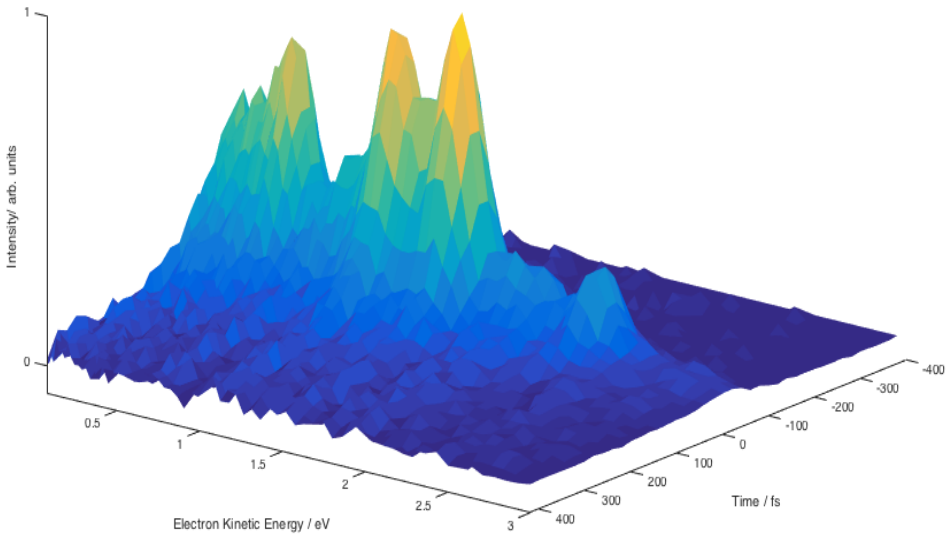

FIGURE 5.2: Surface plot of the full time resolved photoelectron spectrum obtained following excitation of the NH_3 $\tilde{A}$ state at 200.8 nm. The photoelectron spectra are obtained following multi-photon ionisation with a 400 nm probe.

The time resolved changes in the photoelectron spectrum obtained can be seen in figure 5.2. This represents the complete data that has been collected throughout this study. The NH_3 ground state is initially pumped with 200.8 nm exciting the molecule into its $\tilde{A}$ state, the molecule is then probed via multi-photon ionisation with a 400 nm probe. The spectrum shows a series of peaks that correspond to the vibrational bands within the NH_3 ion. The intensity is dependent on the overlap of the vibrational wavepackt in the $\tilde{A}$ state, with accesible vibrational states in the ion. The excitation schemes for the photoelectron spectra can be seen in figure 5.3 A, showing the total energy between the 1+2′. As a comparison we also collected the 1+1 spectrum which has the same total energy but does not ionise through the intermediate Rydberg state, the energy for this is also shown on A. The 1+2′ goes via the Rydberg intermediate whereas the 1+1 doesn't go directly via this intermediate and for comparison the spectra obtained from the two

different excitation schemes are significantly different these can be seen in B and C. The assignments of the bands can be seen in Figure 5.3.

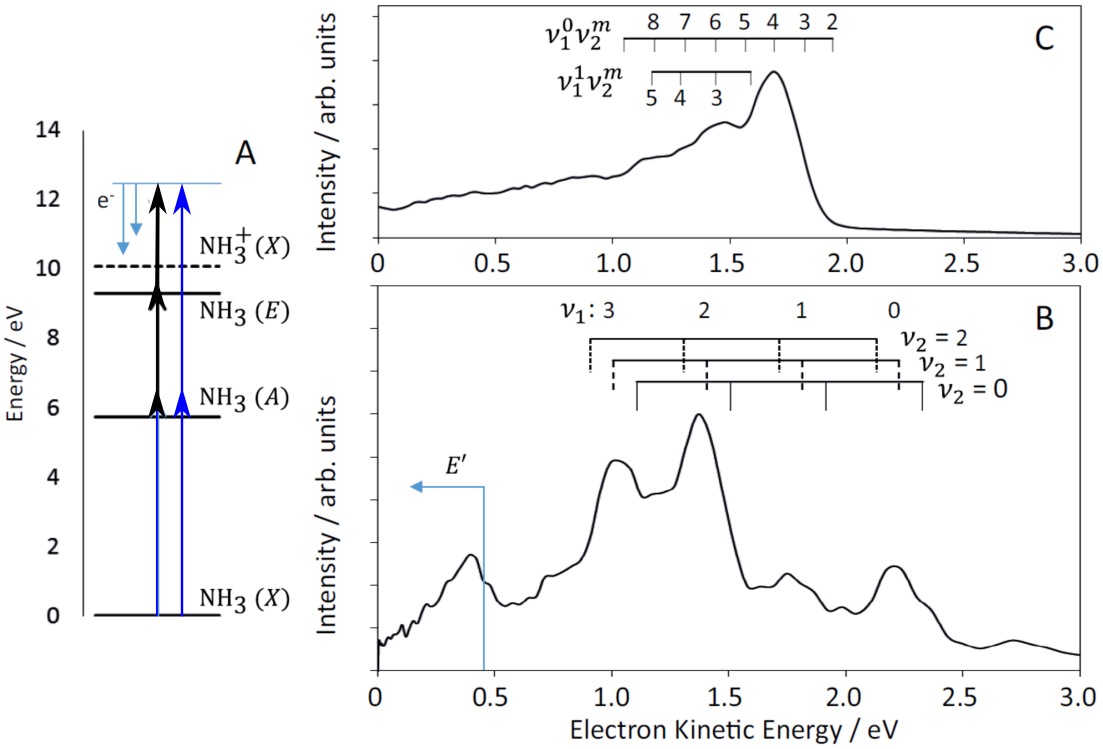

FIGURE 5.3: A. Excitation scheme showing the resonant absorption processes and the ground ion state, blue arrows represent a 200 nm photons and the black arrows represent 400 nm photons. The left hand scheme is for the excitation of the 1+2′ photoelectron spectrum shown in B, the right hand scheme is for the 1+1 photoelectron spectrum seen in C. B. 1+2′ Photoelectron spectrum and assignment of the time zero photoelectron spectrum. The combs above the plot show the dominant vibrational states in the photoelectron spectrum originating from the ground ion state. The region below 0.4 eV is assigned to the 2E′ excited state of the ion. C. 200.8 nm 1+1 Photoelectron spectrum and assignment as a comparison to the 1+2′ photoelectron spectrum in B.

In Figure 5.3A, left hand side, we show the excitation scheme that is followed for the experimental data, that is shown in figure 5.3 B. In Figure 5.3B we plot the background subtracted photoelectron spectrum for NH_3 obtained when the pump and probe are time overlapped. The pump beam populates the ν_2^4 vibrational level of the $\tilde{A}$-state, which is then subsequently ionised by the absorption of two or three 400 nm photons.

Absorption of two photons leads to a total photon energy of 12.47 eV which is 2.4 eV above the ionisation potential for the ground, $2A'$, ion state. Absorption of a third photon increased the available energy to 15.6 eV which is 0.39 eV above the vertical excitation energy of the $2E'$ ion state., providing another possible ionisation channel. The spectrum therefore contains features that correspond to these two ion states, and shows clear vibrational structure originating from the electronic ground state of the ion. The intensity of the probe is kept to a level that minimises two photon non-resonant excitation of the $\tilde{A}$ state. This means we do not observe any dynamics at negative time delays and means any probe-pump contributions to the spectrum are minimal. This is confirmed by the fact that we obtain the same, albeit noisier, photoelectron spectrum at times outside the cross-correlation. There is a third feature within the spectrum whilst small is seen at around 2.6 eV. This is from the NH_3 dimer. During this experiment the formation of clusters was minimised however was not zero. This band whilst observed is not analysed during this work. A more in depth study of the NH_3 dimer was carried out alongside this work, more details can be seen in Horke et al.[105] At high electron kinetic energies (<0.5 eV) a clear vibrational progression is observed corresponding to ionisation into vibrationally excited states of the $2A'$ ground ion state. We assign the vibrational features based on an anharmonic oscillator model of the form.

$$E = \omega_{e1}\left(\nu_1 + \frac{1}{2}\right) - \omega_{e1}\chi_{e1}\left(\nu_1 + \frac{1}{2}\right)^2 + \omega_{e2}\left(\nu_2 + \frac{1}{2}\right) - \omega_{e2}\chi_{e2}\left(\nu_2 + \frac{1}{2}\right)^2 \tag{5.1}$$

Where ω_{ei} and $\omega_{ei}\chi_{ei}$ are the harmonic and anharmonic vibrational frequencies of the ith vibrational mode of the ground ion state of ammonia and ν_i is the vibrational quantum number of the state populated. The literature values used are taken from Xie et al.[106] and result in the expected kinetic energies given in the Table 5.3 and assignments shown in Figure 5.3 B as the combs above the data. The assignments highlight a progression in the ν_1, symmetric stretch, in combination with various quanta in the umbrella mode, ν_2. Based on the calculated positions, the $\nu_2 = 1$ peaks show the highest intensity at all levels of excitation of ν_1 with the maximum seen at $\nu_1^2\nu_2^1$ level. The strongly overlapping nature of the features means that this is a rough assignment and slightly shifts the

	$\nu_1 = 0$	$\nu_1 = 1$	$\nu_1 = 2$
$\nu_2 = 0$	2.33	2.23	2.13
$\nu_2 = 1$	1.92	1.81	1.72
$\nu_2 = 2$	1.51	1.41	1.31
$\nu_2 = 3$	1.11	1.01	0.91

TABLE 5.1: Expected electron kinetic energies in eV for the various vibrational states in the NH_3^+ state calculated using equation 5.1. ν_1 labels the symmetric stretch and ν_2 labels the umbrella vibration.

measured peak maxima from what might be expected for well resolved peaks. As such we define each of the features by the level of excitation in the symmetric stretch only.

Each feature in the spectrum associated with the $2A'$ state is therefore treated as having a different quanta of vibrational energy in ν_1 and is labelled by this quantum number in the rest of this discussion. The broad low energy feature at 0.38 eV does not correlate well with the expected vibrational progression by correlates energetically with what would be expected following three photon ionisation into the $2E'$ state. We therefore assign this feature to ionisation into the excited $2E'$ state. The broad feature contains no vibrational structure, so this is treated as a single feature in fits described later. There is also a small feature between 2.5 and 3 eV which is due to ionisation of the ammonia dimer which makes up a small component of our molecular beam.

By comparing the photoelectron spectrum obtained with single photon ionisation measurements of the $\tilde{A}$-state we see very clear differences. In figure 5.3 C we plot the 1 + 1 photoelectron spectrum at 200.8 nm. This provides almost exactly the same energy as the 1 + $2'$ ionisation process and the spectrum shown in Fig. 1B has a drastically different appearance. In the direct ionisation measurements, a strong $\delta v = 0$ propensity is observed such that ionisation from the ν_2^4 vibrational level predominantly leads to population of the ν_2^4 level in the ion, with lower energy vibrational levels having a negligible intensity in the observed photoelectron spectrum.[77] The vibrational progression in the single photon experiments is in the ν_2 mode with at most one quanta in the ν_1 mode, such that the spectrum is dominated by the $\nu_1^0\nu_2^m$ progression.[77] This is contrary to our findings where the dominant vibrational progression correlates with a change in the vibrational quantum number associated with ν_1 with high levels of vibrational excitation in this mode. This is in conjunction with a progression in ν_2 with a dominant

transition into the $\nu_2 = 1$ level for all levels of ν_1. The reason for the dramatic changes is the resonant excitation process at the single photon level. Absorption of a single 400 nm photon excites the E′ $^1A_1'$ Rydberg state. The resonant excitation and finite duration of the laser pulses changes the Franck-Condon factors associated with ionisation, enhancing overlap with a different set of vibrational states. The states observed broadly match those presented in[107] where the E′ Rydberg state is accessed through a non-resonant two photon process at 266 nm, followed by ionisation with a time delayed 400 nm photon. The spectrum is however not identical to that obtained from directly accessing the E′ Rydberg state, but contains a fingerprint associated with the $\tilde{A}$ state character. The similarity of the spectra does however confirm that ionisation proceeds through the intermediate E′ Rydberg state. The relative complex spectrum obtained from ionisation of the Rydberg state is somewhat contrary to what may be expected. Ionisation of Rydberg states is often associated with strong $\delta v = 0$ propensity due to the strong similarity of character between the Rydberg and ion state.

This often leads to a strong single feature in the photoelectron spectrum obtained. The E′ state shows a more complex propensity with previous measurements showing the dominant transition is of $\delta v = 1$ character, suggesting there are significant differences in the shape of the E′ and ion states.[107] The difference in ionisation propensity for the $\tilde{A}$ and E′ states means the transition between them is likely to involve a change in vibrational state and is the reason for the rather different appearance of the two photoelectron spectra.

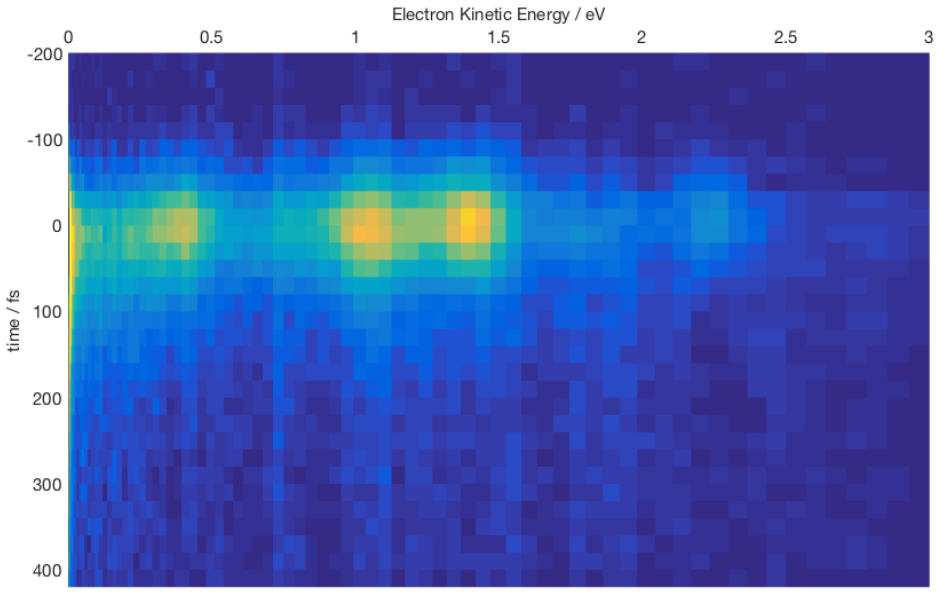

FIGURE 5.4: colourmap of the time and energy dependent photoelectron spectrum obtained following excitation of the ν_2=4 vibrational level of the electronic A-state and ionisation with multiple 400 nm photons.

In figure 5.4 we plot the time dependence of the full photoelectron spectrum. Each peak in the photoelectron spectrum rises together followed by what appears to be a bi exponential decay. In common with previous single photon ionisation experiments we do not observe any energy shifts as a function of time.[77,94] To highlight the decay dynamics we plot lineouts for each of the features associated with the various levels of ν_1 excitation. In each case the early time signal follows the intensity profile of the instrument response function, which is obtained from the cross-correlation of our pump and probe beams. The instrument response function corresponds to a Gaussian of full width half maximum of 108 fs. In the longer term, the dynamics show an exponential decay such that we fit the overall experimental signal as a combination of a Gaussian, representing the instrument response function, plus a component which is the Gaussian instrument response function convoluted with an exponential decay,

$$I = N_1 e^{\frac{\lambda}{2}(2\mu+\lambda\sigma^2-2t)} \operatorname{erfc}\left(\frac{\mu+\lambda\sigma^2-t}{\sqrt{2}\sigma}\right) + N_2 exp^{\frac{-t-\mu^2}{2\sigma^2}} \tag{5.2}$$

Where μ is time zero, λ is the decay constant, σ is the full width half maximum of the instrument response function and t is the time step. N_1 and N_2 are normalisation constants of the two signal components. The Gaussian contribution to the overall signal is due to strong-field ionisation as the two laser pulses overlap in time and provides a fingerprint for ionisation from the Franck-Condon region. Information about the dynamics is then contained within the lifetimes obtained from the second component in the fit. Each feature was fitted simultaneously using a least squatted method, with the fits to equation 5.2 plotted in figure 5.5 along with the Gaussian instrument response function and a Gaussian convoluted with an exponential decay. The energy ranges used and lifetimes ($1/\lambda$) obtained from the fits are given in table 5.2. The plots and table show that each of the vibrational features has a different associated lifetime, suggesting that the Frank-Condon factors associated with the multiphoton ionisation are changing as a function of time and that these could provide a sensitive probe of the excited state dynamics.

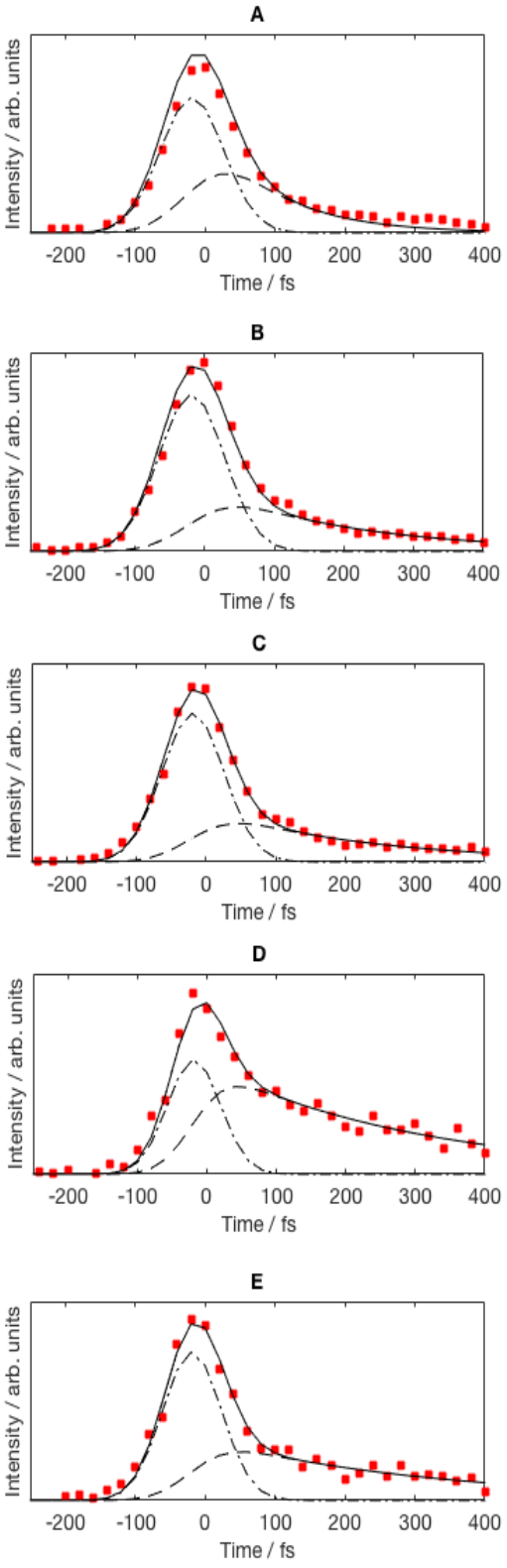

FIGURE 5.5: Experimentally measured (data points) time dependence of the photoelectron intensity for the main features observed in the photoelectron spectrum as well as the corresponding fits to equation 5.2 (solid line) and the Gaussian IRF (dot dash line) and exponentially decaying (dashed line) components of the fit. The plots correspond to the ionisation into the (A) 2E′, (B) 2A′ ν_1^3, (C) 2A′ν_1^2, (D) 2A′ ν_1^1, (E) 2A′ ν_1^0 ion states. The energy regions used and lifetimes obtained are given in table 5.2

TABLE 5.2: Decay lifetimes derived from the fits of the experimental data to equation 5.2.

Energy range / eV	Ion state	Vibrational state	Lifetime / fs
0.34-0.4	$2E'$	-	184 ± 14
1.0-1.06	$2A'$	ν_1^3	212 ± 17
1.32-1.5	$2A'$	ν_1^2	228 ± 25
1.69-1.81	$2A'$	ν_1^1	307 ± 26
2.26-2.44	$2A'$	ν_1^0	325 ± 54

The fits provide a different lifetime for each of the features associated with each electronic and vibrational state of the ion. Longer lifetimes are found for features of higher electron kinetic energy, correlating with lower levels of excitation in the symmetric stretch in the ground state of the ion. The shortest lifetime is associated with ionisation into the $2E'$ excited ion state at an electron kinetic energy of 0.3 eV, which has a lifetime of 184 fs. The vibrational features associated with ionisation into the $2A'$ state have longer lifetimes, with the lifetimes seen to increase as the vibrational energy in the ion state is reduced. The highest internal energy feature of the $2A'$ state, associated with the ν_1^3 vibrational level, has a lifetime of 212 fs, while the lower energy ν_1^0 has a lifetime of 325 fs. The lifetimes are significantly longer than the < 75 fs derived from photoelectron spectroscopy measurements using direct ionisation from the $\tilde{A}$-state.[77] A key point from all of these measurements is that the timescales derived correspond to the time it takes for the excited state wavepacket to leave the observation window of the experiment, as usually set by the probe energy. The < 75 fs timescale derived previously has defined the time taken for the wavepacket to lose overlap with the accessible ion states and leave the initially populated Frank-Condon region.[77] The longer timescales provided by this experiment more closely match those obtained in recent time and energy resolved ion yield measurements on the same vibrational state of ammonia.[79,99] In the ion kinetic energy release work the appearance times of the hydrogen atom is resolved into various kinetic energy regions correlating with adiabatic and non-adiabatic dissociation processes. The kinetic model proposed broadly separated the dissociation trajectories in two; one centred on more planar geometries at the Frank-Condon region which lead to non-adiabatic dissociation and the formation of the ground state products; a second set of trajectories coming from non-planar geometries leading to the formation of adiabatic dissociation products. Both sets of trajectories left the Frank-Condon region

and moved towards the conical intersection located at the extended H-NH_2 bond lengths on a timescale of 100 fs. Once in the region of the conical intersection, the trajectories originating from planar geometries were seen to relax through the conical intersection within 70 fs, leading to a rapid formation of ground state products through a non-adiabatic process. Conversely, the trajectories originating from non-planar geometries were seen to have an extended lifetime in the region of the conical intersection, leading to a delayed appearance of the adiabatic dissociation products. The delayed appearance allowed for a lifetime of the population in the region of the conical intersection to be derived which was on the order of 400 fs.[99]

The timescales derived from the photoion kinetic energy release measurements are therefore at odds with previous photoelectron spectroscopy measurements and slightly longer than those measured in our experiment.[99] As mentioned above, the difference lies in the measurement process and what part of the full dynamics is being measured. Based on the timescales the resonant multiphoton probe is sensitive to an extended region of the excited state potential energy surface, but is not sensitive to the final dissociation product formation. The difference in lifetimes obtained for the various vibrational states are a consequence of the resonant ionisation process.

Rydberg states are in general very similar in shape to the ion states to which they converge. Rydberg states therefore have a very strong $\delta V = 0$ transition propensity which gives rise to extremely sharp lines in their photoelectron spectra. This is a key property in the use of Rydberg fingerprint spectroscopy experiments, where often the use of superexcited and Rydberg states provides detailed information about static and dynamics structure.[108,109] The situation in the E′ state is slightly more complex, however the changes in the observed photoelectron spectrum can still be related back to the dynamics in the $\tilde{A}$-state. The change in vibrational levels seen in the time dependent photoelectron spectrum is related to which vibrational levels of the Rydberg state are accessed after the absorption of a single probe photon and can be rationalised as follows with reference to figure 5.6. At early times, absorption of a single 400 nm photon populates a particular set of vibrational levels in the E′ Rydberg state. The dominant level populated leads to the photoelectron spectrum obtained at early times, peaking

at the $\nu_1^2\nu_2^1$ level. As the wavepacket propagates on the $\tilde{A}$-state towards the conical intersection and dissociation, the various trajectories lead to changes in the dominate transition into the E′ Rydberg state. Changes in the transition probability into the Rydberg state then manifest in the photoelectron spectrum.

The higher vibrational levels associated with the symmetric stretch show a shorter lifetime. We associate this lifetime with the non-adiabatic dissociation process which, from our measurements, proves an average lifetime around 200 fs. This closely matches the average lifetimes were associated with different levels of vibrational excitation in the NH_2 fragment, with the majority of the signal seen at higher levels of vibrational excitation correlating with the longer lifetime. The 200 fs lifetime obtained from out photoelectron spectroscopy measurements would provide an average of these numbers and therefore correlates well with the excited state lifetime suggested from ion kinetic energy release measurements. With the current data we cannot correlate the vibrational levels in the photoelectron spectrum with the associated levels of vibrational excitation in the resulting NH_2 fragment. This may be possible in a more resolved spectrum or if calculations of the intermediate Rydberg state can provide insight into the resonance condition for the excitation and ionisation process. The non-adiabatic dissociation process is thought to predominantly originate from planar geometries whose trajectories we suggest, maintain overlap with higher vibrational levels in the E′ Rydberg state out to the region of the conical intersection.

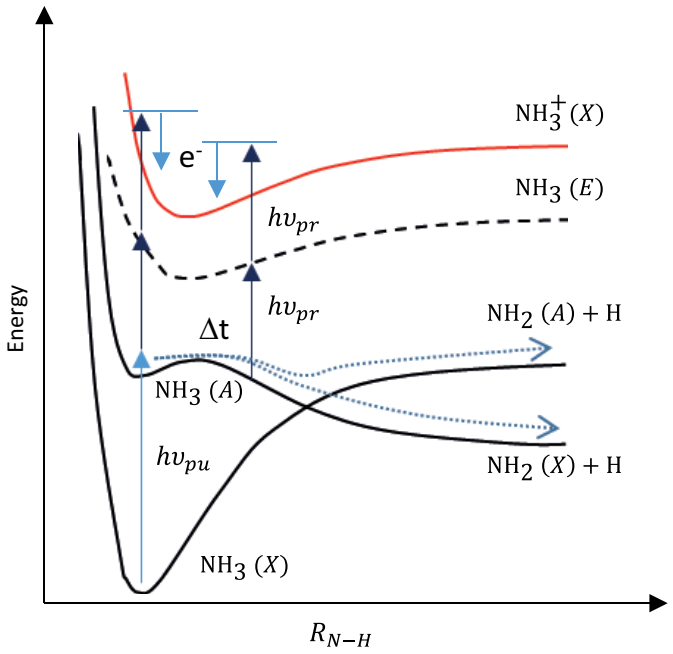

FIGURE 5.6: Schematic representation of the potentials of ammonia of relevence to the experiment. A single UV photon at 200 nm, $h\nu_{pu}$, excites the ν_2=4 vibrational level of the $\tilde{A}$-state. Absorpion of a single 400 nm photon, $h\nu_{pr}$ populates vibrational levels of the E' Rydberg state. At early times the dominant transition into the E' Rydberg state leads to population of the ν_1=2 vibrational level of the ion state upon absorption of a second 400 nm photon. After approximately 100 fs the wavepacket is localised in the region of the conical intersection where different trajectories to the adiabatic and non-adiabatic dissociation products give rise to different levels of vibrational excitation in the E' Rydberg state. These manifest as changes in the vibrational lifetimes of the measured ion states accessed following the absorption of a second 400 nm photon.

The lower vibrational states observed in the photoelectron spectrum have a much longer lifetime of over 300 fs. This is longer than the lifetime associated with non-adiabatic dissociation and more closely matches the lifetime associated with adiabatic dissociation into an electronically excited NH_2 fragment in conjunction with H. The adiabatic dissociation products are considered to be formed by trajectories originating from non-planar geometries in the $\tilde{A}$-state. These maybe expected to follow a less direct trajectory towards the conical intersection and dissociation such that lower levels of the stretching vibration are observed. The 300 fs lifetime is someway short of the lifetime retrieved from ion kinetic energy release measurements, however, the photoelectron spectroscopy experiments will only be sensitive to regions where the probe photon remains resonant.

While this will extend some distance along the excited state potential it is unlikely to extend beyond the region of the conical intersection. As the trajectory may be less direct this could explain the relatively short lifetime obtained when compared with the time at which the fully dissociated products are formed.

5.4 Conclusions

The photodissociation dynamics of ammonia in the ν_2^4 vibrational level of the $\tilde{A}$-state have been studied using a resonant multiphoton ionisation probe in a photoelectron spectroscopy experiment. By probing the dynamics via the intermediate E' Rydberg state we access a different set of vibrational levels in the ion and maintain overlap with the ion state for an extended period of time. By maintaining the overlap with the ion state without requiring a high energy probe, the observation window is maximised without the problems associated with DUV or XUV probes, maintaining a low background signal and clear early time dynamics. The dynamics in the $\tilde{A}$-state manifest as changes in the vibrational transition into the Rydberg state which show up in the measurement as vibrational state dependent lifetimes. Higher lying ion vibrational states have an average excited state lifetime of approximately 200 fs which closely matches the lifetime associated with the non-adiabatic dissociation process while the lower vibrational states have a much longer lifetime of over 300 fs which more closely matches the adiabatic dissociation process. The different trajectories taken by the two competing dissociation pathways at the region of the conical intersection show up different excitation and ionisation propensity allowing us to isolate features related to each process.

Chapter 6

XUV Photoelectron Spectroscopy of Carbon Disulphide

The work presented in this chapter is based on publication Smith et al. Phys. Rev. Lett. **120**, 183003, 2018 that has been submitted, the work has been carried out at Artemis in the Central Laser Facility, UK. The theoretical work presented in this section is carried out by the Kirrander group, University of Edinburgh.

6.1 Introduction

Despite the simplicity of the CS_2 molecule, a clear picture of the dynamics and a full explanation for time scales and product branching ratios remains elusive for the photo chemistry of this molecule. The simplicity of CS_2 arises from the small nature of the molecule but like larger systems, its photochemistry involves many different states making its dynamics complex. It includes a high number of near degenerate electronic states, rapid internal conversion, and inter-system crossing dynamics, with the latter two processes correlating strongly with vibrational dynamics.[110–117] In CS_2 different dissociation products are formed with either singlet or triplet spin states of the dissociated S atom, due to competing processes within the molecule. Despite how fast the dissociation process is (< 1 ps) extensive experiments have shown that the spin forbidden triplet state

product dominates the dissociation yield.[118–121] For this reaction explaining the mechanism for this outcome is non-trivial. Experimental techniques that are able to provide the required sensitivity to the electronic and nuclear dynamics rarely measure the full reaction pathway. Leading to the partial measurements of the mechanism and henceforth vital steps in the mechanism could have been missed.

The dynamics of CS_2 have been widely studied, in both the time and frequency domains. In previous work Stolow and co-workers used molecular alignment in combination with UV photoelectron imaging to measure the early time dynamics. The corrolated changes in electronic structure and molecular geometry highlight the importance of the initial internal conversion process.[111,112]The combination of both photoelectron images and alignment show new insight into the valence shell electrons as the photodissciation reaction progress. However they are still unable to measure the whole reaction co-ordinate. More recent measurements by Horio et al. mapped the the bending vibrational motion during early time dynamics and the large ionisation potential change associated with this vibrational motion.[114,115]They observed the appearance of the singlet dissociation products through a resonance with the auto-ionising states of the S atom produced using a 9.3 eV probe.[117] The observation of the singlet product was coincidental due to resonance with the probe, however the observation is short lived. Even by using a high energy probe, observing the dynamics in the dominant triplet state dissociation could not be done and the singlet dissociation mechanism was challenging to define. Extensive experiments also monitored the angular and velocity distributions of the products[120,122,123] and provided branching ratios for the triplet to singlet dissociation channels of around 3:1 (however estimates over the years have varied from 0.25:1 to 6:1[118–121 124–127] but, importantly, the experiments have provided few explanations for why the spin forbidden product dominates the dissociation yield.

Using a table-top femtosecond XUV pulse from a high harmonic generation source as a probe for photoelectron spectroscopy, our experiments aimed to measure a complete reaction pathway in full detail. This has allowed us to identify the most important electronic and structural transformation associated with the CS_2. The energy of the XUV probe allow us to ionise and measure all of the relevant electronic states present

within the complete reaction co-ordinate. A cartoon representation of these states can be seen in figure 6.1.

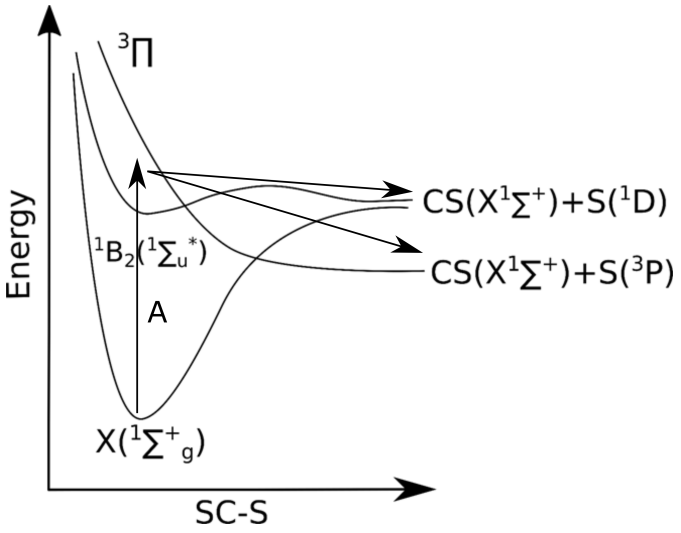

FIGURE 6.1: A schematic potential energy surface of the dissociation dynamics of CS_2, A is the absorption of a photon into the singlet excited state. Following initial excitation this leads to the dissociation, resulting in the formation of S(^{1}D) singlet and S(^{3}S) triplet following intersystem crossing, the cartoon representation is adapted from Hu, et al.[1]

6.2 Experimental

A brief overview of the experimental is provided. Following on from this a guide as to how the experiment was set-up with the details to the process. For a full description of the beamline please refer back to the details provided in 2.3. The experiments were performed at the Artemis laser facility at the Rutherford Appleton Laboratories. The laser system consists of amplified femtosecond laser system (Red Dragon, KM labs) generating 30 fs duration pulses at a central wavelength of 800 nm. The output of the laser is split into two parts before compression allowing for independent optimisation of the chirp, duration and pulse energy of the pulses used to generate the pump and probe. The pump is generated from the 5 mJ output of compressor 2 which is frequency doubled in BBO followed by two stages of sum frequency generation (SFG). The first SFG stage generates 266 nm light through mixing the fundamental 800 nm with the second harmonic at 400 nm in a type II process in BBO. The second SFG stage mixes

the 266 nm light with a previously separated 800 nm beam to generate the pump at 200 nm with a controllable pulse energy of up to 2 μJ. For the experiments described in this work the pulse energy is kept to 1 μJ. The probe is generated via high harmonic generation. The 4 mJ output of compressor 1 is frequency doubled in BBO generating 0.5 mJ at 400 nm. The 400 nm light is separated from the residual 800 nm beam and focussed into a gas jet of Ar. The resulting harmonics are monochromated at a time preserving monochromator.[65] The 7th harmonic at 21.5 eV is selected and focussed into the centre of the interaction region of a time of flight photoelectron spectrometer with an on target flux of approximately 1×10^{10} photons per second. The pump beam is focussed into the interaction region of a commercial Time of Flight (ToF) spectrometer (Kaesdorf ETF11) with a 1 m focal length mirror where it is crossed at a small angle (3°) by the probe. The pump and probe beams have linear polarisation in the plane of the time of flight axis and have a temporal cross-correlation of 180 fs (FWHM). The 200 nm (6.2 eV) pump pulse excites CS_2 from the ground state mostly into the S_2 (B $^1B_2$ / $^1\Sigma_u^+$) excited state at time zero. Following this the molecule evolves the excited state potential surfaces leading to dissociation. The dynamic processes are then probed using a 21.6 eV probe at various time delays, which leads to a time resolve photoelectron spectrum. The CS_2 molecular beam is generated by the expansion of a 2 % CS_2 in He mixture through a pulsed nozzle operating at 1 kHz (Amsterdam Cantelever).[66] The resulting molecular beam is skimmed before entering the measurements chamber. The relative delay between the pump and probe pulses is controlled by a mechanical translation stage with delays between -2 – 10 ps. This range is covered with varying time steps. To correct for any long term fluctuations in power, the stage is through the progression of the delays multiple times. For each time step within a cycle we collect a spectrum for 1 second which corresponds to 1000 laser pulses. We cycle through the time steps 650 times to give a total data collection time of approximately 13 hours per delay scan.

6.2.1 A guide as to how to carry out a time resolved photoelectron spectroscopy measurement with an XUV probe

The beamline that was used for this experiment can be seen in figure 2.8. The first step in this experiment was to assemble the beamline. Each arm of the experiment will be discussed in turn, including the optimisation process at each step. For the probe arm of the experiment distance before the first compressor needed to be included so that the beam paths were of equal length. Once the probe beam path had been adjusted to approximately the same length as the pump arm of the experiment, the beam was passed into the compressor. After the compressor we performed second harmonic generation in order to produce 400 nm from the fundamental 800 nm beam. The second harmonic generation process was optimised here. This was conducted by adjusting the crystal angle and the rotation of the crystal in the mount in order to obtain maximum conversion efficiency in the BBO. In order to measure the amount of second harmonic that is being generated and to remove the fundamental beam from the experiment harmonic separators were used which transmit the fundamental beam whilst reflecting the second harmonic. The second harmonic then enters the XUV generation chamber. When the beam is in the chamber it is reflection focused into the gas cell using a 20 cm focal length mirror. The beam was aligned so that it was flat and straight throughout the whole beamline and that the focal position was in the centre of the gas cell. Once the XUV chamber had been pumped down, high harmonic generation was performed with argon being used as the generation medium. Harmonic flux is critical in these experiments because it leads to shorter collection times and an improved signal to noise ratio. Harmonic flux must be optimised and in order to do this the CEM was used to monitor the flux at a particular harmonic peak. There are several steps here; firstly the phase-matching into the gas cell had to be optimised. This was done by moving the gas cell position in the X, Y and Z dimensions, as it was mounted on movable stages. The pressure in the gas cell can be adjusted in order to maximise harmonic flux and once the generation conditions are optimised the grating angle in the monochromator can be adjusted so that a maximum of a particular harmonic can be isolated. Following this, the slit width on the exit of the monochromator can also be adjusted. This was

generally set as wide as possible whilst maintaining isolation of a single harmonic. The isolated harmonic beam was then focused into the interaction region of the end station using the toroidal mirror.

The next step was to assemble the pump are of the experiment. The delay stage must be set so that the beam is flat and straight as it moves from one end to the other, if this is not the case overlap will be lost as this is adjusted to control the time step of the experiment. Fourth harmonic generation is then set-up, as seen in figure 2.7 and this required optimisation before data could be collected. As previously discussed in chapter 2.3.2.1 this is done by adjusting the angle of the crystals and the timing of the final overlap in the fourth harmonic generation crystal. Once the fourth harmonic has been generated it is isolated once again using a series of reflections on harmonic separators. The isolated forth harmonic is then refection focused using a 150 cm focal length mirror, before it enters into the toroidal mirror chamber where it is bounced off a D-shaped mirror in order to reach the interaction region. The overlap of both the pump and probe beams at the interaction region is critical because the focused probe beam is considerably smaller than the focused pump beam. Spatial overlap of the pump and probe beams was checked using a (LuAG:Ce) phosphorescent crystal which is mounted on a mechanical arm, that can be moved by hand. The phosphorescence from the crystal was imaged using a CCD camera. The crystal was mounted such that it sat in the centre of the interaction region. The harmonic beam is imaged first and its position adjusted such that it is centred on the crystal by moving the toroidal mirror which is mounted on motorised stages. The position of the phosphorescence was then marked on the screen and the centre of mass of the pump beam is placed on top of this point. This is achieved by adjusting the D-shaped mirror which is also controllable in X and Y, allowing the beam to be moved into place. The focal position of the pump beam could also be optimised by adjusting the position of the focusing mirror, this was placed on a translation stage, in order to get the tightest focus of the pump beam at the interaction region.

Once Spatial overlap had been established between the two beams of the experiment,

temporal overlap needed to be located. Temporal overlap is non-trivial to achieve especially with the XUV. In order to get a guide as to where time zero was, a fast photodiode was used to make measurements of the time at which each pulse arrived at the back end of the chamber. This process ensured that time zero was at least within the delay stages length. By making these measurements we usually ended up within a few millimetres of time zero, this distance is on the order of picoseconds in terms of time. Once time zero was found within this range a scan using the pump beam and the zero order probe beam (400 nm, this can pass through the monochromator as long as the slit is opened wide to prevent damage) was performed in CS_2. In this molecule there is a large signal at time zero due to multiphoton ionisation. Once time zero has been found using the zero order beam, a scan was set up with the XUV using an isolated harmonic. The isolated harmonic that was chosen was the one with maximum flux between 16 and 21 eV. The 21 eV harmonic had approximately a third again more flux on the CEM (10^{10} photons/second in the 21 eV harmonic) so this was used for the measurement. A simple scan was then set-up which went from one side of the time zero position that was found previously, using the zero order probe, to the other in order to determine if the photo-dissociation was occurring from molecular CS_2 to the molecular CS plus S. If dissociation is occurring a new peak will be observed at 12 eV due to molecular S. Once this is observed scans with more steps were used to find the precise position of time zero, initially steps of 1 ps were used and these became incrementally smaller around the area over which the dissociation was initially observed. For example, if the molecular S peak was observed first, at + 6 ps from time zero, we would move time zero to that position and then make 500 fs steps and incrementally smaller steps, in order to find the exact time overlap.

To extract the data the TDC values need to be calibrated to actual time of flight, which is then converted to energy. This was done using the peak from photons directly hitting the detector and the known values for the ground state ionisation potentials of CS_2 which are 10.06, 12.69 and 14.47 eV. The time space between the ground peaks was correct so when this was converted to energy only the zero offset had to be accounted for this was done by subtracting the photon peak time from all the TDC values. The TDC values given in time were then converted to energy using $E_{binding} = E_{photon} - 0.5 * m * (d/t)^2$.

Where d is the distance of the drift, t is TDC time E_photon is the energy of the XUV probe. The intensities were then multiplied by a Jacobian $1/t^3$ factor. The values for d and E_{photon} were calibrated using the CS_2 ground state peaks.

6.3 Results and Discussion

In figure 6.2 we plot the ground state CS_2 spectrum obtained at a time long before the arrival of the pump pulse. The energy axis is the difference between the probe photon energy and the measured electron kinetic energy and corresponds to the binding energy of the electron to the state being ionised. The peaks in the spectrum are due to ionisation of the ground state into different ion states. The ground state $\chi\Pi_g$ and the excited states $\tilde{A}^2\Pi_u$ and $\tilde{B}^2\Sigma_u^+$ of the ion at binding energies of 10.06, 12.7 and 14.5 eV respectively. This spectrum is taken as the background and is subtracted from all spectra obtained at later times providing a background subtracted spectrum. Two background subtracted spectra are plotted within the same figure. The spectra are the average spectra obtained between 100-600 fs and 4.1-10 ps. The dynamics in CS_2 are predominantly over by 4.1 ps so this is considered to be asymptotically long and shows the spectrum obtained once the dynamics are complete. Here we can see both positive and negative features, positive features correspond to an enhancement and negative features to a depletion. In the spectra from 4.1-10 ps we see a strong depletion of the peaks associated with the ground state spectrum of CS_2 as well as several new features associated with the multiple dissociation products. Based on the amount of depletion observed we estimate that approximately 2% of the ground state population is excited in the experiment, the amount of depletion whilst large relative to the formation of the dissociated products is still relatively small compared to the total amount of CS_2 used throughout the experiment. We observe peaks associated with ionisation of the ground state CS ($\chi^1\Sigma^+$) fragment in conjunction with both ground (^{3}P) and excited state (^{1}D) sulphur atoms which are labelled by combs in the figure based on known ionisation potentials. At early times we have features at lower binding energies that are much lower in intensity due to the small ionisation cross section of the excited states of the bound CS_2 molecule. The labels marking the assignments for these features do not have

well defined energies, the width of the comb therefore corresponds to the energy region taken in the kinetic fits described later. The singlet state has been previously studied and is known to cover an energy spread around 3 eV.[115]

The features in the spectrum are assigned based on known ionisation limits and previous frequency resolved photoelectron spectroscopy measurements taken with He I radiation sources. The ground state CS_2 spectrum is assigned based on the work of Turner.[2] The assignment of the excited singlet states of CS_2 matches that expected energetically and agrees with previous assignments.[114–116] To the best of our knowledge, the excited triplet state has not been previously measured. The assignment is based on the expected energy for ionisation into the first excited state of the ion. The dynamic of the signal is in line with the kinetics of the triplet dissociation process and with the expected time dependence from the surface hopping calculations. To assign the sulphur features we compare the features observed to those made by L. Zuin et al. previously[128] for ionisation of the ^{3}P state and M. Barthel et al. previous measurements for comparison with ^{1}D state.[129] Ionisation of ground state ^{3}P sulphur atoms is into the ground, ^{4}S, and excited ion states, ^{2}D and ^{2}P, at 10.4 eV, 12.2 eV and 13.4 eV respectively with the largest cross section into the ^{2}D state at 12.2 eV in agreement with those measured previously.[128] A direct comparison of the ionisation cross section for the metastable ^{1}D is not available with no measurements at a comparable wavelength. The features associated with ionisation of the excited state S(^{1}D) atoms leads to population of the excited ion states, ^{2}D and ^{2}P, at 11.0 eV and 12.2 eV. The assignment is based on known ionisation limits with ionisation of the ^{1}D product into the ground ion state not observed due to the spin forbidden nature of this transition. The assignment of features of the CS fragment was based on previous work by N. Jonathan et al.[130] In this work an electrical discharge has been used to drive the dissociation of CS_2 molecule with the CS products measured by photolysis with a helium lamp.

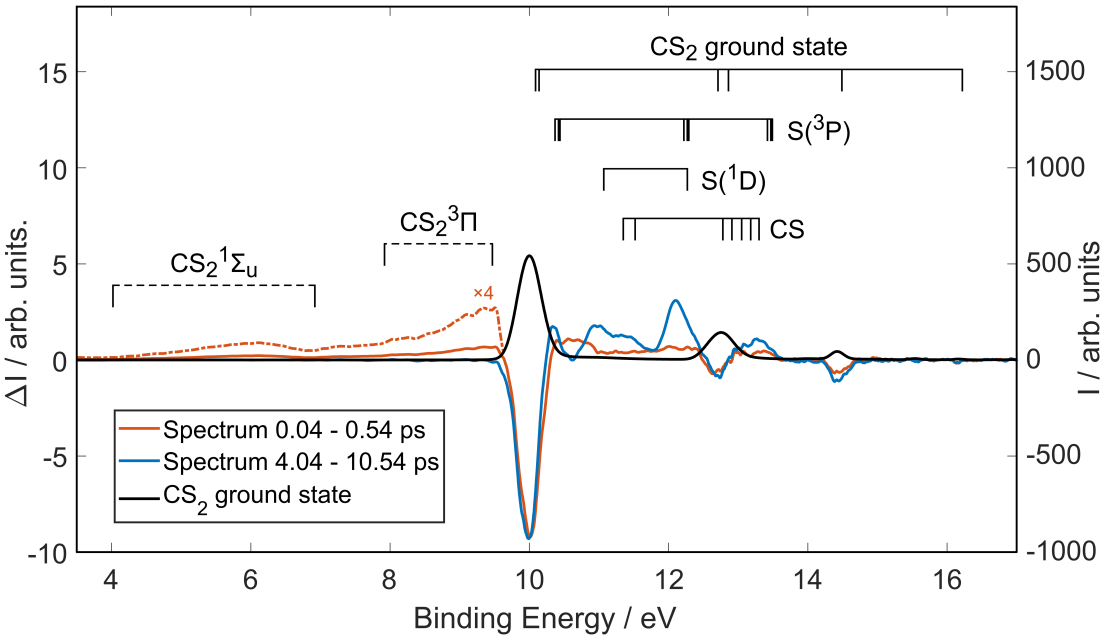

FIGURE 6.2: Assigned photoelectron spectra for the different bands that have been measured. The ground state spectrum is the black line, plotted on the right hand axis. The ground state spectrum highlights the position of the features associated with the ground sate population and is the background spectrum. Both the red and blue line spectra are background subtracted, the black line. The red line is the average of the early time spectrum from 0.1 - 0.6 ps and the blue line is the average late time spectrum 4.1 - 10.6 ps. The times are times after the pump beam, 200 nm (6.2 eV). Negative features in the spectrum are from the reduction in signal and correspond to a reduction in the ground state population with positive features showing new bands in the photoelectron spectrum. The combs above the peaks show the assignments based on the known ionisation energies of the produces fragments.

Time dependent changes in the background-subtracted photoelectron spectrum over the full range of energies measured are plotted as a false colour surface plot in figure 6.3. These plots are separated into two energy ranges that cover different parts of the dynamics. Below 10 eV we measure signal that is due to the excited state population in the bound CS_2 molecule which has a correspondingly low binding energy. The final products all have ionisation potentials above 10 eV and this section therefore provides information on the appearance of the dissociation products. Examining these plots, we observe that initial excitation leads to a depletion of bands associated with the

ground state CS_2 molecules as well as a proportional increase in signal associated with population of the excited singlet state. Ionisation of the excited singlet state is expected to dominantly populate the ground ion state of the molecule giving a photoelectron band starting at 4 eV. The photoelectron band stretches between 4-7 eV due to large changes in the ionisation potential associated with the CS_2 bending motion. This 3 eV change in the photoelectron energy has previously been observed with an 8 eV filamentation source. The damping of the vibrational motion leads to the triangular shape of the band over the few hundred femtoseconds in which significant population remains within the excited singlet state. Previous work has shown that there is a clear bending motion in S-C-S at early times. The bending motion has been observed experimentally.[115] This motion leads to a distinctive shape in the singlet excited state feature. The motion occurs on a quick timescale (the bending period is approximately 80 fs) and therefore a clear observation of the bend requires a very short cross correlation time, ours from the experimental fits is around 180 fs. As the singlet state population decays we observe a new band at binding energies 7-10 eV. We assign this signal to population in the triplet state following inter-system crossing. The band maximum is seen to shift to higher binding energies as the molecule dissociates eventually reaching the asymptotic values associated with the ground state CS and S(^{3}P) products. As well as the features associated with the ground state we resolve the S(^{1}D) products that form from the direct dissociation in the singlet excited states. The strongest and clearest product signal is observed at 12.4 eV and contains contributions from both the singlet and triplet dissociation products. Previous He 1 photoelectron spectroscopy experiments have shown this to be the dominant ionising transition at these wavelengths for the ^{3}P states of S.

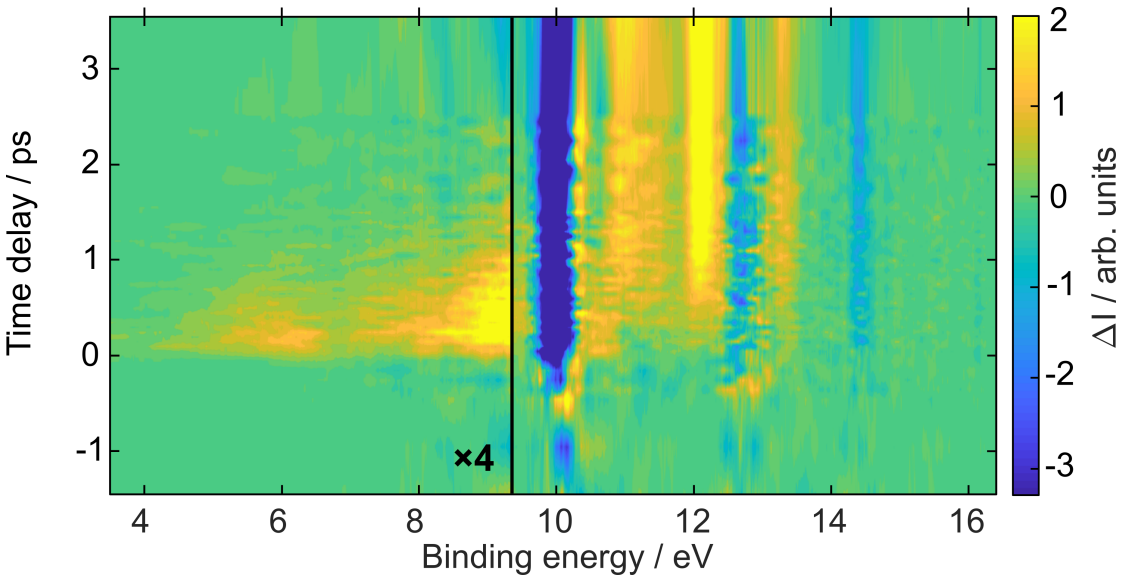

FIGURE 6.3: A figure showing a false colour surface map showing the changes in the photoelectron spectrum as a function of pump-probe time delay, positive times the pump pulse is first followed by the XUV pulse.

To highlight the changes in the photoelectron spectrum we select regions of the spectrum that correlate with specific transient states in the dynamic process. In Figure 6.5 we plot the photoelectron intensity in the regions between 9.8 – 10.1 eV, 4.0 – 6.9 eV, 7.9 – 9.1 eV and 11.9 – 12.3 eV that correlate with population in the ground state, singlet excited state, triplet excited state and dissociation products. The ground state, singlet excited state, triplet excited state and dissociation products can be fitted to a kinetic model that allows us to extract effective lifetimes for each of the regions assuming first order kinetic processes are occurring. The kinetic model used to obtain the excited state lifetimes breaks down the dynamics into 5 distinct regions. Absorption of a photon transfers population from the ground state, $CS_2(X)$, into the excited singlet states, $CS_2(S)$. The $CS_2(S)$ population decays into the excited triplet states, $CS_2(T)$ leading to the formation of triplet dissociation products, $S(^3P)$. The population that does not transfer into the triplet states dissociates forming singlet, $S(^1D)$. The singlet and triplet dissociation pathways form parallel competing reactions can be seen in figure 6.4.

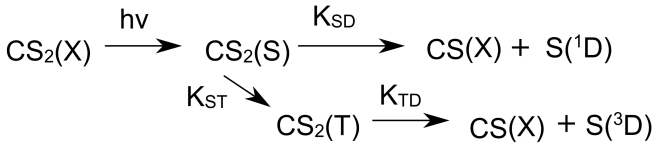

FIGURE 6.4: A scheme showing the kinetic model used for extracting lifetimes from the experimental data.

K_{SD} and K_{ST} gives the decay rates of the initially excited singlet state into the singlet dissociation channel and into the excited triplet state respectively. The total decay rate of the excited state is therefore given by $K_s = K_{SD} + K_{ST}$. K_{TD} defines the decay rate of the triplet state to the dissociated products and $h\nu$ defines the laser pulse parameters.

By applying the model the dynamics can be viewed as two distinct channels, for the five different chemical species involved. the equations used for each channel define the time-dependent intensity of the regions, which includes a convolution with the instrument response function which is defined by the laser cross-correlation. The kinetic model sets a series of equations that define the time dependent populations used for fitting.

Ground state population

$$I = -A_0 \left[1 + \mathrm{erf}\left(\frac{\Delta t}{\sqrt{2}\sigma}\right)\right]$$

CS_2 singlet excited state population

$$I = Ae^{-K_S \Delta t} \left[1 + \mathrm{erf}\left(\frac{\Delta t - \sigma^2 K_S}{\sqrt{2}\sigma}\right)\right]$$

CS_2 triplet excited state population

$$I = B_1 \left(e^{-K_{TD}\Delta t} e^{\frac{(\sigma K_{TD})^2}{2}} \left[1 + \mathrm{erf}\left(\frac{\Delta t - \sigma^2 K_{TD}}{\sqrt{2}\sigma}\right)\right] - e^{-K_S \Delta t} e^{\frac{(\sigma K_S)^2}{2}} \left[1 + \mathrm{erf}\left(\frac{\Delta t - \sigma^2 K_S}{\sqrt{2}\sigma}\right)\right]\right)$$

Dissociated CS & S singlet population

$$I = B_2 \left(\left[1 + \mathrm{erf}\left(\frac{\Delta t}{\sqrt{2}\sigma}\right)\right] - e^{-K_S \Delta t} e^{\frac{(\sigma K_s)^2}{2}} \left[1 + \mathrm{erf}\left(\frac{\Delta t - \sigma^2 K_s}{\sqrt{2}\sigma}\right)\right]\right)$$

Dissociated CS & S triplet states population

$$I = C\left(\frac{K_S - k_{TD}}{K_s k_{TD}}\left[1+\mathrm{erf}\left(\frac{\Delta t}{\sqrt{2}\sigma}\right)\right] - e^{-k_{TD}\Delta t}e^{\frac{(\sigma k_{TD})^2}{2}}\left[1+\mathrm{erf}\left(\frac{\Delta t-\sigma k_{TD}}{\sqrt{2}\sigma}\right)\right]\right.$$
$$\left.+e^{-K_s\Delta t}e^{\frac{(\sigma K_s)^2}{2}}\left[1+\mathrm{erf}\left(\frac{\Delta t-\sigma k_S}{\sqrt{2}\sigma}\right)\right]\right)$$

A, B and C are fitted amplitude that account for the changing ionisation cross sections and detection efficiencies of the various chemical species, σ is the standard deviation of the Gaussian which defines the laser cross-correlation, t is the pump-probe delay, erf is the error function, and all other terms have the same defined in the reaction scheme above. Within this model, separation of k_{SD} and k_{ST} is not possible from measurements of the decay rates alone. If the kinetic model accurately defines all the individual processes the ratio of values of k_{SD} and k_{ST} would define the branching ratio however this is not the case for the singlet dissociation process.

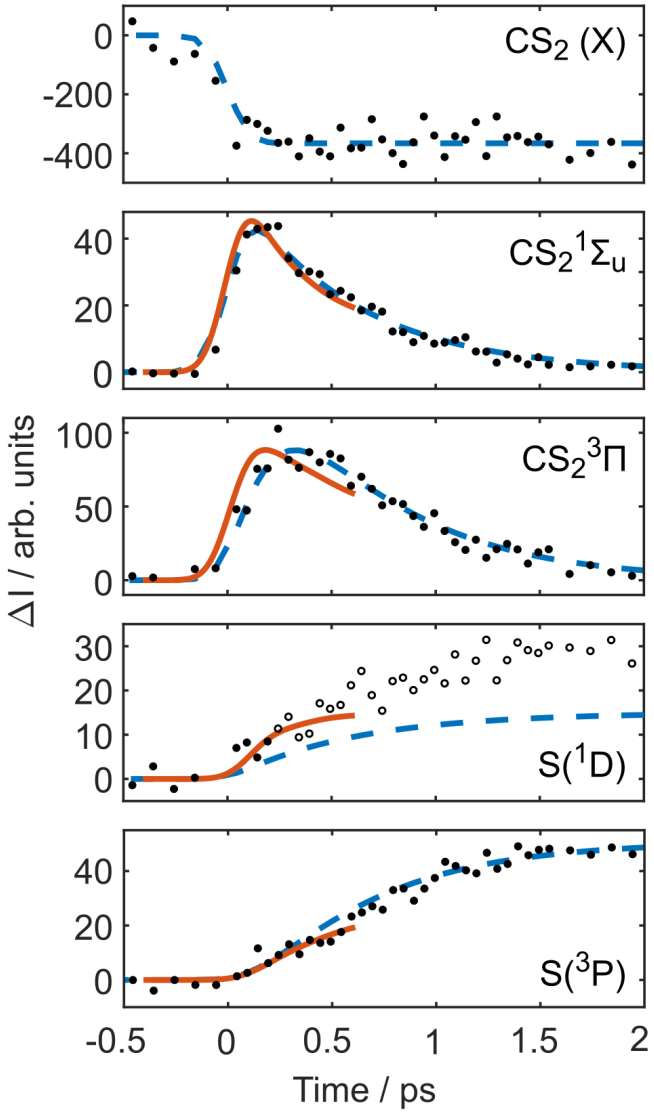

FIGURE 6.5: Time dependent plots for the corresponding to the ground state population, the excited singlet state population, the excited triplet state population, the S(^{1}D) dissociation product and the S(^{3}D) dissociation product. The dashed lines in the plot represent the fits to the data that are based on the kinetic model. The solid lines are from surface hoping calculations performed by the Kirrander group, University of Edinburgh.

In order to highlight the changes in the photoelectron spectrum, we plotted the integrated electron count over energy regions that correlate with specific states in the dynamic process in figure 6.5. The regions selected covered the 9.8 – 10.1 eV, 4.0 – 6.9 eV, 7.9 – 9.4 eV, 12.1 – 12.2 eV, and 12.25 – 12.33 eV energy ranges, which correlate with population in the ground state (CS_2(X)), singlet excited states ($CS_2(^1\Sigma)$), triplet excited

states ($CS_2(^3\Pi)$), singlet dissociation product ($S(^1D)$) and triplet dissociation product ($S(^3P)$) respectively. The analysis of the features associated with dissociated population was complicated by the density of the spectrum and by the features associated with transient structures.

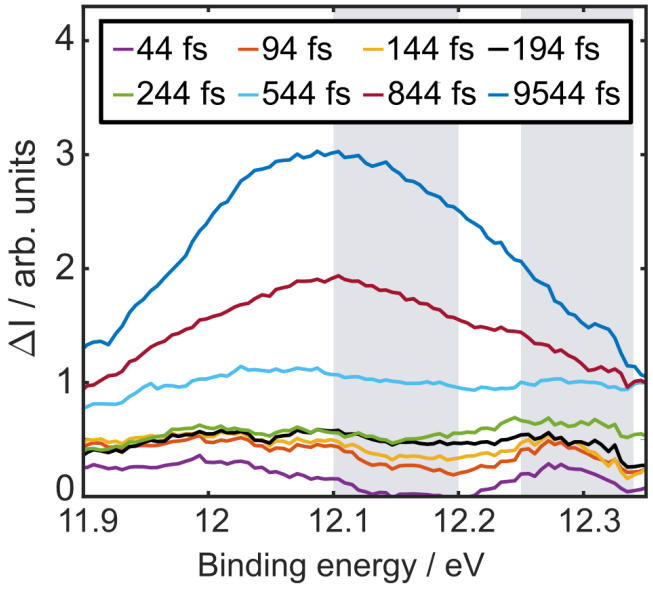

FIGURE 6.6: An expanded view of the photoelectron spectrum in the region covered by the two dissociation products. The regions highlighted cover those used for the $S(^1D)$ and $S(^3P)$ fits respectively. Showing at early times the single is dominated by the singlet, but after a few 100 fs triplet dominates.

An expanded view of the photoelectron spectrum over the region 11.9 – 12.35 eV associated with the atomic S signal used in figure 6.5 and at various times after excitation is shown in figure 6.6. Based on the known ionisation limits of the S atom in this energy region, we expect signals relating to the $S+(^2P) \leftarrow S(^1D)$ and $S+(^2D) \leftarrow S(^3P)$ ionising transition at 12.26 eV and between 12.1 – 12.2 eV respectively.We see a rapid increase in the $S(^1D)$ signal at 12.26 eV at early times (< 200 fs) and this is the major feature in the spectrum. There is also significant intensity at energies below 12.1 eV which is seen to shift to higher energies as a function of time. As the time delay increases the maximum of the lower energy feature shifts to energies associated with the $S(^3P)$ product. These eventually dominate the spectrum including in the region of the spectrum initially dominated by the $S(^1D)$ signal. A measure of the $S(^3P)$ and $S(^1D)$ yields can be obtained by integrating over the energy windows highlighted in figure 6.6. The trace obtained for the

$S(^1D)$ is dominated by signal linked to the $S(^3P)$ product at long times. Therefore it is only reliable for the first 200-250 fs following excitation because the $S(^3P)$ yield remains small. The integrated electron count in the highlighted regions are plotted in figure 6.5. The data points for the $S(^1D)$ channel that are reliable are plotted as solid symbols and those that have a significant contribution from the $S(^3P)$ are represented by hollow symbols. The plots therefore quantitatively measure the $S(^3P)$ yield and a qualitatively measure the time dependence of the production of the $S(^1D)$ fragments. Based on the changes in the spectrum and in the integrated yields, the singlet fragment appears to be produced more rapidly than the triplet, but with a much lower yield. After the initial formation, we observe no measurable increase in the singlet dissociation products despite significant population remaining in the excited singlet states for several hundred femtosecond after the initial rise. The fits we obtained provided an effective excited state lifetime of 570 fs for the singlet excited state. This correlates with the rising triplet state population and a lifetime of 170 fs for the triplet state which correlates with the appearance of the $S(^3P)$ dissociation products. The delayed appearance of features between 7.9 – 9.4 eV and their correlation with the formation of the atomic triplet state product, confirms the earlier assignment of the states. The significant intensity in the singlet dissociation products early on (100 fs) appears as a step and does not correlate with the singlet or triplet state populations or effective lifetimes. This suggests the singlet states are stabilised from further dissociation after the first few hundred femtoseconds.

Full dimensional surface hoping calculations were performed by collaborators from the Kirrander group, University of Edinburgh. There calculations accounted for internal conversion and inter-system crossing. The theory work was based on ab initio calculations, the comparison between the theoretical calculations and experimental can be seen in figure 6.5, with the solid line showing the theoretical work. The theory shows strong agreement with the experiment in both lifetimes and branching ratios and can aid in the full understanding of the molecular dynamics.

6.4 Conclusions

Experimentally we have demonstrated that by using an XUV probe in photoelectron spectroscopy we are able to map the complete reaction co-ordinate for CS_2. Whilst during the early time dynamics the bending motion has not been captured such that it is well defined. The shape of the photoelectron band matches closely to the work that has been performed by Suzuki, who mapped the early time dynamics extremely clearly using a 9 eV probe. By having additional probe energy available to use we are able to make full observations of the singlet state. The lifetimes for different states have been extracted from the experimental data however, the kinetic model breaks down due to the step that is observed within the singlet sulphur band at early times, meaning that this does not fit the model.

Our theoretical collaborators have shown that experimental data and theoretical data can match with a high degree of accuracy. By having high level theoretical calculations that match experimental data new information for the mechanism of dissociation for a particular molecule can be obtained. Enabling both experimentalists and theoreticians to work together to provide a full description of the molecular dynamics. The theoretical work that has been performed has concluded that the branching ratio between singlet and triplet products is controlled by spin-orbit coupling, as well as the extremely fast non-adiabatic dynamics in the numerous singlet states that are accessible.

Providing an experimental probe that can capture all reaction intermediates in this simple system has led to conclusions that there is more complex motion in the electronic and nuclear dynamics than previously observed. By monitoring all aspects of the reaction a full mechanism can be provided in conjunction with theoretical work. Whilst performing this type of measurement on larger systems will be challenging, due to the increased complexity of the photoelectron spectrum and the increased background on the measurements, it is expected that other features that have been hidden to date will provide new insight into the true mechanism of dissociation.

Chapter 7

Summary

In chapter 3 the development of a high harmonic spectroscopy experiment in Southampton has been shown. This includes the design and commissioning of a new flat field spectrometer. The flat field spectrometer has been shown to offer much grater sensitivity to harmonic signals and offers a lower energy range than the Rowland type spectrometer. The wavelength range of the flat field is adjustable by moving the grating position opening opportunities to study many different molecular systems.

In chapter 4 the new experimental set-up in Southampton has been used to demonstrate that high harmonic generation is sensitive to molecular vibrations. Whilst there were practical limitations with this experiment these have been removed since the commissioning of a new spectrometer. This leaves the opportunity to expand on the the first time resolved measurements that have been made in order to develop the understanding of high harmonic generations sensitivity to molecular vibrations. This can be done by performing more measurements of carbon tetrachloride to try and experimentally pin down the reasoning for the deterioration in the molecular vibrations. More complex photo-dissociation reactions could be investigated using this set-up, this could be done in conjunction with photoelectrons spectroscopy measurements providing information about both the ionisation and recombination matrix elements.

In chapter 5 the photodissociation of the $\tilde{A}$-state of ammonia was studied using a multiphoton ionisation probe. The multiphoton ionisation probe went via a Rydburg intermediate enabling the time window of the measurement to be extended. In order to devleop this work further the experiment could be repeated using an XUV probe, to capture all the reaction intermediates.

In chapter 6 the full reaction co-ordinate for the photo-dissociation of CS_2 has been mapped experimentally via the use of a high harmonic generation probe. This demonstrates that these experiments can be performed and that data for all intermediate states can be obtained. In order to improve on this a shorter pump pulse is required so that the cross correlation time can be reduced and the dynamics at early times, the bending motion in CS_2, can be more accurately traced. Many small molecular systems with low backgrounds in there photoelectron spectrum can now be investigated using this type of probe.

Bibliography

[1] Z. Hu, W.-B. Lee, X.-P. Zhang, P.-Y. Wei and K.-C. Lin, *ChemPhysChem*, 2008, **9**, 422–430, DOI: 10.1002/cphc.200700620.

[2] D. W. Turner, *Molecular Photoelectron Spectroscopy*, John Wiley and sons, 1st edn., 1970.

[3] *eBiochemicals*, `http://www.ebiochemicals.com/Wiki/Qceb000029274_Raman.html`, Accessed: 02-10-2017.

[4] F. Valente, *Pubblicazioni dello IUSS*, 2008, **2**, 1–112.

[5] R. P. Wayne, *Chemistry of atmospheres: an introduction to the chemistry of the atmospheres of earth, the planets, and their satellites*, Oxford University Press, Oxford [England] ; New York, 3rd edn., 2000.

[6] V. G. Stavros and J. R. Verlet, *Annual Review of Physical Chemistry*, 2016, **67**, 211–232, DOI: 10.1146/annurev-physchem-040215-112428.

[7] J. C. S. N. J. Turro, V. Ramamurthy, *Modern Molecular Photochemistry of Organic Molecules*, University Science Books Sausalito, California, Columbia University, University of Miami, University of Ottaw, 1st edn., 2010.

[8] O. Geßner, A. M. D. Lee, J. P. Shaffer, H. Reisler, S. V. Levchenko, A. I. Krylov, J. G. Underwood, H. Shi, A. L. L. East, D. M. Wardlaw, E. t. H. Chrysostom, C. C. Hayden and A. Stolow, *Science*, 2006, **311**, 219–222, DOI: 10.1126/science.1120779.

[9] S. Adachi, M. Sato and T. Suzuki, *The Journal of Physical Chemistry Letters*, 2015, **6**, 343–346, DOI: 10.1021/jz502487r.

[10] A. Jablonski, , 1933, **131**, 839–840, DOI: 10.1038/131839b0.

[11] P. Siegbahn and B. Liu, *The Journal of Chemical Physics*, 1978, **68**, 2457–2465, DOI: 10.1063/1.436018.

[12] A. H. Zewail, *The Journal of Physical Chemistry A*, 2000, **104**, 5660–5694, DOI: 10.1021/jp001460h.

[13] B. H. Stuart, *Infrared Spectroscopy: Fundamentals and Applications*, Wiley, 1st edn., 2004.

[14] *Dedication*, ed. J. R. Ferraro, K. Nakamoto and C. W. Brown, Academic Press, San Diego, Second Edition edn., 2003, pp. v –, DOI: https://doi.org/10.1016/B978-0-12-254105-6.50022-6.

[15] E. P. M. Badertscher, P.Bühlmann, *Structure Determination of Organic Compounds*, Springer, Berlin, Heidelberg, 4th edn., 2009.

[16] A. Huefner, W.-L. Kuan, R. A. Barker and S. Mahajan, *Nano Letters*, 2013, **13**, 2463–2470, DOI: 10.1021/nl400448n.

[17] K. Kneipp, H. Kneipp, I. Itzkan, R. R. Dasari and M. S. Feld, *Chemical Reviews*, 1999, **99**, 2957–2976, DOI: 10.1021/cr980133r.

[18] N. Dudovich, D. Oron and Y. Silberberg, *Nature*, 2002, **418**, 512–4.

[19] D. Patterson, M. Schnell and J. M. Doyle, *Nature*, 2013, **497**, 475–7.

[20] A. L. S. C. H. Townes, *Microwave Spectroscopy*, Dover Publications Inc., 4th edn., 2012.

[21] S. Weiss, *Science*, 1999, **283**, 1676–1683, DOI: 10.1126/science.283.5408.1676.

[22] G. Poter, *Flash photolysis and some of its applications*, 1967.

[23] M. Eigen, *Immeasurably fast reactions^*$*, 1967.

[24] U. Keller, *Nature*, 2003, **424**, 831–838, DOI: 10.1038/nature01938.

[25] M. J. Rosker, M. Dantus and A. H. Zewail, *The Journal of Chemical Physics*, 1988, **89**, 6113–6127, DOI: 10.1063/1.455427.

[26] M. Dantus, M. J. Rosker and A. H. Zewail, *The Journal of Chemical Physics*, 1987, **87**, 2395, DOI: 10.1063/1.453122.

[27] I. Gierz, F. Calegari, S. Aeschlimann, M. Chávez Cervantes, C. Cacho, R. T. Chapman, E. Springate, S. Link, U. Starke, C. R. Ast and A. Cavalleri, *Phys. Rev. Lett.*, 2015, **115**, 086803, DOI: 10.1103/PhysRevLett.115.086803.

[28] M. Faubel, B. Steiner and J. P. Toennies, *The Journal of Chemical Physics*, 1997, **106**, 9013–9031, DOI: 10.1063/1.474034.

[29] J. H. D. Eland, *Journal of Physics E: Scientific Instruments*, 1978, **11**, 969.

[30] L. Nugent-Glandorf, M. Scheer, D. A. Samuels, A. M. Mulhisen, E. R. Grant, X. Yang, V. M. Bierbaum and S. R. Leone, *Phys. Rev. Lett.*, 2001, **87**, 193002, DOI: 10.1103/PhysRevLett.87.193002.

[31] A. Makida, H. Igarashi, T. Fujiwara, T. Sekikawa, Y. Harabuchi and T. Taketsugu, *The Journal of Physical Chemistry Letters*, 2014, **5**, 1760–1765, DOI: 10.1021/jz5003567.

[32] P. B. Corkum, *Phys. Rev. Lett.*, 1993, **71**, 1994–1997, DOI: 10.1103/PhysRevLett.71.1994.

[33] V. S. Popov, *Physics-Uspekhi*, 2004, **47**, 855–885, DOI: 10.1070/PU2004v047n09ABEH001812.

[34] N. B. D. M. V. Ammosov and V. P. Krainow, *Scv. Phys. JETP*, 1986, **6**, year.

[35] B. H. Bransden and C. J. Joachain, *Physics of atoms and molecules*, Prentice Hall, Harlow, England ; New York, 2nd edn., 2003.

[36] J. L. Krause, K. J. Schafer and K. C. Kulander, *Phys. Rev. A*, 1992, **45**, 4998–5010, DOI: 10.1103/PhysRevA.45.4998.

[37] M. Lewenstein, P. Balcou, M. Y. Ivanov, A. L'Huillier and P. B. Corkum, *Phys. Rev. A*, 1994, **49**, 2117–2132, DOI: 10.1103/PhysRevA.49.2117.

[38] A. D. Shiner, *Phys. Rev. Lett.*, 2009, **103**, year, DOI: 10.1103/PhysRevLett.103.073902.

[39] H. G. Muller, *Phys. Rev. A*, 1999, **60**, 1341–1350, DOI: 10.1103/PhysRevA.60.1341.

[40] E. Schrödinger, *Phys. Rev.*, 1926, **28**, 1049–1070, DOI: 10.1103/PhysRev.28.1049.

[41] C. Winterfeldt, C. Spielmann and G. Gerber, *Reviews of Modern Physics*, 2008, **80**, 117–140, DOI: 10.1103/RevModPhys.80.117.

[42] P. Balcou, P. Salieres, A. L'Huillier and M. Lewenstein, *Physical Review A*, 1997, **55**, 3204.

[43] M. Bellini, C. Lynga, A. Tozzi, M. B. Gaarde, T. W. Hänsch, A. L'Huillier and C.-G. Wahlström, *Physical Review Letters*, 1998, **81**, 297.

[44] A. McPherson, G. Gibson, H. Jara, U. Johann, T. S. Luk, I. A. McIntyre, K. Boyer and C. K. Rhodes, *J. Opt. Soc. Am. B*, 1987, **4**, 595–601, DOI: 10.1364/JOSAB.4.000595.

[45] K. J. Schafer and K. C. Kulander, *Phys. Rev. Lett.*, 1997, **78**, 638–641, DOI: 10.1103/PhysRevLett.78.638.

[46] P. M. Paul, E. S. Toma, P. Breger, G. Mullot, F. Augé, P. Balcou, H. G. Muller and P. Agostini, *Science*, 2001, **292**, 1689–1692, DOI: 10.1126/science.1059413.

[47] O. Smirnova, S. Patchkovskii, Y. Mairesse, N. Dudovich, D. Villeneuve, P. Corkum and M. Y. Ivanov, *Phys. Rev. Lett.*, 2009, **102**, 063601, DOI: 10.1103/PhysRevLett.102.063601.

[48] M. C. H. Wong, A.-T. Le, A. F. Alharbi, A. E. Boguslavskiy, R. R. Lucchese, J.-P. Brichta, C. D. Lin and V. R. Bhardwaj, *Phys. Rev. Lett.*, 2013, **110**, 033006, DOI: 10.1103/PhysRevLett.110.033006.

[49] M. Odstrcil, P. Baksh, S. A. Boden, R. Card, J. E. Chad, J. G. Frey and W. S. Brocklesby, *Opt. Express*, 2016, **24**, 8360–8369, DOI: 10.1364/OE.24.008360.

[50] J. Itatani, J. Levesque, D. Zeidler, H. Niikura and e. al, *Nature*, 2004, **432**, 867–71.

[51] H. Yun, S. J. Yun, G. H. Lee and C. H. Nam, *Journal of Physics B: Atomic, Molecular and Optical Physics*, 2017, **50**, 022001.

[52] A. Flettner, T. Pfeifer, D. Walter, C. Winterfeldt, C. Spielmann and G. Gerber, *Applied Physics B*, 2003, **77**, 747–751, DOI: 10.1007/s00340-003-1329-x.

[53] T. T. Luu, M. Garg, S. Y. Kruchinin, A. Moulet, M. T. Hassan and E. Goulielmakis, *Nature*, 2015, **521**, 498–502.

[54] S. Ghimire, A. D. Dichiara, E. Sistrunk, P. Agostini, L. F. Dimauro and D. A. Reis, *Nature Physics*, 2011, **7**, 138–141.

[55] A. D. Shiner, B. E. Schmidt, C. Trallero-Herrero, H. J. Wörner, S. Patchkovskii, P. B. Corkum, J.-C. Kieffer, F. Légaré and D. M. Villeneuve, *Nature Physics*, 2011, **7**, 464–467, DOI: 10.1038/nphys1940.

[56] H. J. Wörner, J. B. Bertrand, D. V. Kartashov, P. B. Corkum and D. M. Villeneuve, *Nature*, 2010, **466**, 604–607, DOI: 10.1038/nature09185.

[57] J. O. F. Thompson, R. A. Livingstone and D. Townsend, *The Journal of Chemical Physics*, 2013, **139**, 034316, DOI: 10.1063/1.4813005.

[58] H. J. Wörner, J. B. Bertrand, B. Fabre, J. Higuet, H. Ruf, A. Dubrouil, S. Patchkovskii, M. Spanner, Y. Mairesse, V. Blanchet, E. Mével, E. Constant, P. B. Corkum and D. M. Villeneuve, *Science*, 2011, **334**, 208–212, DOI: 10.1126/science.1208664.

[59] C. Vozzi, R. Torres, M. Negro, L. Brugnera, T. Siegel, C. Altucci, R. Velotta, F. Frassetto, L. Poletto, P. Villoresi, S. D. Silvestri, S. Stagira and J. P. Marangos, *Applied Physics Letters*, 2010, **97**, 241103, DOI: 10.1063/1.3526752.

[60] N. L. Wagner, A. Wüest, I. P. Christov, T. Popmintchev, X. Zhou, M. M. Murnane and H. C. Kapteyn, *PNAS*, 2006, **103**, 13279–13285, DOI: 10.1073/pnas.0605178103.

[61] H. A. Haus, *IEEE Journal of Selected Topics in Quantum Electronics*, 2000, **6**, 1173–1185, DOI: 10.1109/2944.902165.

[62] R. Trebino, *Frequency-Resolved Optical Gating: The Measurement of Ultrashort Laser Pulses*, Springer US : Imprint : Springer, Boston, MA, 2000.

[63] D. J. Kane and R. Trebino, *Quantum Electronics, IEEE Journal of*, 1993, **29**, 571–579.

[64] E. Hecht, *Optics*, Addison-Wesley, San Francisco, 4th edn., 2010.

[65] F. Frassetto, C. Cacho, C. A. Froud, I. E. Turcu, P. Villoresi, W. A. Bryan, E. Springate and L. Poletto, *Opt. Express*, 2011, **19**, 19169–19181, DOI: 10.1364/OE.19.019169.

[66] D. Irimia, D. Dobrikov, R. Kortekaas, H. Voet, D. A. van den Ende, W. A. Groen and M. H. M. Janssen, *Review of Scientific Instruments*, 2009, **80**, 113303, DOI: 10.1063/1.3263912.

[67] A. T. J. B. Eppink and D. H. Parker, *Review of Scientific Instruments*, 1997, **68**, 3477, DOI: 10.1063/1.1148310.

[68] A. H. and S. F. S., *The Structure and Utilization of Supersonic Free Jets in Low Density Wind Tunnels*, 1965, p. 84.

[69] J. Grant-Jacob, *Ph.D. thesis*, University of Southampton, 2011.

[70] J. Wiza, *Nuclear Instruments and Methods*, 1979, **162**, 578–601.

[71] A. Ferré, D. Staedter, F. Burgy, M. Dagan, D. Descamps, N. Dudovich, S. Petit, H. Soifer, V. Blanchet and Y. Mairesse, *Journal of Physics B: Atomic, Molecular and Optical Physics*, 2014, **47**, 124023.

[72] Z. B. Walters, S. Tonzani and C. H. Greene, *Journal of Physics B: Atomic, Molecular and Optical Physics*, 2007, **40**, F277.

[73] W. Li, X. Zhou, R. Lock, S. Patchkovskii, A. Stolow, H. C. Kapteyn and M. M. Murnane, *Science*, 2008, **322**, 1207–1211, DOI: 10.1126/science.1163077.

[74] *NIST Chemistry WebBook, Reference Database Number 69*, `http://webbook.nist.gov/cgi/cbook.cgi?ID=C56235&Units=SI`, Accessed: 02-10-2017.

[75] S. Patchkovskii, *Phys. Rev. Lett.*, 2009, **102**, 253602, DOI: 10.1103/PhysRevLett.102.253602.

[76] *Computational Chemistry Comparison and Benchmark DataBase*, `http://cccbdb.nist.gov/`, Accessed: 02-10-2017.

[77] N. L. Evans, H. Yu, G. M. Roberts, V. G. Stavros and S. Ullrich, *Physical Chemistry Chemical Physics*, 2012, **14**, 10401–10409, DOI: 10.1039/c2cp40178a.

[78] D. Bonhommeau, R. Valero, D. G. Truhlar and A. W. Jasper, *Journal of Chemical Physics*, 2009, **130**, 234303, DOI: 10.1063/1.3132222.

[79] K. L. Wells, G. Perriam and V. G. Stavros, *Journal of Chemical Physics*, 2009, **130**, 074308, DOI: 10.1063/1.3072763.

[80] M. L. Hause, Y. H. Yoon and F. F. Crim, *Molecular Physics*, 2008, **106**, 1127–1133, DOI: 10.1080/00268970802245192.

[81] Z. H. Li, R. Valero and D. G. Truhlar, *Theoretical Chemistry Accounts*, 2007, **118**, 9–24, DOI: 10.1007/s00214-006-0237-7.

[82] M. L. Hause, Y. H. Yoon and F. F. Crim, *Journal of Chemical Physics*, 2006, **125**, 174309, DOI: 10.1063/1.2363192.

[83] R. Loomis, J. Reid and S. Leone, *Journal of Chemical Physics*, 2000, **112**, 658–669, DOI: 10.1063/1.480677.

[84] D. Mordaunt, M. Ashfold and R. Dixon, *Journal of Chemical Physics*, 1998, **109**, 7659–7662, DOI: 10.1063/1.477411.

[85] J. Biesner, L. Schnieder, G. Ahlers, X. Xie, K. Welge, M. Ashfold and R. Dixon, *Journal of Chemical Physics*, 1989, **91**, 2901–2911, DOI: 10.1063/1.457644.

[86] M. Ashfold, C. Bennett and R. Dixon, *Chemical Physics*, 1985, **93**, 293–306, DOI: 10.1016/0301-0104(85)80026-4.

[87] M. Ashfold, C. Bennett and R. Dixon, *Faraday Discussions*, 1986, **82**, 163–175, DOI: 10.1039/dc9868200163.

[88] A. Bach, J. Hutchison, R. Holiday and F. Crim, *Journal of Physical Chemistry A*, 2003, **107**, 10490–10496, DOI: 10.1021/jp027396g.

[89] A. Bach, J. Hutchison, R. Holiday and F. Crim, *Journal of Chemical Physics*, 2002, **116**, 4955–4961, DOI: 10.1063/1.1450550.

[90] R. Dixon, *Molecular Physics*, 1996, **88**, 949–977, DOI: 10.1080/00268979650025993.

[91] T. Seideman, *Journal of Chemical Physics*, 1995, **103**, 10556–10565, DOI: 10.1063/1.469839.

[92] L. Ziegler, *Journal of Chemical Physics*, 1985, **82**, 664–669, DOI: 10.1063/1.448542.

[93] J. D. Rodriguez, M. G. Gonzalez, L. Rubio-Lago and L. Banares, *Phys. Chem. Chem. Phys.*, 2014, **16**, 406–413, DOI: 10.1039/C3CP53523A.

[94] H. Yu, N. L. Evans, A. S. Chatterley, G. M. Roberts, V. G. Stavros and S. Ullrich, *The Journal of Physical Chemistry A*, 2014, **118**, 9438–9444, DOI: 10.1021/jp507201a.

[95] K. Giri, E. Chapman, C. S. Sanz and G. Worth, *Journal of Chemical Physics*, 2011, **135**, 044311, DOI: 10.1063/1.3614038.

[96] F. Bernardi, M. Olivucci and M. A. Robb, *Chem. Soc. Rev.*, 1996, **25**, 321–328.

[97] V. Donnelly, A. Baronavski and J. McDonald, *Chemical Physics*, 1979, **43**, 271 – 281, DOI: http://dx.doi.org/10.1016/0301-0104(79)85194-0.

[98] J. Biesner, L. Schnieder, J. Schmeer, G. Ahlers, X. Xie, K. Welge, M. Ashfold and R. Dixon, *Journal of Chemical Physics*, 1988, **88**, 3607–3616, DOI: 10.1063/1.453910.

[99] A. S. Chatterley, G. M. Roberts and V. G. Stavros, *The Journal of Chemical Physics*, 2013, **139**, 034318, DOI: 10.1063/1.4811672.

[100] A. Makida, H. Igarashi, T. Fujiwara, T. Sekikawa, Y. Harabuchi and T. Taketsugu, *The Journal of Physical Chemistry Letters*, 2014, **5**, 1760–1765, DOI: 10.1021/jz5003567.

[101] R. Iikubo, T. Fujiwara, T. Sekikawa, Y. Harabuchi, S. Satoh, T. Taketsugu and Y. Kayanuma, *The Journal of Physical Chemistry Letters*, 2015, **6**, 2463–2468, DOI: 10.1021/acs.jpclett.5b00943.

[102] L. Nugent-Glandorf, M. Scheer, D. A. Samuels, A. M. Mulhisen, E. R. Grant, X. Yang, V. M. Bierbaum and S. R. Leone, *Phys. Rev. Lett.*, 2001, **87**, 193002, DOI: 10.1103/PhysRevLett.87.193002.

[103] G. M. Roberts, J. L. Nixon, J. Lecointre, E. Wrede and J. R. R. Verlet, *Review of Scientific Instruments*, 2009, **80**, 053104, DOI: 10.1063/1.3126527.

[104] K. Zhao, T. Colvin, W. T. H. III and G. Zhang, *Review of Scientific Instruments*, 2002, **73**, 3044–3050, DOI: 10.1063/1.1493231.

[105] D. A. Horke, H. M. Watts, A. D. Smith, E. Jager, E. Springate, O. Alexander, C. Cacho, R. T. Chapman and R. S. Minns, *Phys. Rev. Lett.*, 2016, **117**, 163002, DOI: 10.1103/PhysRevLett.117.163002.

[106] J. Xie, B. Jiang, G. Li, S. Yang, J. Xu, G. Sha, D. Xu, N. Lou and C. Zhang, *Faraday Discussions*, 2000, **115**, 127–136, DOI: 10.1039/b000301h.

[107] H. P. Liu, S. H. Yin, J. Y. Zhang, L. Wang, B. Jiang and N. Q. Lou, *Physical Review A*, 2006, **74**, 053418, DOI: 10.1103/PhysRevA.74.053418.

[108] C. C. Pemberton, Y. Zhang, K. Saita, A. Kirrander and P. M. Weber, *Journal of Physical Chemistry A*, 2015, **119**, 8832–8845, DOI: 10.1021/acs.jpca.5b05672.

[109] J. Gosselin and P. Weber, *Journal of Physical Chemistry A*, 2005, **109**, 4899–4904, DOI: 10.1021/jp0503866.

[110] D. Bellshaw, D. A. Horke, A. D. Smith, H. M. Watts, E. Jager, E. Springate, O. Alexander, C. Cacho, R. T. Chapman, A. Kirrander and R. S. Minns, *Chemical Physics Letters*, 2017, **683**, 383 – 388, DOI: https://doi.org/10.1016/j.cplett.2017.02.058.

[111] C. Z. Bisgaard, O. J. Clarkin, G. Wu, A. M. D. Lee, O. Geßner, C. C. Hayden and A. Stolow, *Science*, 2009, **323**, 1464–1468, DOI: 10.1126/science.1169183.

[112] C. Z. Hockett, Paul Bisgaard, O. J. Clarkin and A. Stolow, *Nature Physics*, 2011, **7**, 612–615, DOI: doi:10.1038/nphys1980.

[113] K. Wang, V. McKoy, P. Hockett and M. S. Schuurman, *Phys. Rev. Lett.*, 2014, **112**, 113007, DOI: 10.1103/PhysRevLett.112.113007.

[114] T. Horio, R. Spesyvtsev and T. Suzuki, *Opt. Express*, 2013, **21**, 22423–22428, DOI: 10.1364/OE.21.022423.

[115] R. Spesyvtsev, T. Horio, Y.-I. Suzuki and T. Suzuki, *The Journal of Chemical Physics*, 2015, **142**, 074308, DOI: 10.1063/1.4907749.

[116] D. Townsend, H. Satzger, T. Ejdrup, A. M. D. Lee, H. Stapelfeldt and A. Stolow, *The Journal of Chemical Physics*, 2006, **125**, 234302, DOI: 10.1063/1.2403137.

[117] T. Horio, R. Spesyvtsev, Y. Furumido and T. Suzuki, *The Journal of Chemical Physics*, 2017, **147**, 013932, DOI: 10.1063/1.4982219.

[118] I. M. Waller and J. W. Hepburn, *The Journal of Chemical Physics*, 1987, **87**, 3261–3268, DOI: 10.1063/1.453018.

[119] W. Tzeng, H. Yin, W. Leung, J. Luo, S. Nourbakhsh, G. D. Flesch and C. Y. Ng, *The Journal of Chemical Physics*, 1988, **88**, 1658–1669, DOI: 10.1063/1.454144.

[120] T. N. Kitsopoulos, C. R. Gebhardt and T. P. Rakitzis, *The Journal of Chemical Physics*, 2001, **115**, 9727–9732, DOI: 10.1063/1.1415436.

[121] W. S. McGivern, O. Sorkhabi, A. H. Rizvi, A. G. Suits and S. W. North, *The Journal of Chemical Physics*, 2000, **112**, 5301–5307, DOI: 10.1063/1.481101.

[122] D. Xu, J. Huang and W. M. Jackson, *The Journal of Chemical Physics*, 2004, **120**, 3051–3054, DOI: 10.1063/1.1646671.

[123] M. Brouard, E. K. Campbell, R. Cireasa, A. J. Johnsen and W.-H. Yuen, *The Journal of Chemical Physics*, 2012, **136**, 044310, DOI: 10.1063/1.3678007.

[124] S. C. Yang, A. Freedman, M. Kawasaki and R. Bersohn, *The Journal of Chemical Physics*, 1980, **72**, 4058–4062, DOI: 10.1063/1.439686.

[125] M. Addison, R. Donovan and C. Fotakis, *Chemical Physics Letters*, 1980, **74**, 1980, DOI: https://doi.org/10.1016/0009-2614(80)85014-7.

[126] G. Dornhoefer, W. Hack and W. Langel, *The Journal of Physical Chemistry*, 1984, **88**, 3060–3069, DOI: 10.1021/j150658a026.

[127] V. R. McCrary, R. Lu, D. Zakheim, J. A. Russell, J. B. Halpern and W. M. Jackson, *The Journal of Chemical Physics*, 1985, **83**, 3481–3490, DOI: 10.1063/1.449152.

[128] L. Zuin, F. Innocenti, M. Costa, A. Dias, A. Morris, A. Paiva, S. Stranges, J. West and J. Dyke, *Chemical Physics*, 2004, **298**, 213 – 222, DOI: https://doi.org/10.1016/j.chemphys.2003.11.011.

[129] M. Barthel, R. Flesch, E. Rühl and B. M. McLaughlin, *Phys. Rev. A*, 2015, **91**, 013406, DOI: 10.1103/PhysRevA.91.013406.

[130] N. Jonathan, A. Morris, M. Okuda, D. Smith and K. Ross, *Chemical Physics Letters*, 1972, **13**, 334 – 336, DOI: https://doi.org/10.1016/0009-2614(72)85080-2.